CHARACTERIZATION OF INTERFACIAL ENZYME KINETICS AND PHOSPHORYLATION-DEPHOSPHORYLATION CYCLE OF PHOSPHOINOSITIDES ON MODEL LIPID MEMBRANE

Chun Liu

A DISSERTATION

in

Chemistry

Presented to the Faculties of the University of Pennsylvania

in

Partial Fulfillment of the Requirements for the

Degree of Doctor of Philosophy

2019

Supervisor of Dissertation

_____

Dr. Tobias Baumgart

Professor of Chemistry

Graduate Group Chairperson

_____

Dr. David W. Christianson

Dissertation Committee

Dr. Feng Gai, Edmund J. and Louise W. Kahn Endowed Term Professor of Chemistry

Dr. Paul Janmey, Professor of IME & Physiology

Dr. Ronen Marmorstein, George W. Raiziss Professor of Biochemistry and Biophysics

CHARACTERIZATION OF INTERFACIAL ENZYME KINETICS AND PHOSPHORYLATION-DEPHOSPHORYLATION CYCLE OF PHOSPHOINOSITIDES ON MODEL LIPID MEMBRANE

COPYRIGHT

2019

Chun Liu

This work is licensed under the
Creative Commons Attribution-
NonCommercial-ShareAlike 3.0
License

To view a copy of this license, visit

https://creativecommons.org/licenses/by-nc-sa/3.0/us/

ACKNOWLDGMENTS

Here I would like to thank those who have helped me in my Ph.D. career and led to the production of this dissertation thesis.

First, I would like to express my deepest gratitude to my Ph.D. advisor Dr. Tobias. Baumgart. Dr. Baumgart has been a nice advisor who not only guided me in doing research, but also inspired me to think critically in every aspects of life. His encouragement and guidance are both beneficial to my Ph.D. study and my future career.

Next, I would like to thank my thesis committee members: Dr. Feng Gai, Dr. Paul Janmey, and Dr. Ronen Marmorstein. They all spared valuable time every year to listen to my research progress and gave me precious suggestions for my project. Specifically, Dr. Gai has given me many suggestions in theoretical model fitting, Dr. Janmey has provided me several good suggestions in studying lipid and protein interactions, and Dr. Marmorstein has given me many instructions in kinase reactions and kindly provided a critical kinase for my research.

I want to thank all the group members in Dr. Baumgart lab for research discussion and idea brainstorming. Dr. Chih-Jung Hsu, Dr. Katarzyna I Jankowsak, Dr. Sanghamitra Deb, Dr. Wan-Ting Hsieh, Dr. Tingting Wu, Dr. Chen Zhu, Dr. Zheng Shi, Dr. Ningwei, Dr. Zhiming Chen, Dr. Zachary T Graber, and Dr. Samantha Wilner, for their help in instrumentation and research discussion. Chih-Jung helped me a lot in TIRF alignment and microscopy discussion. Sanghamitra, Wan-Ting, and Tingting taught me protein expression and purification. Katarzyna, Chen, Zheng, and Zhiming helped me a lot on GUV preparation and discussion. Ningwei helped me with plasma etcher training and channel pattern preparation. Zachary and Samantha had many scientific discussions with me. I want to thank two previous undergraduate partners, Vinicius Ferreira and Eric Xu, who assisted me in flow chamber development. I want to further thank all the help for current members Jaclyn Robustelli, Sankalp Shukla, Rui Jin, Zachary Zimmerman, Dr. Samsuzzoha Mondal, Dr. Sohini Mukherjee, Curtis Kuo, Saagar Asnani, and Imañia Powers, for their help in maintaining lab business and creating a nice environment for live discussions about scientific research. I want to thank Zachary T. Graber, Samantha

Wilner Zachary Zimmerman, Saagar Asnani, Curtis Kuo, Jaclyn Robustelli, and Imañia Powers for spending their valuable time proofreading and advising my manuscript and thesis.

I want to thank collaborating labs for kindly offering technical support and instrumentation training. Dr. Michael Grasso, from Dr. Marmorstein's lab, helped me in kinase expression and purification. Kristen McKibben, from Dr. Rhoades's lab, assisted me in protein purification and ultracentrifugation. Alokendra Ghosh, from Dr. Radhakrishnan's lab, helped me with theoretical model simulation.

I want to thank my friends at UPenn, particularly, Dr. Chun-Wei Lin and Dr. Xinle Liu. Xinle helped me a lot in model discussion and future career path selection, and Chun-Wei helped me solving many difficulties in both work and life. I also want to thank Dr. Yu-Hsiu Wang and Yi-Chih Lin, who gave me many useful advices during my Ph.D. career. There are many other friends I wish to thanks, they made my past six years in Philly more colorful.

Finally, I would like to thank my mom Ming-Hsia Ting, my dad De-Guang Liu, my brother Qi Liu, and my girlfriend Chen Wu. Their encouragement is so important to support me to finish it. Words can't describe how thankful I am.

ABSTRACT

CHARACTERIZATION OF INTERFACIAL ENZYME KINETICS AND A PHOSPHORYLATION-DEPHOSPHORYLATION CYCLE OF PHOSPHOINOSITIDES ON MODEL LIPID MEMBRANES

Chun Liu

Tobias Baumgart

Phosphoinositides, though rare species in cell membranes, play important roles in cell regulation and signal transduction mediation. Two vital phosphoinositides are PI(4,5)P2 and PI(3,4,5)P3, which are interconverted by a kinase, PI3K, and a phosphatase, PTEN. PI(3,4,5)P3 acts as a second messenger to recruit and activate Akt to trigger downstream signaling pathways for cell proliferation and growth. Regulation of PI(3,4,5)P3 amounts on cell membranes is critical, however, detailed regulatory mechanisms are not well known yet. First, the mechanism of PI(3,4,5)P3 hydrolysis by PTEN is still under debate. Second, how Ras GTPase affects PTEN-mediated PI(3,4,5)P3 degradation is not well known. Third, the bistability of PI(3,4,5)P3 and PI(4,5)P2 has been hypothesized to be important in maintaining cell polarity and the cell fate switch, but how this bistability is achieved by the collaboration of PTEN / PI3K is also unknown.

To answer the above questions, first we studied the binding affinity and specificity of sensor proteins to the phosphoinositides. YFP-PH-Grp1 and mCherry-PH-Grp1 are shown to bind PI(3,4,5)P3 specifically, while EGFP-PH-PLCδ1 is shown to bind PI(4,5)P2 specifically. Fluorescent protein-labeled Grp1 and PLCδ1 are then used to quantify and monitor PI(3,4,5)P3 and PI(4,5)P2 amounts in the presence of enzymes by either TIRF or confocal microscopy.

Second, we characterized PTEN-mediated PI(3,4,5)P3 dephosphorylation and PI3K-mediated PI(4,5)P2 phosphorylation reactions on model lipid membranes. The rate of PI(3,4,5)P3 hydrolysis by PTEN increases with increasing PI(4,5)P2 concentration, suggesting product-mediated positive feedback loop. By fitting kinetic traces of PI(3,4,5)P3 hydrolysis with the theoretical model we developed, the origin of this feedback was proposed to arise from membrane recruitment and product-mediated activation of PTEN. PI(4,5)P2 phosphorylation by PI3K, which is activated by phosphopeptide binding, is shown to follow typical Michaelis-Menten kinetics. Membrane-bounds KRas is shown to activate PI3K synergistically with phosphopeptide and is shown to slow down PI(3,4,5)P3 hydrolysis by PTEN.

Finally, we combined both PTEN and PI3K on bead-supported lipid bilayers and observed that the steady-state of PI(4,5)P2 / PI(3,4,5)P3 distribution depends not only on the PTEN / PI3K ratio, but also on the initial state of phosphoinositides. This phosphorylation-dephosphorylation cycle is shown on model lipid membranes to exhibit hysteresis, which is the hallmark of bistability. By kinetic model simulation, we identified that the PTEN-PI(4,5)P2 positive feedback loop is critical in establishing phosphoinositide bistability. This bistability can also be affected by the presence of sensor proteins due to competitive substrate binding, leading to the bimodal distribution of PI(4,5)P2-rich and PI(3,4,5)P3-rich states at an intermediate PTEN / PI3K ratio.

TABLE OF CONTENTS

LIST OF TABLES

LIST OF ILLUSTRATIONS

CHAPTER 1. Background and Significance[1,2]

1.1 PI3K / Akt Signaling Pathway

The PI3K signaling pathway, in which phosphoinositide 3-kinase (PI3K) and phosphatase and tensin homologue deleted on chromosome 10 (PTEN) function as positive and negative regulators through phosphorylation and de-phosphorylation, respectively, of phosphoinositide lipids, has become a focus of basic, pre-clinical, and clinical research [1, 2]. This pathway regulates cellular metabolism and growth, proliferation, survival, and cytoskeletal motility, and is perturbed in a vast number of different cancers, highlighting its biomedical importance [3].

Several review papers have been published to describe the PI3K / Akt signaling pathway in detail [3-6] and a short summary is described below. PI3K is either activated by G-protein coupled receptors (GPCRs) or receptor tyrosine kinases (RTKs), resulting in the phosphorylation of phosphatidylinositol-4,5-bisphosphate (PI(4,5)P2) to phosphatidylinositol-3,4,5-trisphosphate (PI(3,4,5)P3) (Fig 1.1). Newly produced PI(3,4,5)P3 then serves as a docking site for the recruitment of pleckstrin homology (PH) domain-containing protein Akt (also called protein kinase B), which is fully activated on the cell membrane through phosphorylation by PDK1 and mTOR complex 2 (mTORC2). Activated Akt phosphorylates numerous downstream proteins, including FOXO

[1] Parts of this chapter are reproduced by previously published work: Liu, C.; Deb, S.; Ferreira, V. S.; Xu, E.; Baumgart, T., Kinetics of PTEN-mediated PI(3,4,5)P3 hydrolysis on solid supported membranes. *PLoS One* **2018,** *13* (2).

[2] Parts of this chapter are reproduced by currently submitted work: Liu, C.; Zimmerman, Z. E.; Grasso, M.; Gosh, A.; Marmorstein, R.; Radhakrishnan, R.; Baumgart, T., Bistable reaction behavior in PTEN / PI3K mediated phosphoinositide lipid conversion.

transcription factor and TSC2, to trigger cell survival and proliferation. More detailed information about PI3K will be discussed in Chapter 1.2.

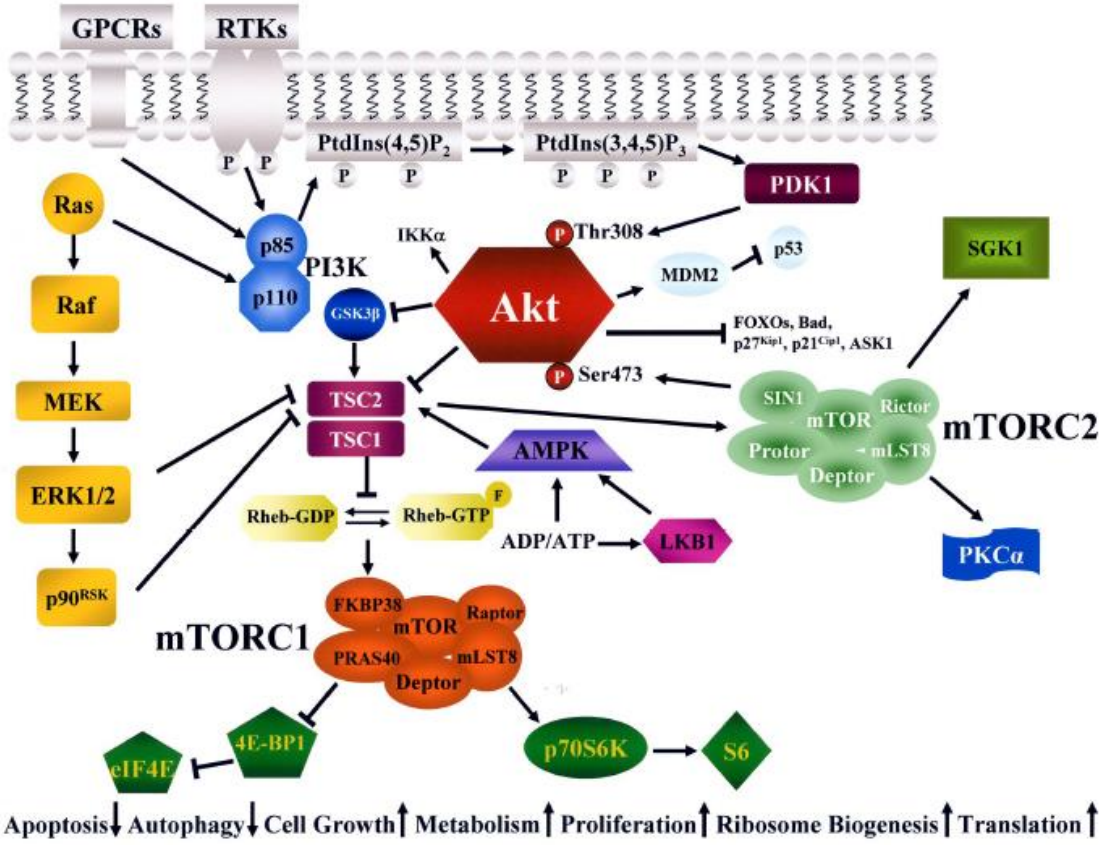

Fig 1.1 The PI3K / Akt signaling pathway. Upon activation by either GPCR or RTK (details in Chapter 1.2), PI3K phosphorylates PI(4,5)P2 to PI(3,4,5)P3, which recruits both PDK1 and Akt to the cell membrane. Full Akt activation occurs through phosphorylation by PDK1 and mTORC2. Active Akt then phosphorylates downstream proteins to trigger cell proliferation, growth, and other events. This figure is adapted from Ref. [6].

The PI3K / Akt signaling pathway is down-regulated by the phosphatase PTEN, which counteracts the PI3K reaction by dephosphorylating PI(3,4,5)P3 back to PI(4,5)P2. More details of PTEN will be discussed in Chapter 1.3.

1.2 Phosphatidylinositol 3-Kinase (PI3K)

PI3Ks are a family of lipid kinases that phosphorylate phosphatidylinositol and phosphoinositides at the D3 position of their inositol rings [7, 8]. PI3Ks are grouped into three classes (classes I - III) based on their structure, sequence, and substrate specificity. Class I PI3Ks phosphorylate PI(4,5)P2 to PI(3,4,5)P3, and they can be further divided into two subgroups based on the modes of activation: Class IA PI3Ks (composed of a p110 catalytic subunit with a p85 regulatory subunit, which inhibits p110) are activated by growth factor receptor tyrosine kinases (RTKs), and Class IB PI3Ks (composed of a p110γ catalytic subunit and a p101 or p87 regulator subunit) are activated by G protein-coupled receptors (GPCRs) (Fig 1.2). Both Class II and III PI3Ks phosphorylate PI to PI(3)P, and Class II PI3Ks can also phosphorylate PI(4)P to PI(3,4)P2.

Class IA PI3K activation is thought to occur as follows: Upon ligand binding, two RTKs dimerize, resulting in auto-phosphorylation of their YXXM motifs. This phosphorylated site serves as the binding site of the p85 subunit of Class IA PI3K. Inhibition of p110 catalytic domain by p85 is relieved upon binding, and the PI(4,5)P2 is phosphorylated to PI(3,4,5)P3 by p110 [3, 7].

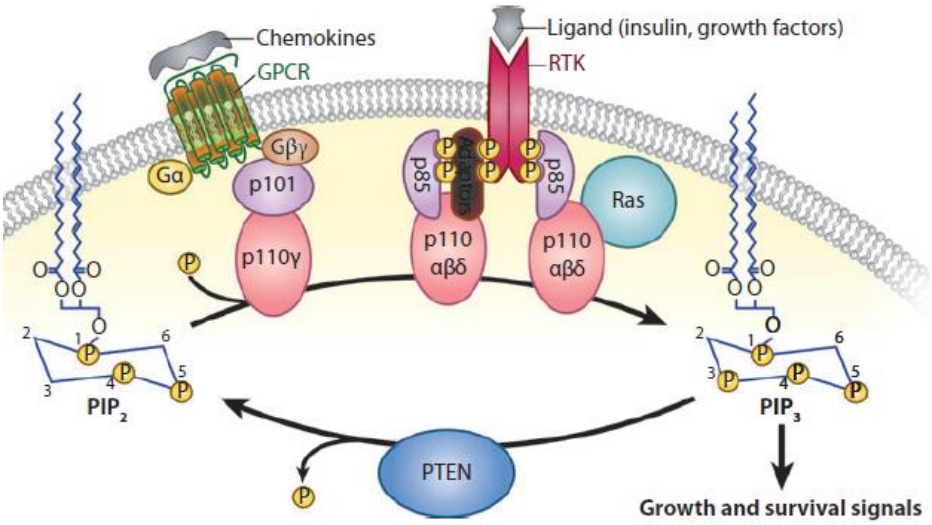

Fig 1.2 Activation of Class I PI3K by either GPCRs or RTKs on a cell membrane. In response to extracellular stimuli (e.g., chemokines, growth factors), PI3K is recruited and activated by either GPCRs or RTKs. Activated PI3K phosphorylates PI(4,5)P2 to PI(3,4,5)P3, which act as a second messenger to trigger downstream signaling pathway responsible for cell survival and growth. This figure is adapted from Ref. [7].

In mammalian cells, the class IA PI3K is composed of a p85-type regulatory subunit (p85α, p85β, p55α, p55γ, or p50α) and a p110 catalytic subunit (p110α, p110β, or p110δ). The domain structure of class IA PI3K is shown in the figure below (Fig 1.3). The p110 subunit contains five major domains, including a p85-binding (p85-BD) domain, a Ras-binding (RBD) domain, a C2 domain, a helical domain, and a catalytic domain (from N to C-terminus). The p85 subunit is composed of an N-terminal SRC homology 2 (nSH2) domain, an inter-SRC homology 2 (iSH2) domain, and a C-terminal SRC homology 2 (cSH2) domain. In two p85 isoforms, p85α and p85β, additional N-terminal SH3 and

breakpoint cluster homology (BH) domains are attached on the N-terminus. Inhibition of p110 results from the binding of the nSH2 domain of p85, and inhibition can be relieved by a phosphotyrosyl peptide (phosphopeptide) binding to the nSH2 domain *in vitro* [9, 10].

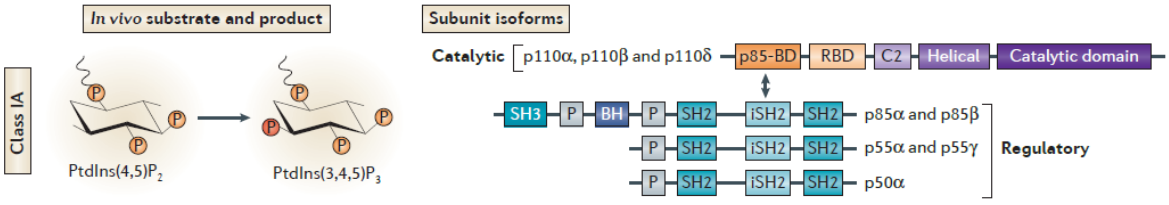

Fig 1.3 Domain structure of class IA PI3K. Class IA PI3Ks are composed of p110 catalytic subunit (with isoforms p110α, p110β, p110δ) and a p85-type regulatory subunit (with isoforms p85α, p85β, p55α, p55γ, or p50α). This figure is adapted from Ref. [11].

Overactivation of the PI3K signaling pathway, caused by somatic loss of PTEN or alternations in PI3K, is one of the most frequent events in human tumors [11]. Point mutations in the *PIK3CA* gene, which encodes the p110α subunit, were identified in various types of tumors, including breast cancer, colon cancer, and hepatocellular cancer [8, 12]. In *PIK3CA* mutations, around 80% occur at three hotspots: E542K, E545K, and H1047R [7]. E542K and E545K are in the helical domain, while H1047R is in the catalytic domain. All three mutations lead to enhanced PI3K activity *in vitro*, as well as to growth factor-independent activation of AKT. In the E545K mutation, the original inhibitory charge interaction from the p85 nSH2 domain is disrupted due to the

negatively charged glutamic acid being replaced by a positively charged lysine, leading to constitutive PI3K activation [7, 13].

1.3 Phosphatase and Tensin Homologue Deleted on Chromosome 10 (PTEN)

PTEN regulates the well-known PI3K / AKT pathway that is central in many cellular processes including cell growth, differentiation, and apoptosis [14] by hydrolyzing PI(3,4,5)P3 at the D3 position of the inositol ring to yield PI(4,5)P2. This process down-regulates membrane binding and subsequent activation of the serine-threonine protein kinase AKT, which has many cellular downstream effectors.

The domain structure of PTEN is shown in Fig 1.4. From N to C-terminus, PTEN contains a PI(4,5)P2-binding domain (PBD), a phosphatase domain, a C2 domain, a carboxyl-terminal tail, and a PDZ-binding domain (PDZ-BD). The N-terminal PI(4,5)P2-binding domain equips PTEN to be able to bind to its own reaction product, generating a positive feedback mechanism that underlies PTEN-mediated PI(3,4,5)P3 hydrolysis, which will be further discussed in Chapter 4. The C2 domain interacts with phospholipid membranes in a Ca^{2+}-independent manner. Phosphorylation on the tail of the C2 domain (C-tail, at Ser380, Thr382, Thr383, and Ser385) switched PTEN from an "open" conformation to a "close" conformation, which leads to PTEN dissociation from the membrane [15, 16].

The structure of PTEN is similar to that of dual specificity protein phosphatases, but contains an active site pocket with a larger width to accommodate the PI(3,4,5)P3

headgroup [17]. Furthermore, PTEN contains the signature catalytic motif of protein tyrosine phosphatases, which includes a cysteine residue that engages in nucleophilic attack of the substrate to accomplish cleavage [18].

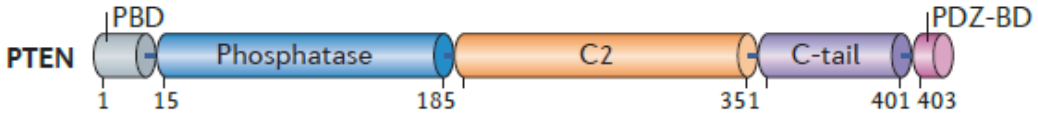

Fig 1.4 Domain structure of phosphatase and tensin homologue (PTEN). This figure is adapted from Ref. [18].

In vivo, PTEN is a known tumor suppressor that shows a loss of activity through mutations or varied expression levels in many types of cancer. Deletion of PTEN is frequently found in prostate and breast cancer [18]. Arg130, Arg173 and Arg233 are common mutation hotspots of PTEN; however, these are not cancer specific. PTEN is involved in several other diseases, including autism, macrocephaly, and Cowden syndrome [19, 20]. Patients with Cowden syndrome have higher risk of getting tumors, including breast (lifetime risk–LR-85%), thyroid (LR35%), kidney (LR33%), and endometrium (LR28%) [21].

1.4 Phosphoinositides

In above two chapters we mentioned PI(4,5)P2 and PI(3,4,5)P3, which belong to the class of phosphoinositide lipids (PIs). PIs, the phosphorylated products of

phosphatidylinositol, play a critical role in cell regulation, including signal transduction mediation and integral protein regulation [22]. There are seven PIs found in cells, including three phosphatidylinositol monophosphates (PI(3)P / PI(4)P / PI(5)P), three phosphatidyl-inositol bisphosphates (PI(3,4)P2 / PI(4,5)P2 / PI(3,5)P2), and a phosphatidylinositol triphosphates (PI(3,4,5)P3), each with a different cellular distribution [23, 24]. For example, PI(4)P and PI(4,5)P2 are mainly distributed on the cell membrane, on the Golgi complex, and on secretory vesicles [25], while PI(3)P and PI(3,5)P2 are mainly concentrated in early endosomes and in late endosomes, respectively [22]. Endosome exocytosis requires the conversion of PI(3)P to PI(4)P, before the recycling endosome is trafficked to the plasma membrane with the assistance of the exocyst [26].

These PIs have a close functional relationship with membrane-bound small GTPases, which are important in mediating signal transduction in the cell. Not only do PIs recruit GTPase activating proteins (GAPs) and guanine nucleotide exchange factors (GEFs) to regulate the activity of numerous small GTPases on the membrane, but they also function as co-receptors with GTPase for cytosolic protein recruitment to specific compartments [22]. PI(4,5)P2 and PI(3,4,5)P3 are often involved in the regulation of actin regulatory proteins on the membrane. For example, PI(4,5)P2 and the small GTPase Cdc42 bind and alleviate the auto-inhibition of N-WASP, which then activate Arp2/3 complex, leading to actin filament nucleation [27, 28]. A subset of class I myosins (ID, IE, and IF) is recruited to the membrane by PI(3,4,5)P3, stimulating actin polymerization during chemotaxis and phagocytosis [29]. Numerous other cell functions are regulated by different PIs: secretory vesicle trafficking from Golgi apparatus to the plasma membrane requires PI(4)P, early

micropinocytosis requires PI(3)P / PI(3,4)P2 [30], and others are summarized in the literature [23].

1.5 Pleckstrin Homology (PH) Domains

Most of the signaling proteins interacting with the PIs in the cell contain pleckstrin homology (PH) domains, which consist of roughly 100 – 120 amino acid residues [31, 32]. Though there is low primary sequence similarity among the different PH domains, they retain a highly conserved 3D core structure, a β-sandwich consisting of two orthogonal β sheets (with three and four β strands, respectively) [33-35]. The PH domains can be grouped based on their interactions with phosphoinositides, including high specificity and affinity (PH of PLCδ1 for PI(4,5)P2 [36, 37]; PH of Btk and Grp1 for PI(3,4,5)P3 [38]), low specificity and / or affinity (i.e. PH of PLC-β, PLC-γ, Gab1), and non-specific binding (PH of DAG K-δ, dynamin) [33].

Signaling proteins bearing PH domain with PI(3,4,5)P3 binding specificity play important roles in regulating cell survival and directional movement [39]. For example, general receptor for 3-phosphoinositide (Grp1) and ADP-ribosylation factor nucleotide binding site opener (ARNO) are two guanine nucleotide exchange factors (GEFs) of ADP-ribosylation factor 6 (ARF6), which is an important mediator of cytoskeleton remodeling [40]. Both Grp1 and ARNO are recruited to the membrane by the interaction of a PH domain with membrane PIs, especially PI(3,4,5)P3 [41, 42].

1.6 Chemotaxis and Cell Polarity

Not only important in cell growth and proliferation, PI(4,5)P2, PI(3,4,5)P3, PI3K and PTEN also play key roles in chemotaxis, which guides cell movement toward chemoattractants. Movement via chemotaxis is crucial in a range of processes including the direction of neutrophils toward infection site, tumor metastasis, and cell movement during embryogenesis [43, 44].

Chemotaxis involves coordination of three processes: gradient sensing, motility, and polarization [45] [46]. *Gradient sensing* refers to a cell's ability to generate an amplified response to a chemoattractant gradient, even while immobile. For example, molecules may distribute spatially polarized on the cell membrane at the front side (e.g. PI3K, PH domain, PI(3,4,5)P3) and at the read side (e.g. PTEN, myosin, PI(4,5)P2) of a gradient. *Polarization* refers to the point at which a cell acquires and maintains leading and trailing edges in response to chemoattractant, even in the presence of a uniform concentration attractant. The third process, *motility*, refers to the cell's ability to extend pseudopodia at the front of cell and retract at the rear side, periodically. Gradient sensing can be explained by the local excitation-global inhibition (LEGI) model, where fast local excitation is triggered by local occupation of receptors and slower global inhibition arises from global occupation of receptors [43, 47]. With the positive feedback and actin cytoskeleton involved, the directional sensing could be stabilized and lead to polarity [48].

Not only important in chemotaxis and directional movement, cell polarity is also important in cell function specialization; for example, the apical and basolateral membranes of photoreceptors function for light sensing and for transducing signal to

underlying neurons, respectively [49]. The asymmetric distribution of PIP2 and PIP3 is common in many cell types, including epithelial cells [50] and *Drosophila* photoreceptor cells [51]. In fact, polarization of epithelial cells is proposed to be caused by PTEN-PI3K bistability [52, 53]. In a recent study, Matsuoka and Ueda conclude that PTEN-PIP3 bistable module, which is generated by the mutual inhibition of PTEN and PIP3, underlies the directional movement of cell's decision-making [54]. The importance and more mechanisms underlying bistability will be discussed further in the next section.

1.7 Ultrasensitivity, Bistability, and Feedback Loop

Before considering bistability more deeply, it is helpful to discuss ultrasensitivity, which is one of the most important mechanisms in creating bistability. The input-output relationship in biochemistry is usually described with the Hill equation: $Output = \frac{Input^n}{K^n + Input^n}$, where n is the Hill coefficient [55]. When $n = 1$, the response is hyperbolic (Michaelian response). When $n > 1$, the response is ultrasensitive. The ultrasensitive input-output response curve is usually sigmoidal, and the response acts more "switch-like" as the Hill coefficient increases (Fig 1.5).

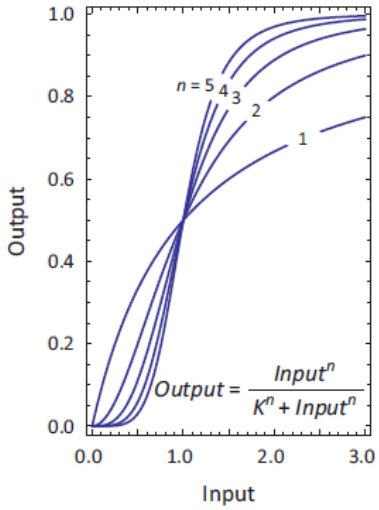

Fig 1.5 Input-output relationships for Hill functions with varying coefficients. Hill coefficient (*n*) is 1 - 5. The relationship behaves more switch-like with increasing Hill coefficient. This figure is adapted from Ref. [55].

Ultrasensitivity is observed in the phosphorylation cycle when both kinase and phosphatase are saturated with substrate. This is termed zero-order ultrasensitivity because the reaction rate is independent with regard to substrate concentration [56]. In addition to enzyme saturation, several additional mechanisms can underlie ultrasensitivity, including multisite phosphorylation and positive feedback [57].

Ultrasensitivity is a key building block in biological systems, particularly in signaling where signals can be amplified and effectively transmitted down a signaling cascade [58]. The S-shaped input-output response, a result of ultrasensitivity, acts as a monostable switch in the system. The initial flat region of this response curve allows it to

filter out the noise in input to remain ‘off’. The system switches to ‘on’ when the signal crosses a certain threshold [58, 59].

When positive feedback is described by a Hill function, the system can more easily establish a bistable response with increasing Hill coefficient [58, 60, 61]. The bistable response acts as switch with built-in memory. This memory is absent in the monostable switch generated from ultrasensitivity [58]. Systems with bistability show hysteresis, in which the output of system depends not only on the present input, but also depends on its recent history [62]. More biological examples with either monostable or bistable switches are examined in the next section.

1.8 Binary Response in Enzyme Activation and Cell Fate Switch

Ultrasensitive responses are important in cell fate decisions and signaling transduction because they allow the cells / enzyme cascades to respond to complicated external stimuli in an all-or-none manner, leading to a binary response [61, 63]. This ultrasensitive, monostable switch is commonly observed in kinase activation process. AMP-activated protein kinase kinase (AMPKK), for example, is shown to be activated by AMP in an ultrasensitive manner with a Hill coefficient of 2.5 [64]. When the cellular energy level is lowered with increasing AMP levels, the AMPK cascade is activated to initiate the catabolic pathway to drive the synthesis of ATP. Another example is Ca^{2+} / camodulin (CaM)-dependent protein kinase II (CAMKII) activation [65]. Ultrasensitive switch-like activation of CAMKII arises from the cooperative binding of Ca^{2+} to CaM, forming a Ca^{2+}-CaM complex, which will subsequently bind to CAMKII. This switch-

like response plays an important role in all-or-none long-term potentiation of hippocampal synapses.

In addition to monostable switches, bistable switches commonly exist in biological systems and are important in cell fate switches. Oocyte maturation, for example, is regulated by the bistable p42 mitogen-activated protein kinase (MAPK) / Cdc2 system [60]. Transient progesterone treatment of immature oocytes can arrest cells in a mature state even when the progesterone is removed, suggesting that the system maintains a "memory" of the stimulus. Separately, a cell's entry into mitosis is controlled by the Cdk1-Cdc25C-Wee1A bistable system, which is created by a positive feedback loop and a negative feedback loop [58].

Several monostable or bistable switches exist in PI3K / Akt / mTOR signaling pathway and play key roles in cell fate determination, including (i). T-cell memory, (ii). insulin response of adipose cells, and (iii). the cell death / survival switch. (i). This pathway leads to the inhibition of the molecular switch of forkhead box O1 (FOXO1) thereby resulting in the promotion of differentiating of effector T-cells [66, 67]. (ii). Bimodal response to insulin stimulation in adipocytes. After insulin stimulation, Akt is phosphorylated to promote the translocation of the glucose transporter GLUT4 to the membrane [68]. Bistability of phosphorylated Akt (pAkt), which is proposed to be established with the help of a positive feedback loop within the PI3K-Akt network, leads to the all-or-none response of GLUT4 transportation to the membrane [69]. This result produces a switch-like behavior to regulate glucose uptake in adipocytes [70]. (iii). Cell death / survival switch. It was shown that bistability of Akt, triggered by a positive

feedback (p53-AKT-Mdm2-p53, involves PIP3 and PTEN) and a negative feedback loop (p53-Mdm2-p53), could be a potential mechanism for cell death and survival switch [71]. Consistent with this result, Arkun indicates that deletion of PTEN disrupts bistability of Akt, which induces proliferation of cancer cells [70].

In the next few sections, three theories are presented. The Langmuir adsorption model is used to measure sensor binding affinity, and transport theory is used to describe enzyme kinetics in a flow chamber. The details of sensor binding and enzyme kinetics experiments are presented in later chapters. Linear stability analysis is used to determine whether a system's steady-state is stable or not. In a later chapter, this tool is applied to PI(3,4,5)P3 / PI(4,5)P2 interconversion equilibrium.

1.9 Langmuir Adsorption Model

The Langmuir adsorption model describes the adsorption of a ligand to a surface at isothermal conditions. Consider binding of ligand *A* to surface receptor *B* to form the complex *AB* on the surface. The reaction is described below:

$$\frac{\partial[AB]}{dt} = k_a[A][B] - k_d[AB] \tag{1.1}$$

$$B_{\max} = [B] + [AB] \tag{1.2}$$

[*A*] (units: μM) is the ligand concentration in the solution, [*B*] (unit: μMm) is the free surface receptor concentration, and [*AB*] (unit: μMm) is the concentration of surface-bound ligand. B_{max} is the total receptor concentration. k_a (unit: $\mu M^{-1}\ s^{-1}$) and k_d (unit: s^{-1})

are the association constant and the dissociation constant, respectively. The unit of surface concentration we will use in this thesis is μMm, which can be easily converted to the commonly used unit number of molecules per square micrometer (1 μMm = $6*10^8$ molecules / μm^2). The derivation of the Langmuir formula is described below.

$$\frac{d[AB]}{dt} = -\frac{d[B]}{dt} = k_a[A][B] - k_d(B_{\max} - [B]) \tag{1.3}$$

Eq. 1.3 can be converted to the standard form of a linear first-order differential equation, Eq. 1.4, and further to Eq. 1.5:

$$\frac{d[B]}{dt} + (k_a[A] + k_d)[B] = k_d B_{\max} \tag{1.4}$$

$$\frac{d}{dt}([B]e^{(k_a[A]+k_d)t}) = k_d B_{\max} e^{(k_a[A]+k_d)t} \tag{1.5}$$

The free receptor B concentration is solved:

$$[B] = e^{-(k_a[A]+k_d)t}\int k_d B_{\max} e^{(k_a[A]+k_d)t} = (\frac{k_d B_{\max}}{k_a[A]+k_d})e^{-(k_a[A]+k_d)t}\{e^{(k_a[A]+k_d)t} + C\} \tag{1.6}$$

At t=0, $[B] = B_{\max}$

$$[B] = (\frac{k_d B_{\max}}{k_a[A]+k_d}) + (\frac{k_a[A]B_{\max}}{k_a[A]+k_d})e^{-(k_a[A]+k_d)t} \tag{1.7}$$

$$[AB] = B_{\max} - [B] = (\frac{k_a[A]B_{\max}}{k_a[A]+k_d})(1 - e^{-(k_a[A]+k_d)t}) \tag{1.8}$$

When the binding reaction reaches equilibrium:

$$[AB]_{eq} = \frac{k_a[A]B_{\max}}{k_a[A]+k_d} = \frac{B_{\max}[A]}{K_D+[A]} \tag{1.9}$$

where $K_D = \frac{k_d}{k_a}$ (1.10)

K_D is the equilibrium dissociation constant. The plot of equilibrium concentration of *AB* versus the ligand concentration is a hyperbola. When [*A*] is equal to K_D, the amount of surface-bound ligand reaches the half-maximum binding site: $[AB]_{eq} = \frac{1}{2} * B_{\max}$. From Eq. 1.8, we notice that the binding kinetics not only depends on the association constant k_a, but also on the dissociation constant k_d. This is because when an association process occurs, a dissociation process also occurs at the same time. Therefore, both k_a and k_d affect ligand binding kinetics. In addition, the binding rate increases with increasing ligand concentration. In summary, the time to reach equilibrium decreases with increasing k_a, k_d, and [*A*].

During dissociation: $[A] = 0$

$$\frac{\partial[AB]}{dt} = -k_d[AB] \tag{1.11}$$

$$[AB] = [AB]_{eq} e^{-k_d t} \tag{1.12}$$

The dissociation process is considered as the absence of ligand in the bulk solution, so the kinetics depend only on k_d.

1.10 Compartment Model and Transport Theory

Binding kinetics can be measured in a flow chamber, which contains surface-immobilized receptors and ligands introduced in a continuous stream. The flow chamber is commonly combined with an optical biosensor method to monitor binding and unbinding reactions. Surface plasmon resonance (SPR) is one of the most commonly used methods in determining affinity and kinetic parameters of ligand-receptor binding, including protein-protein, receptor-drug, lipid membrane-protein, etc. Commercial SPR instrument configuration is based on Kretschmann geometry, consisting of a high refractive index prism, a sensor chip (thin gold film), and an incident light. The binding of a ligand from solution to the membrane is monitored by changes in the intensity and the phase of the light reflected off the sensor surface [72, 73].

However, the ligand binding (or unbinding) kinetics may be affected by the rate of the transport process. When the rate of ligand transport is much lower than binding kinetics, then the observed kinetics is transport-limited [74]. This effect is considered in a kinetic compartment model, which accounts for the presence of a depletion layer near the surface [74-76]. The compartment model divides the flow channel into two compartments and describes the ligand binding with two processes: (i). Ligands introduced into the flow channel enter into the outer compartment, and then transport to the inner compartment. (ii). Only ligands from inner compartment bind to the surface (Fig 1.6). Concentration of ligand in the outer compartment (bulk solution) remains identical to the initial concentration of the injected solution. This model considers the fact that the binding of

ligands to a membrane receptor depends on the kinetics of transport through the bulk solution.

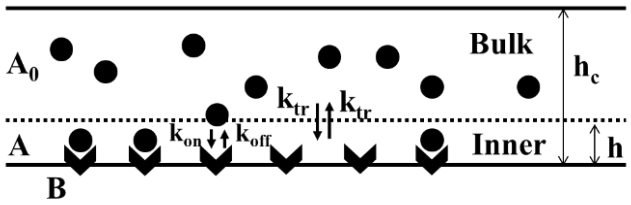

Fig 1.6 Schematic illustration of the compartment model in a system with a planar surface. The bulk solution and inner compartment are separated by the dotted line.

The reaction scheme of the compartment model is reviewed below, along with the corresponding differential equations; Eqs. 1.22 and 1.23:

$$A + B \underset{k_{off}}{\overset{k_{on}}{\rightleftarrows}} AB \qquad\qquad A_0 \underset{k_{tr}}{\overset{k_{tr}}{\rightleftarrows}} A$$

$$\frac{\partial [AB]}{dt} = k_{on}[A][B] - k_{off}[AB] \tag{1.13}$$

$$\frac{\partial [A]}{dt} = \frac{1}{h}\{k_{tr}([A]_0 - [A]) + k_{off}[AB] - k_{on}[A][B]\} \tag{1.14}$$

$[A_0]$ and $[A]$ (units: μM) are the concentration of ligands in the bulk solution (outer compartment) and in the inner compartment, respectively, while $[B]$ (unit: μMm) is the surface receptor concentration within the supported lipid bilayer. $[AB]$ (unit: μMm) is the surface concentration of protein bound to the lipid membrane. The association constant is k_{on} (unit: $\mu M^{-1}\ s^{-1}$), the dissociation constant is k_{off} (unit: s^{-1}), k_{tr} (unit: m/s) is the transport

coefficient of ligands between inner and outer compartment, and h (unit: μm) is the height of the inner compartment. The transport coefficient can be expressed as follows [74]:

$$k_{tr} \sim 0.855 * (\frac{v_c D^2}{h_c x})^{1/3} \tag{1.15}$$

where D is the diffusion coefficient, v_c is the linear flow velocity, h_c is the height of the flow chamber, and x is the distance from the observation point from the inlet. Application of the compartment model to describe sensor binding and enzyme catalysis will be further described in Chapters 3 and 4.

Besides flow chambers, another system we use to characterize interfacial enzyme reactions is the bead-supported membrane (Chapter 7). A schematic illustration of the compartment model on a spherical surface is in Figure 1.7. The radius of circular surface and inner compartment are a and r_i, respectively. [C] is the concentration of ligand in the inner compartment, and [$\bar{C}$] is the bulk concentration of ligand. The reaction scheme is the same as in the planar system, and the formulas are described in Eqs. 1.13 and 1.14.

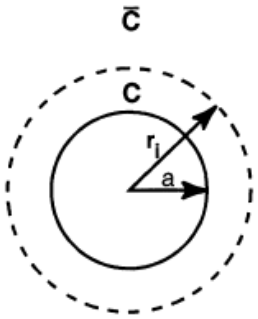

Fig 1.7 Schematic illustration of the compartment model in a system with a spherical surface. The bulk solution and inner compartment are separated by the dotted line. This figure is adapted from Ref. [75].

The transport coefficient between inner and outer compartments of a system with a spherical surface is different than a system with a planar surface in a flow chamber. The transport coefficient in spherical system is expressed as follows [74, 75]:

$$k_{tr} = \frac{k_+}{A} = \frac{4\pi Da}{4\pi a^2} = \frac{D}{a} \tag{1.16}$$

Where k_+ is the diffusion limited forward rate constant, A is the surface area of the spherical reactor, D is the diffusion coefficient, and a is the radius of circular reactor.

1.11 Linear Stability Analysis

In Chapter 7, we solve sets of differential equations to get the equilibrium states of the phosphoinositides PI(4,5)P2 and PI(3,4,5)P3 under different enzyme and sensor protein conditions. These steady-states, however, can be either stable or unstable. In this section, we will introduce a method of stability analysis, which can be used to evaluate the stability of steady-states.

Consider the system: $\dot{x} = f(x, y)\,;\ \dot{y} = g(x, y)$ (1.17)

At the ***fixed point*** x^* and y^*: $f(x^*, y^*) = 0$ and $g(x^*, y^*) = 0$ (1.18)

To evaluate the stability of the fixed point, we'd like to linearize about a fixed point:

Let $u = x - x^*;\ v = y - y^*$ (1.19)

$$\dot{u} = \dot{x} = f(x^* + u, y^* + v) \sim u\frac{\partial f}{\partial x} + v\frac{\partial f}{\partial y} \tag{1.20}$$

$$\dot{v} = \dot{y} = g(x^* + u, y^* + v) \sim u\frac{\partial g}{\partial x} + v\frac{\partial g}{\partial y} \tag{1.21}$$

Combining above two equations and we get the ***linearized system***:

$$\dot{U} = AU \tag{1.22}$$

Where $U = \begin{bmatrix} u \\ v \end{bmatrix}$ (1.23)

and $A = \begin{bmatrix} \frac{\partial f}{\partial x} & \frac{\partial f}{\partial y} \\ \frac{\partial g}{\partial x} & \frac{\partial g}{\partial x} \end{bmatrix}_{(x^*, y^*)}$: the ***Jacobian matrix*** at the fixed point (x^*, y^*) (1.24)

Substitute $U = e^{\lambda t}v$ into $\dot{U} = AU$, and we will get

$$Av = \lambda v \tag{1.25}$$

Where λ is the eigenvalue and v is the eigenvector of matrix A.

(a). When the eigenvalues are real numbers

(i). When all eigenvalues are negative, the fixed point is a *stable point*.

(ii). When all eigenvalues are positive, the fixed point is an un*stable point*.

(iii). When some eigenvalues are positive and some are negative, the fixed point is a *saddle point*.

(i). (ii). (iii).

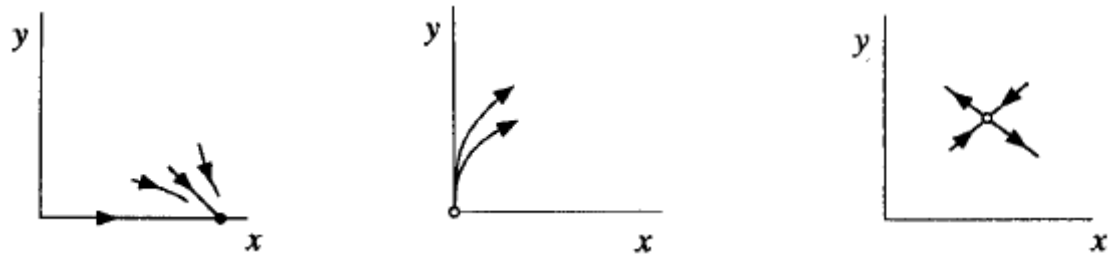

Fig 1.8 Schematic illustration of stable point (i), unstable point (ii), and saddle point (iii). This figure is adapted from Ref. [77].

(b). When the eigenvalues are complex numbers

Assuming two eigenvalues are $\lambda_{1,2} = \alpha + i\omega$

(i). $\alpha = 0$: the fixed point is a *center*

(ii). $\alpha < 0$: the fixed point is a *stable spiral* (decaying oscillation)

(iii). $\alpha > 0$: the fixed point is an un*stable spiral* (growing oscillation)

(i). (ii).

Fig 1.9 Schematic illustration of fixed point of a center (i) and a stable spiral (ii). This figure is adapted from Ref. [77].

In summary, the solution of Eq. 1.25 can be expressed

$$\lambda_{1,2} = \frac{1}{2}(\tau \pm \sqrt{\tau^2 - 4\Delta}) \tag{1.26}$$

Where $\Delta = \lambda_1 * \lambda_2$ (1.27)

$$\tau = \lambda_1 + \lambda_2 \tag{1.28}$$

The type and stability of all different fixed points can be summarized in Figure 1.10.

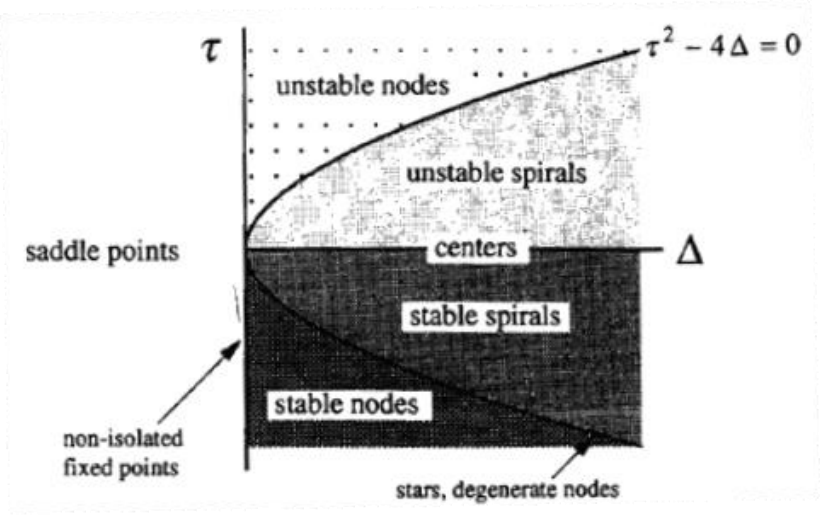

Fig 1.10 Stability diagram of all different types of fixed points. This figure is adapted from Ref. [77].

1.12 Summary

In this chapter, we described and introduced background knowledge for my research. we first established the biological importance of the PI3K-Akt signaling pathway, as well as two important enzymes that will be characterized in Chapters 4-7 of my dissertation, PTEN and PI3K. Next, we characterized the importance of phosphoinositides and their main binding partners, PH domains, which will be characterized in Chapter 3. After introducing each of these enzymes, proteins, and lipids, we discussed the role that these proteins and lipids play in the regulation of cell functioning, including chemotaxis and cell polarization. The collaboration of different proteins leads to complex phenomena, like bistability and ultrasensitivity, which are important in protein activation and cell fate switch. The mechanism that underlies bistability will be further characterized in Chapter

7. In the last two sections, we presented three important theories: Langmuir binding model, which identifies the binding affinity of ligand to receptor, and was used in my research to characterize PH-Grp1 to PI(3,4,5)P3 binding, as well as PH-PLCδ1 to PI(4,5)P2 binding (Chapter 3); Transport effect, which is critical in analyzing binding / unbinding kinetics in flow chamber, and was considered in our theoretical model to describe sensor proteins' binding kinetics, as well as interfacial enzyme kinetics (Chapter 3 and 4, respectively); and a method for linear stability analysis, which was used in evaluating the stability of the steady-state (described in Chapter 7).

CHAPTER 2. Experimental Systems and Methods[3,4]

2.1 Small Unilamellar Vesicle (SUV)

The preparation of Small unilamellar vesicles (SUVs) followed a previously described protocol [78]. Briefly, the desired lipid compositions were prepared to 5 mM stock solutions in the solvent $CHCl_3$: MeOH = 3 : 1. Phospholipids were then spread evenly in a round-bottomed flask followed by vacuum application over two hours. The lipid film was rehydrated with PBS (1X, pH = 7.4) and sonicated in an ultrasonic bath for 40 min. The solution was then freeze-thawed via liquid nitrogen and room-temperature water 4 times and extruded 17 times through a 50 nm filter.

2.2 Si-Bead Supported Lipid Bilayer

Silica beads, 5 µm in diameter, were purchased from Polyscience Inc (Warrington, PA, USA). The beads were washed with PBS (1X, pH = 7.4) three times, and then treated with air plasma for 5 min (medium intensity; Plasma cleaner from HARRICK PLASMA (Ithaca, NJ, USA)). After plasma treatment, the beads (typically an amount of about $3 \cdot 10^4$) were immediately resuspended using 15 µL of a 0.5 mg/ml SUV dispersion and incubated for 30 min for bilayer formation. We note that this involved a more than 1000-fold excess of SUV area compared to bead surface area, in order to facilitate rapid

[3] Parts of this chapter are reproduced by previously published work: Liu, C.; Deb, S.; Ferreira, V. S.; Xu, E.; Baumgart, T., Kinetics of PTEN-mediated PI(3,4,5)P3 hydrolysis on solid supported membranes. *PLoS One* **2018,** *13* (2).

[4] Parts of this chapter are reproduced by currently submitted work: Liu, C.; Zimmerman, Z. E.; Grasso, M.; Gosh, A.; Marmorstein, R.; Radhakrishnan, R.; Baumgart, T., Bistable reaction behavior in PTEN / PI3K mediated phosphoinositide lipid conversion.

formation of high quality bead-supported bilayer membranes. BSMs were then washed with PBS to remove the remaining vesicles.

2.3 Protein Expression and Purification

2.3.1 mCherry-PH-Grp1

The PH domain (267-399) of human Grp1 [79, 80] was cloned by the company VectorBuilder (Santa Clara, CA, USA) into the pET16b vector, with a C-terminal 6x His tag and mCherry at the N-terminus. The plasmid was obtained in *E. coli* Stbl3 cells, and we extracted it with a PureYield miniprep kit (Promega, Madison, WI, USA). Protein purification procedures were described previously [78, 80] and were used with minor modifications. Briefly, mCherry-PHGrp1 was expressed in *E. coli* BL21-(DE3) cells after induction with 500 μM isopropyl-β-d-thiogalactoside (IPTG) at 37 ^{o}C for 4 hours. After lysis through tip sonication (used for all proteins expressed for this project), the supernatant was purified with a His trap affinity column (GE, Piscataway, NJ) followed by size exclusion chromatography with a Superdex 200 16/600 column.

2.3.2 EGFP-PH-PLCδ1

The PH domain (1-170) of human phospholipase C delta 1 (PLCδ1) [81, 82] was cloned into the pET16b vector with an N-terminal GST-tag and C-terminal EGFP via VectorBuilder and extracted as described above. The EGFP-PH-PLCδ1 was expressed in *E. coli* BL21-(DE3) cells and was induced with 100 μM IPTG at 18 ^{o}C for 21 hours. The

expressed proteins were extracted by a GST affinity column, eluted, and then digested with PreScission protease. The resulting solution was further purified by size exclusion chromatography with a Superdex 200 16/600 column.

2.3.3 PI3Kα (p110α-niSH2)

The plasmid of human PI3Kα (p110α-niSH2) was obtained from Addgene, Cambridge, MA, USA). The niSH2 domain of p85α (322-600) and the p110α (1-1068) subunit [83] were each separately cloned into separate Pfastbac1 vectors and then coexpressed in Sf9 insect cell for 48 hours. Supernatant resulting from cell lysis was purified using a Ni-NTA resin (Thermo Fisher Scientific, Philadelphia, PA, USA). The proteins were further purified through an anion exchange (Hi Trap Q) and size exclusion chromatography (Superdex 200 Increase 10/300).

2.3.4 PTEN (WT) with double HisTag

The full length (1-403) human PTEN (plasmid get from Addgene, originally deposited by Dr. Ross [84]) was cloned into the pET16b vector with a double 6x His at the C-terminus via VectorBuilder and extracted as above. The double HisTag was shown to improve the binding of the protein to the Ni-NTA column [85], which enabled us to use a washing buffer containing 100 mM imidazole buffer in order to reduce non-specific binding of proteins to the affinity column. By using this method, we were able to eliminate the anion exchange (Hi Trap Q) step from our previous procedure [78]. After

elution of the target protein from the Ni-NTA column it was further purified with size exclusion chromatography. Other PTEN purification procedures were as described previously [78, 86] with minor modifications. Briefly, *E. coli* BL21-(DE3) transformed with the PTEN expression plasmid were grown at 37^{o}C, followed by transfer to 18 ^{o}C for 20 min when the OD at 600 nm reached ~0.5. Protein expression was then induced with 50 μM IPTG and was grown at 20 ^{o}C for 21 hours. The cell was then harvested and lysed with tip sonication in 20 mM phosphate binding buffer with 500 mM NaCl, 20 mM Imidazole, and 10 mM 2-Mercaptoethanol (BME) at pH = 7.4. After passing the supernatant onto the His trap affinity column (GE, Piscataway, NJ), the column was first washed with the binding buffer, followed by an additional washing step using a buffer containing 20 mM phosphate, 500 mM NaCl, 100 mM Imidazole, pH = 7.4, for 10 column volumes. The proteins were then eluted in the following buffer (20 mM phosphate, 500 mM NaCl, 500 mM Imidazole, pH = 7.4) and further purified by size exclusion chromatography (Superdex 200 16/600). Finally, 10 mM dithiothreitol (DTT) was added and the resulting solution was stored at 4 ˚C.

2.3.5 Doubly phosphorylated peptide (pY2)

The doubly phosphorylated peptide (pY2) used to activate PI3K was synthesized by the company GenScript (Piscataway, NJ, USA). The peptide was acetylated on the N-terminus, and was amidated at the C-terminus. These modifications protect peptide from enzymatic degradation. The sequence of peptide was ESDGGpYMDMSKDESVD pYVPMLDMKGDVKYADIE, where pY indicates phosphorylated tyrosine. This peptide

sequence derives from the human platelet-derived growth factor receptor beta (PGFRB; residues 735-767 with Y740 and Y751) and it has been shown to bind to the p85 N-terminal SH2 domain [87], leading to release of inhibition of the p110 catalytic domain of PI3K.

2.3.6 PTEN (WT)

A pET30b vector containing PTEN was obtained from Addgene. The protein was expressed and purified as previously described by Ross and Gericke [86]. Briefly, PTEN was expressed in Escherichia coli BL21-(DE3) cells grown in Rich media at 37^{o}C. Protein expression was induced with 50 µM isopropyl-β-d-thiogalactoside (IPTG) at 20 ^{o}C for 21 hours. Cells were harvested by centrifugation and the pellets were resuspended in a pH=7.4 buffer containing 500 mM NaCl, 10 mM 2-mercaptoethanol in 20 mM phosphate buffer. The cells were lysed by tip sonication and centrifuged at 4 ℃. The supernatant was applied to a His trap affinity column (GE, Piscataway, NJ). The protein was further purified by size exclusion and anion-exchange chromatography, and stored on ice after dithiothreitol (DTT) was added at a concentration of 10 mM.

2.3.7 YFP-PH-Grp1

A plasmid for YFP-PHGrp1 was kindly provided by Prof. T. Balla (National Institutes of Health, NIH). The fusion protein was purified as previously described [80]. YFP-PHGrp1 was expressed in BL21-(DE3) cells and grown in Rich media at 37^{o}C.

Induction occurred with 200 μM IPTG at 18 ^{o}C, and proteins were expressed for 16 hours. The fusion protein was purified by His trap affinity and size exclusion chromatography, successively.

2.4 Ibidi Flow Chamber Fabrication and Supported Lipid Bilayer Preparation

μ-Slide VI 0.4 flow chambers were obtained from Ibidi (Martinsried, Germany). Glass slides were cleaned by sonicating in 2% Hellmanex solution (Hellma, Mullheim, Germany) for 30 min and then rinsed with water. Subsequently, they were further treated with NOCHROMIX (Godax Laboratories, Inc) and concentrated H_2SO_4 for at least 6 hours, and then extensively rinsed with water. The glass slide was plasma cleaned and attached to the Ibidi chamber with double-sided tape around, forming a closed chamber with inlet and outlet. The buffer (20 mM HEPES / 150 mM NaCl, pH=7.4) was injected to test whether leakage occurs. Small unilamellar vesicles (SUV) were then injected and incubated for 30 min to form the supported lipid bilayer. Any excess SUVs were washed out with buffer. The picture and schematic illustration of Ibidi flow chamber are in Figure 2.1.

2.5 PDMS Channel Fabrication and Supported Lipid Bilayer Preparation

The PDMS **(**Dow Corning Sylgard 184**)** was obtained from Dow Corning (Midland, Maryland, U.S.A). The product consists of a silicone elastomer and a curing agent. To make the PDMS chamber, the silicone elastomer was mixed with curing agent with the

ratio 10 : 1 by mass in a 50 mL polypropylene centrifuge tube, then transferred to a patterned Si wafer (procedures described in Chapter 2.7) and cured in a 50^{o}C oven for 1 day. The cured PDMS chamber was cut and was peeled off from the wafer, immersed in hexane for 1.5 days to remove PDMS oligomer from cross-linked polymer, and then deswelled slowly in toluene (1 day), ethyl acetate (half day), and acetone (half day) [88]. The extracted PDMS was then dried in a 50^{o}C oven for 2 - 3 days and stored in a petri dish.

For the chamber fabrication, both the extracted PDMS and the glass slide (cleaned with sulfuric acid and NOCHROMIX; described in section 2.4) were treated with oxygen plasma for 45 s, then adhered together irreversibly [89]. SUVs were added into the channel and incubated for 30 min to allow for bilayer formation. Tubes were then connected to the inlet and outlet, respectively, to wash out the remaining SUV with buffer. The picture and schematic illustration of PDMS flow chamber are in Figure 2.1.

(A). (B).

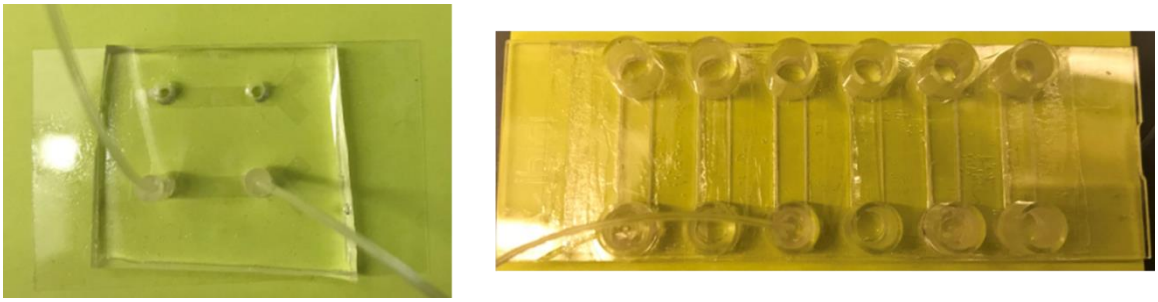

(C).

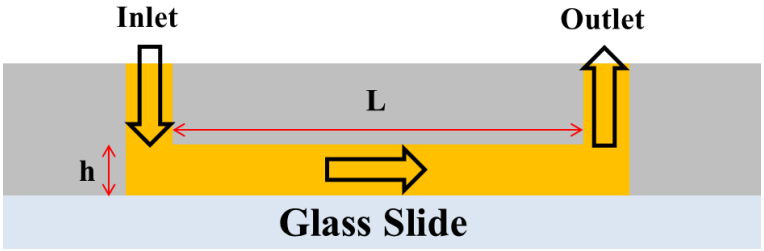

Fig 2.1 Different types of flow chambers. (A). PDMS channels, with the channel dimensions: Length (L) = 15 mm; Height (h) = 40 μm; Width (w) = 2 mm. (B). Ibidi chambers, with the channel dimensions: Length (L) = 20 mm; Height (h) = 515 μm; Width (w) = 3 mm. (C). Schematic illustration of channels with inlet and outlet.

2.6 Imaging Chambers for BSMs Observation

Holes were drilled into polystyrene Petri Dish (Fisher Scientific) with a 1/16 inch drill bit. Vacuum grease (Dow Corning) was spread uniformly around each hole, and a piece of acid-cleaned glass (see [32]) was attached to form an observation chamber. To reduce the adsorption of protein on the glass and chamber walls, the chamber was passivated with 5 mg/mL casein (Fisher Scientific) over 10 min. To prevent sample evaporation, chambers were covered with microcentrifuge tube caps.

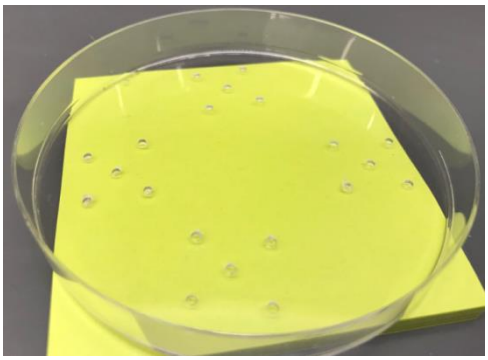

Fig 2.2 Imaging chambers for BSMs observation. Holes size: 1 / 16 inch in diameter.

2.7 Making Patterns on Si Wafer by Lithography

Patterned Si wafer, which is used as a template to make PDMS channels, is made by Dr. Ningwei Li in Dr. Stebe lab. Procedures are listed below:

(i). OmniCoat on four inch Si wafer: 500 rpm for 5 s → 3000 rpm for 30 s, then bake at 200 ^{o}C for 1 min.

(ii). Spin coating SU8 2150 photoresist on Si wafer: 500 rpm for 20 s → 8000 rpm for 1 min

(iii). Soft bake: 65 ^{o}C for 20 min → 93 ^{o}C for 60 min → 65 ^{o}C for 20 min

(iv). UV exposure: Expose Si wafer with 240 – 260 mJ/cm^2 UV through a photomask. The power of the lamp was measured before the exposure, and exposure time were calculated accordingly.

(v). Hard bake: 68 ^{o}C for 10 min → 95 ^{o}C for 20 min → 68 ^{o}C for 10 min

(vi). Leave it in oven overnight: 68 ^{o}C at first, then cool down slowly. The oven was turned off when the sample was in, so that the temperature will drop slowly overnight.

2.8 Preparation of KRas4b-Functionalized Supported Lipid Bilayer

1,2-dipalmitoyl-sn-glycero-3-phosphoethanolamine-N-[4-(p-maleimidomethyl)cyclohexane-carboxamide] (16:0 PE MCC, which is abbreviated as mCCPE below) is mixed with other lipid components to make SUVs, and then SUVs are used to make supported lipid bilayers in the flow chamber. Procedures are described above in Chapter 2.1, 2.4, and 2.5. KRas4b (40 μM) was first mixed with GTPγS for an hour on ice. Then Kras4b-GTPγS was loaded into the chamber and incubated with a bilayer for 2 hours at room temperature. After the coupling reaction, excess mCCPE was quenched with 10 mM β-mercaptoethanol (BME) for 20 minutes, then the bilayer was washed with buffer and used within a few hours for eznyme experiments.

CHAPTER 3: Phosphoinositides and PH Domains for Membrane PI(3,4,5)P3 and PI(4,5)P2 Binding[5,6]

In the current study, we use the PH domain of PLCδ1 (PH-PLCδ1) and the PH domain of Grp1 (PH-Grp1) to detect PI(4,5)P2 (referred to as PIP2 below) and PI(3,4,5)P3 (referred to as PIP3 below) on a supported lipid bilayer (their interconversion by a kinase / phosphatase pair is discussed in a later chapter). In section 3.1, we test the specific binding of EGFP-PH-PLCδ1 and mCherry-PH-Grp1 to PIP2 and PIP3, respectively, on a Si bead supported lipid bilayer (BSM). This BSM system is then used to characterize the steady-state of PIP2 and PIP3 interconversion by the PI3K and PTEN in Chapter 7. In section 3.2 we characterize the specific binding of YFP-PH-Grp1 and the association / dissociation kinetics on the glass-supported lipid bilayer in the flow chamber. This flow chamber system will then be used to characterize PTEN-mediated PIP3 dephosphorylation (Chapter 4), PI3K-mediated PIP2 phosphorylation (Chapter 5), and KRas activated PI3K kinetics (Chapter 6).

[5] Parts of this chapter are reproduced by previously published work: Liu, C.; Deb, S.; Ferreira, V. S.; Xu, E.; Baumgart, T., Kinetics of PTEN-mediated PI(3,4,5)P3 hydrolysis on solid supported membranes. *PLoS One* **2018,** *13* (2).

[6] Parts of this chapter are reproduced by currently submitted work: Liu, C.; Zimmerman, Z. E.; Grasso, M.; Gosh, A.; Marmorstein, R.; Radhakrishnan, R.; Baumgart, T., Bistable reaction behavior in PTEN / PI3K mediated phosphoinositide lipid conversion.

3.1 Specific Binding of PIP3 and PIP2 by mCherry-PH-Grp1 and EGFP-PH-PLCδ1, Respectively.

To be able to observe PIP3 and PIP2 contained in lipid bilayer membranes in the absence (this Chapter) and the presence of the kinase PI3K and phosphatase PTEN (in Chapter 7), we designed a fluorescent sensor approach (Fig 3.1A; more details with enzymes involved will be discussed in Chapter 7) based on a silica bead-supported lipid bilayer (BSM) platform (Fig 3.1B). Supported lipid bilayers were prepared by vesicle fusion [90-92] on the beads. The pleckstrin homology (PH) domain of PLCδ1 [81, 82] labeled with EGFP (green, EGFP-PH-PLCδ1), was chosen as a fluorescent sensor to detect PIP2, while the PH domain of Grp1 [80] labeled with mCherry (red, mCherry-PH-Grp1) functioned as a sensor for PIP3. After mixing BSMs with sensor proteins in microcentrifuge tubes, samples were transferred to an observation chamber and imaged by confocal microscopy (Fig 3.1B).

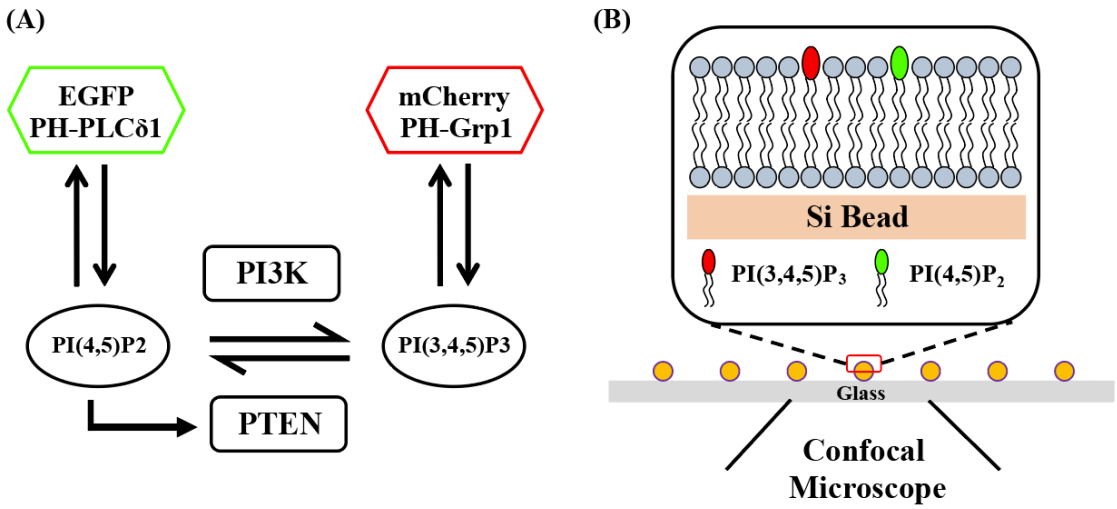

Fig 3.1. Experimental design to study phosphoinositide interconversion by a kinase-phosphatase pair on a model lipid membrane. (A). Molecular scheme of phosphorylation-dephosphorylation cycle catalyzed by PI3K and PTEN, with positive feedback of PIP2 to PTEN. PIP2 and PIP3 are detected with the fluorescent sensor proteins EGFP-PH-PLCδ1 and mCherry-PH-Grp1, respectively. (B). Schematic illustration of bead-supported lipid bilayer membrane (BSM) system.

We characterized the phosphoinositide-specific membrane binding of the two sensors in our model membrane system. The sensor proteins mCherry-PH-Grp1 and EGFP-PH-PLCδ1 were separately mixed with BSMs and fluorescence intensities were determined on the membranes as a function of bulk sensor concentration. The resulting data were fitted with the Langmuir adsorption isotherm: $\frac{I^R_{\max}[P]}{K_d+[P]}$ (details described in Chapter 1.9), where P is the bulk concentration of sensors, $I^R_{\max}$ is the fluorescence intensity at maximal sensor binding to the membrane, and K_d is the equilibrium dissociation constant (Fig 3.2A). The agreement between fit curve and experimental data is consistent with a Langmuir binding mechanism, and the resulting K_d values enabled a rational choice of biosensor concentrations for the monitoring of interfacial catalysis, detailed below.

Having in mind typical physiological PIP2 contents of the plasma membrane of mammalian cells, for the following experiments we chose a range of individual PI lipid contents within our BSMs between 0 – 2 Mol%, while fixing the total PI content in our membranes. We experimentally evaluated the relation between phosphoinositide content ratio and the resulting biosensor fluorescence intensities at the membrane. BSMs with

systematically varied ratios of PIP3 and PIP2 were simultaneously mixed with both sensor proteins at a bulk concentration equal to the K_d value of each fluorescent sensor, determined in Fig 3.2A.

The fluorescence intensities both of membrane-bound mCherry-PH-Grp1 and EGFP-PH-PLCδ1 are proportional to the percent of PIP3 and PIP2 contained in the membrane, respectively (see Fig 3.2B). The linear dependence of binding on the binding site density in both cases is consistent with 1:1 binding of PIP-lipid to fluorescent sensors, and it also indicates minimal sensor interference of binding. Representative fluorescence images, as well as for each PI lipid ratio the corresponding histograms of fluorescence intensity ratios, are shown in Fig 3.2C. For reasons of symmetry, histogram abscissa scaling was chosen to be logarithmic, spanning a linear range of PIP2/PIP3 sensor fluorescence between 1/3 and 3, with values outside of this range combined in the two bins corresponding to these thresholds. We note that all three histograms show monomodal distributions as expected (also note that the logarithmic scale broadens the histogram for the case of the equal PIP lipid ratio BSMs). The BSM system is further used to characterize the PIP2 and PIP3 interconversion by PI3K and PTEN in Chapter 7.

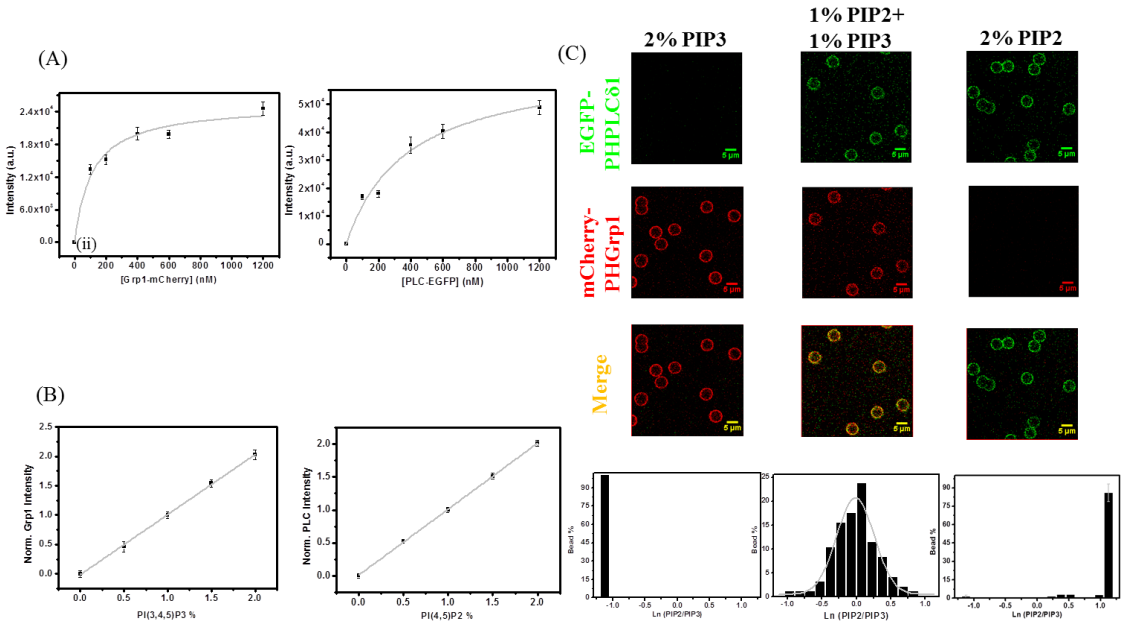

Fig 3.2 PIP2 and PIP3 on Si bead-supported lipid bilayer are bound site specifically with two sensor proteins EGFP-PH-PLCδ1 and mCherry-PH-Grp1, respectively.

(A). Binding isotherm of mCherry-PH-Grp1 (with K_d = 110 ± 27 nM) (left) and EGFP-PH-PLCδ1 (with K_d = 375 ± 95 nM) (right) on Si bead-supported lipid bilayer 1% PIP3 / 1% PIP2 / 5% DOPS / DOPC / 0.2% Naphthopyrene.

(B). Binding of mCherry-PH-Grp1 (left) and EGFP-PH-PLCδ1 (right) on (2-*n*)% PIP3 / n% PIP2 / 5% DOPS / 92.8% DOPC / 0.2% Naphothopyrene bilayer. *n* = 0, 0.5, 1, 1.5, 2. The bulk concentration of mCherry-PH-Grp1 and EGFP-PH-PLCδ1 are 110 nM and 375 nM, respectively. Data points are mean ± SEM (Number of beads ≧ 70, *N* = 2).

(C). Representative images of sensor proteins binding and the histogram PIP2 and PIP3 distribution on the bilayer 2% PIP3 (left column, number of beads ≧ 90), 1% PIP3 + 1% PIP2 (middle column, number of beads = 97; The Gaussian curve is shown in grey), and 2% PIP2 (right column, number of beads ≧ 90). The scale bar on the images is 5 μm.

The remaining lipid compositions in bilayer are 5% DOPS / DOPC / 0.2% Naphthopyrene. The bulk concentration of mCherry-PH-Grp1 and EGFP-PH-PLCδ1 are 110 nM and 375 nM, respectively. For the channels of images, from top to bottom are: EGFP-PH-PLCδ1 channel, mCherry-PH-Grp1 channel, and the merge channel.

3.2 Association and Dissociation Kinetics / Binding Isotherm of YFP-PH-Grp1

In order to quantitatively study association and dissociation kinetics of YFP-PH-Grp1 to the PIP3-containing membrane, we used a fluorescence approach based on solid supported lipid bilayer (SSB) membranes in a flow chamber (Fig 3.3A). SSBs were produced via injection and subsequent fusion of PIP3-containing small unilamellar vesicles (SUV) to a microscope cover slide which sealed an Ibidi flow chamber. The YFP-PH-Grp1 and buffer were injected sequentially into the measurement chamber at a flow velocity of 1 cm/s, and its signal on the membrane surface was monitored through total internal reflection fluorescence microscopy (TIRF) imaging. We determined the deadtime of the flow chamber for a series of flow velocity (Figure 3.5). At a flow velocity of 1 cm/s, we found a dead time of about 2 s, which is substantially shorter than the time frame over which relevant membrane mediated kinetics occurred.

(A) (B)

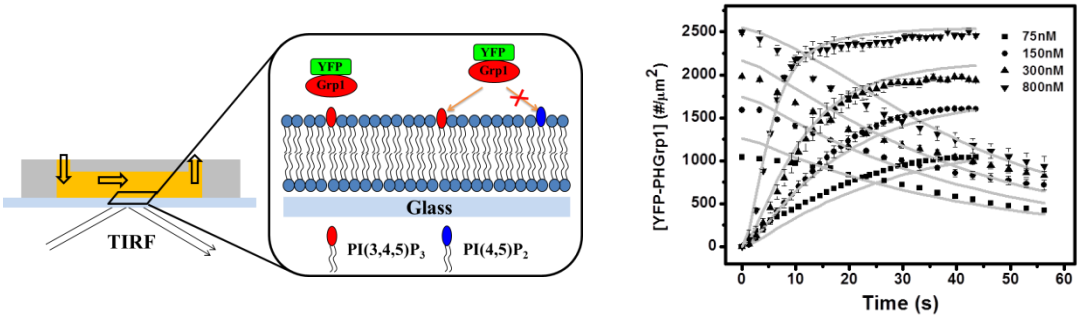

Fig 3.3 Association and Dissociation of YFP-PH-Grp1 on supported lipid bilayer in flow chamber. (A) Schematic illustration of the flow chamber / TIRF detection system. Small unilamellar vesicles (SUV) were injected to form a supported lipid bilayer on the glass surface. Subsequently, YFP-PH-Grp1 and buffer were injected sequentially into the measurement chamber, and the YFP-PH-Grp1 signal change on the membrane is monitored by TIRF microscopy imaging. (B) YFP-PH-Grp1 association and dissociation curves at 0.2% PIP3 / 5% DOPS / 94.6% DOPC / 0.2% TR-DHPE membrane. The y-axis represents the surface concentration of YFP-PH-Grp1. The bulk concentrations of YFP-PH-Grp1 for association kinetics measurements are 75 nM (square), 150 nM (circle), 300 nM (triangle), 800 nM (down-pointing triangle), respectively. After the signals reached their plateau values, buffer was injected to initiate YFP-PH-Grp1 dissociation kinetics. The data were globally fitted with a compartment model (Fig 3.3C, Eqs. 1-2), the fitting curves are shown as grey lines. The value of the fitting parameters are k_a^{Grp1} =1.68±0.18 $\mu M^{-1}s^{-1}$, k_d^{Grp1} =0.16±0.02 s^{-1}, k_{tr}=(1.50±0.20)*10^{-6} m/s, and h=17.83±2.23 μm. Data points are mean ± SEM (typically $N \geqq 3$, but always $N \geqq 2$ measurements). The uncertainty of fit parameters is standard deviation.

We then describe the association and dissociation kinetics of YFP-PH-Grp1 on the membrane (Fig 3.3B). Solutions with different concentrations of YFP-PH-Grp1 were injected in order to measure association kinetics. Buffer was subsequently injected at a flow velocity of 1 cm/s to study dissociation kinetics. We fitted the data with a kinetic compartment model discussed in Chapter 1.10.

We determined an association constant k_a^{Grp1} for YFP-PH-Grp1 of 1.68±0.18 $\mu M^{-1} s^{-1}$ and a dissociation constant k_d^{Grp1} of 0.16±0.02 s^{-1}. These values are close to previously determined values measured by stopped flow on PC / Dansyl-PE / PIP3 (92 / 5 / 3) membranes [93]. Although in the literature the membrane contains a higher concentration of PIP3, we would only expect it to change the observed binding / unbinding rates but not the rate constants k_{on} and k_{off}. More details about the binding / unbinding rates are discussed in the Chapter 3.3. The transport coefficient calculated based on the Eq. 1.15 (with D=100 $\mu m^2/s$, v_c=1 cm/s, h_c=515 µm, x=1 cm in our system) is $2.3*10^{-6}$ m/s, which is close to our fitted value of $1.5*10^{-6}$ m/s (see Table 3.1). The height of the inner compartment can be estimated by the thickness of the Nernst boundary layer, which can be expressed as follows [94]:

$$\delta_N = D^{\frac{1}{3}} u^{\frac{1}{6}} \left(\frac{x}{v_c}\right)^{\frac{1}{2}} \tag{3.1}$$

where u is the kinematic viscosity (u=10^{-6} m^2/s; D, v_c, and x are the same as above). The thickness of the calculated boundary layer is 46 µm, which is of the same order of magnitude as the fitted value of 18 µm (see Table 3.1).

To exclude the possibility that PIP2 affects YFP-PH-Grp1 binding under our

experimental conditions. For these purposes, we obtained YFP-PH-Grp1 binding isotherms among bilayers containing 0% and 0.6% PIP2, respectively (Fig 3.4). Here we used 0.6% PIP2 because it refers to the maximal PIP2 content of membranes used for PTEN-mediated hydrolysis experiments described in Chap 4. Binding data were fitted with the Langmuir adsorption isotherm: $\frac{I^R_{\max}[P]}{K_d+[P]}$. $I^R_{\max}$ is the fluorescence intensity at surface saturation and is expressed in arbitrary units of the detector signal using the same gain setting for each isotherm. We obtained identical (within experimental uncertainties) $I^R_{\max}$ and K_d values for YFP-PH-Grp1 on both membrane types (For 0% PIP2: $I^R_{\max}$ =9612.30±132.42 (a.u) and K_d=126.51±6.07 nM; 0.6% PIP2: $I^R_{\max}$ =9526.64±265.70 (a.u) and K_d=116.91±11.74 nM). This agrees with literature findings showing that PH-Grp1 has high specificity towards PIP3 over PIP2 [41, 95]. These findings justify the exclusion of the influence of PIP2 content on YFP-PH Grp1 membrane binding.

Table 3.1. Value of fitting parameters obtained for fits to data shown in Fig 3.2B

	Parameters	Values	Literature value
k_a^{Grp1}	**Association rate of Grp1 to the lipid bilayer**	**1.7±0.2 μM^{-1} s^{-1}**	**2.95 μM^{-1} s^{-1} (ref [93])***
k_d^{Grp1}	**Dissociation rate of Grp1**	**0.16±0.02 s^{-1}**	**0.28 s^{-1} (ref [93])**

	from the lipid bilayer		
k_{tr}	**Transport coefficient**	**$(1.5\pm0.2)*10^{-6}$ m/s**	**$2.3*10^{-6}$ m/s (calculation) ****
h	**Height of inner compartment**	**18±2 µm**	**46 µm (calculation)****

*** Unit conversion for parameter comparison will be discussed in Chapter 3.3.**

**** The calculation of k_{tr} and *h* is shown in the main text and described by formula 1.15 and 3.1, respectively.**

The uncertainty of the fit parameters is the standard error.

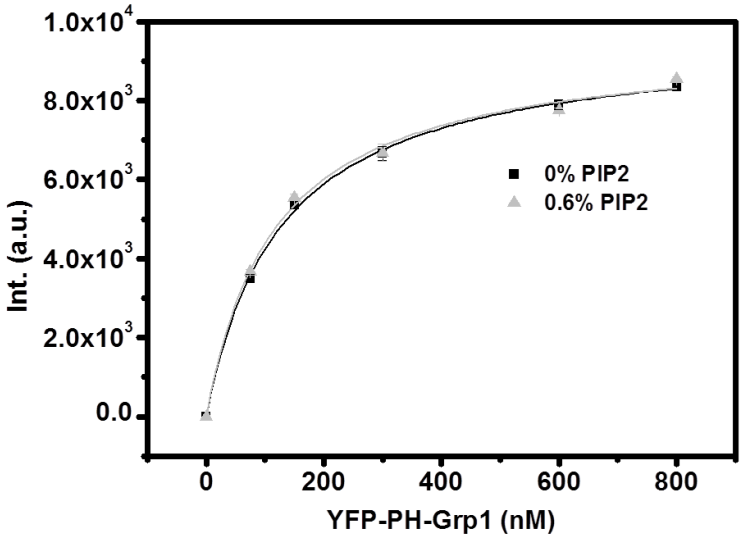

Fig 3.4 Binding isotherm of YFP-PH-Grp1. Binding isotherm of YFP-PH-Grp1 on 0.2% PIP3 / 5% DOPS / 94.6% DOPC / 0.2% TR-DHPE (square, with I^R_{max}

=9612.30±132.42 (a.u) and K_d=126.51±6.07 nM) and 0.6% PIP2 / 0.2% PIP3 / 5% DOPS / 94% DOPC / 0.2% TR-DHPE (triangle, with I_{max}^{R} =9526.64±265.70 (a.u) and K_d=116.91±11.74 nM). Data points are mean ± standard errors of the mean (SEM) for N = 3 measurements. The uncertainty of fit parameters K_d and I_{max}^{R} is standard deviation. The solid lines represent the best fit of experimental data using Langmuir isotherm formula $\frac{I_{max}^{R}[P]}{K_d+[P]}$.

3.3 Dead Time Measurement and the Association Constant of Grp1 Comparison

To establish the speed with which the YFP-PH-Grp1 reaches the desired bulk concentration through continuous flow in our measurement chamber, we prepared a supported lipid bilayer without PIP3 (composition 5% DOPS + 94.8% DOPC + 0.2% TR-DHPE) on a glass cover slip to prevent non-specific binding of YFP-PH-Grp1. Then we injected 600 nM YFP-PH-Grp1 with different flow rates and observed the resulting fluorescence signal in the solution through confocal microscopy imaging. The data was fitted with a single exponential function and the inverse rate constant was defined as the dead time of the flow chamber. The flow rate for our experiments described in the main text was 1 cm/s, so the dead time was ~2 s.

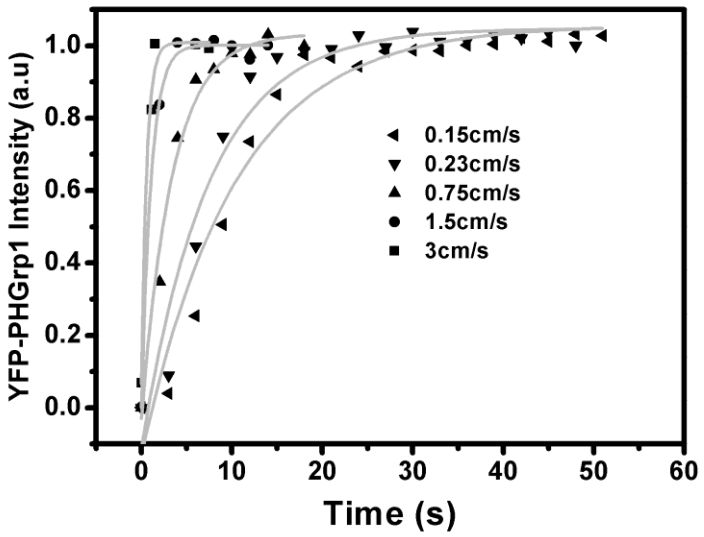

Fig 3.5 Dead time of flow chamber measurement. 600 nM YFP-PH-Grp1 was injected into chamber with a flow rate of 0.15 (left-pointing triangle), 0.23 (down-pointing triangle), 0.75 (triangle), 1.5 (circle), 3 (square) cm/s, respectively. A supported lipid bilayer (5% DOPS + 94.8% DOPC + 0.2% TR-DHPE) was spread on the glass surface to prevent non-specific binding of YFP-PH-Grp1. The YFP-PH-Grp1 signal in solution is monitored by confocal microscopy. The kinetic data was fit with single exponential function: t_{mix} = 10.29±1.34 s (0.15 cm/s), 7.46±0.95 s (0.23 cm/s), 3.41±0.43 s (0.75 cm/s), 1.07±0.09 s (1.5 cm/s), and 0.58±0.14 s (3 cm/s).

3.3.1 Comparison between Association Rate Constant of Grp1 and Literature Value

Lai et al. used a stopped-flow technique with FRET readout to measure association and dissociation rate constants of PH-Grp1 binding to PIP3 [93]. However, they defined

the association rather constant based on the accessible PIP concentration rather than Grp1 concentration. To compare their findings with our result, a conversion is required. According to the Langmuir adsorption model, ligand binding kinetics is described as;

$$[AB] = \frac{k_{on}[A]}{k_{on}[A] + k_{off}} B_{\max}(1 - e^{-(k_{on}[A]+k_{off})t}) \qquad k_{obs} = k_{on}[A] + k_{off} \tag{3.2}$$

[A]: Solution ligand concentration

$B_{\max}$: Maximum binding site on the surface

[AB]: Surface concentration of ligand-receptor complex

The above formula is usually being used to describe ligand binding kinetics in SPR experiments, where the total surface receptor concentration is fixed while varying the solution ligand concentration. However, we can also fix the solution ligand concentration and vary the surface receptor concentration and to obtain the following formula:

$$[AB] = \frac{k_{on}[B]}{k_{on}[B] + k_{off}} A_{\max}(1 - e^{-(k_{on}[B]+k_{off})t}) \qquad k_{obs} = k_{on}[B] + k_{off} \tag{3.3}$$

The observed rate constant for binding kinetics described by Eqs. 3.2 and 3.3 are identical. Accordingly, we can convert it by multiplying k_{on} by the PIP3 concentration and divide by the Grp1 concentration. For a lipid composition of PC / Dansyl-PE / PIP3 = 92:5:3, k_{on} was found [93] to be 0.58 μM^{-1} s^{-1} (with PIP3 concentration) which converts to 2.95 μM^{-1} s^{-1} (with Grp1 concentration). For a second composition used in that study: PC / PS / Dansyl-PE / PIP3 = 69:23:5:3, k_{on} was found [93] to be 2.04 s^{-1} μM^{-1} (with PIP3

concentration) which converts to 11.94 μM^{-1} s^{-1} (with Grp1 concentration). Accordingly, the association rate constant of 1.68 μM^{-1} s^{-1} that we obtained here (see table 3.1) is more similar to the association rate constant determined in ref [93] in the absence of PS lipids, which is reasonable given the low PS content of our membranes (5%).

3.4 Summary

In this chapter, we systematically characterized the binding of sensor proteins with phosphoinositides. First, a linear relationship between membrane-bound PH-Grp1 and PIP3 amount as well as membrane-bound PH-PLCδ1 and PIP2 amount was identified. This result is not only consistent with the expected 1:1 binding of PH-Grp1 to PIP3 and PH-PLCδ1 to PIP2, but is also an indication of minimal sensor interference to binding. Next, association and dissociation kinetics of PH-Grp1 to the PIP3-containing lipid membrane is characterized in the flow chamber. The kinetic parameters of the binding / unbinding of PH-Grp1 that we extracted are comparable to previous literature values, indicating that the compartment model we used is sufficient to describe protein binding in the flow chamber. The fitted values of the height of inner compartment and the transport coefficient are also consistent with the calculated values based on Eqs. 1.15 and 3.1. After confirming the effectiveness of the compartment model, we'll incorporate it into the kinetic model to characterize PTEN-mediated PIP3 hydrolysis, which will be described in next chapter.

Chapter 4: Kinetics of PTEN-mediated PIP3 Dephosphorylation on Solid Supported Lipid Bilayer[7]

PTEN is an interfacial enzyme that has higher catalytic ability when bound to the membrane surface [96], and it hydrolyzes PIP3 on a lipid membrane in the hopping mode [97] [98]. In addition to the substrate, the membrane binding of PTEN involves (at least) two additional lipid types. The C2 domain of PTEN interacts with negatively charged lipids, such as phosphatidylserine [99], and it facilitates membrane binding electrostatically through a hopping type interaction [98]. Furthermore, PTEN possesses an N-terminal phosphatidylinositol-4,5-bisphosphate PIP2 binding domain. This third interaction likely gives rise to two different mechanisms by which the catalytic activity of PTEN is modulated through enzymatic product formation. The first mechanism involves an increase in membrane binding affinity through product formation [97]. The second one involves a conformational change of the enzyme after PIP2 binding that causes allosteric activation [86, 100]. To what extent these two mechanisms contribute to the overall autocatalytic kinetics of PTEN catalyzed PIP3 conversion is currently unknown. To clarify this matter is one of the main objectives of this chapter. Characterizing how the rate of PIP3 dephosphorylation by PTEN is regulated by PH domain-containing proteins is an additional aim of this section.

Several previous studies have analyzed the enzyme kinetics of PTEN. Initial studies assessed the hydrolysis of the highly soluble inositol 1,3,4,5-tetrakisphosphate substrate

[7] Parts of this chapter are reproduced by previously published work: Liu, C.; Deb, S.; Ferreira, V. S.; Xu, E.; Baumgart, T., Kinetics of PTEN-mediated PIP3 hydrolysis on solid supported membranes. *PLoS One* **2018,** *13* (2).

based on a radioactivity assay [101]. The malachite green assay [102] can be used for both soluble substrates [103] and those embedded in lipid membranes [102]. A method based on a soluble fluorescent substrate has also been developed [104]. While the assessment of PTEN activity by means of soluble substrates is at times efficient and straightforward, it has been appreciated for a long time that the activity of interfacial enzymes, including PTEN can be substantially affected by the interface [105, 106]. Accordingly, several previous contributions have studied PTEN catalysis by means of phosphoinositide lipids contained in vesicles [97, 107]. One challenge of working with a dispersion of vesicles containing mixed lipids is compositional variation from vesicle to vesicle [108].

This problem can be solved by working with single lipid bilayer membranes deposited onto a solid support [109]. Solid supported membranes, in either solely physisorbed [110] or partially tethered form [111], have previously been used to study the membrane binding behavior of PTEN. This approach allows the application of surface sensitive techniques, including surface plasmon resonance spectroscopy [111] and total internal reflection microscopy imaging [112]. The application of optical imaging to study PTEN action may ultimately allow the study of spatio-temporal dynamics of reconstituted versions of the PI3K / PTEN reaction pathway [113, 114].

4.1 Experimental Setup for PTEN Kinetics Measurement

In Chap 3.2 we have characterized the reversible binding of YFP-PH-Grp1 on the model membranes in the Ibidi flow chamber (Fig 4.1), we proceeded to study PIP3

hydrolysis by PTEN, under the condition of continuous flow of 1 cm/s. All of the lipid bilayers used in this study consisted of a DOPC background, and also contained 5% DOPS, which increases PTEN binding [86], and small amounts of phosphoinositide lipids, as well as the lipid fluorophore TR-DHPE (Texas-Red-dihexadecanoylphosphatidylethanolamine).

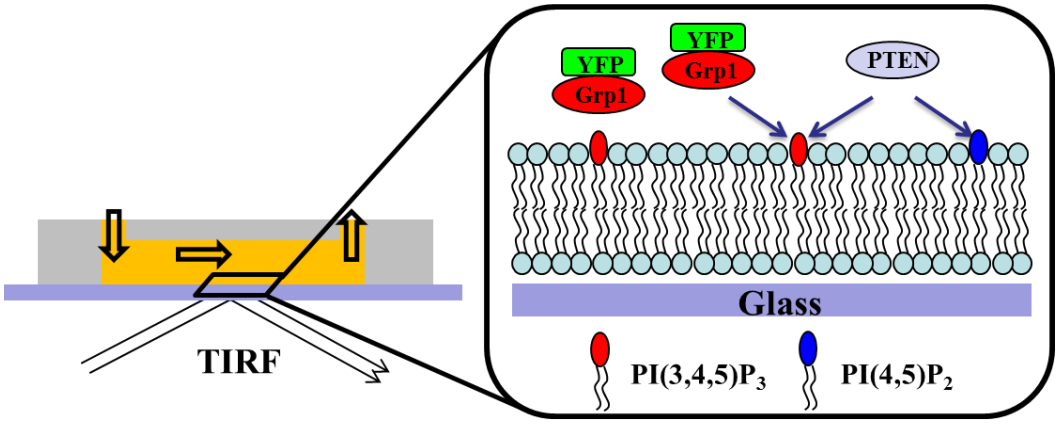

Fig 4.1 Interfacial protein binding and enzyme catalysis on supported lipid bilayer in flow chamber. Schematic illustration of the flow chamber / TIRF detection system. Small unilamellar vesicles (SUV) are injected to form a supported lipid bilayer on the glass surface. Subsequently, YFP-PH-Grp1 and PTEN / YFP-PH-Grp1 are injected sequentially into the measurement chamber, and the YFP-PH-Grp1 signal change on the membrane is monitored by TIRF microscopy imaging.

4.2 Autocatalytic PIP3 Hydrolysis by PTEN through Membrane-Recruitment and Allosteric Activation Mechanisms

When PTEN is introduced into the measurement chamber, accessible PIP3 will be hydrolyzed and thus YFP-PH-Grp1 will progressively dissociate from the membrane. This process was imaged through TIRF via the YFP-PH-Grp1 signal decay. We found that the YFP-PH-Grp1 signal decay upon PTEN injection does not follow simple exponential decay in the presence of non-zero initial concentrations of PIP2. Instead, sigmoidal kinetics was observed for membranes initially containing 0.2% PIP2 (Fig 4.2). The sigmoidally shaped kinetics curve is interesting because it is consistent with the fact that PIP3 hydrolysis by PTEN is an autocatalytic reaction. This finding supports the notion that PIP2 produced through PTEN action has positive effects on either PTEN recruitment or PTEN activation, or both.

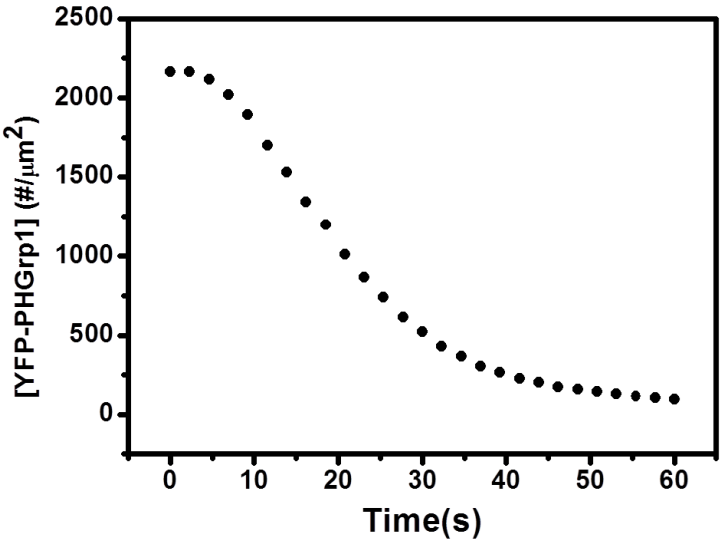

Fig 4.2 PIP3 hydrolysis kinetics by PTEN on 0.2% PIP3 / 0.2% PIP2 / 5% DOPS / 94.4 % DOPC / 0.2% TR-DHPE membrane. The y-axis represents the surface concentration of YFP-PH-Grp1. The kinetic curve of YFP-PH-Grp1 decay follows a sigmoidal shape.

On the basis of the positive effect of PIP2 on PTEN hydrolysis of PIP3, we sought kinetic models capable of suitably describing this autocatalytic reaction (Fig 4.3). In our model, we consider the reversible binding of YFP-PH-Grp1 to PIP3. We assume that PIP3 cannot be hydrolyzed by PTEN while bound to Grp1, as both the catalytic site of PTEN and the PH domain of Grp1 bind to the inositol ring of PIP3 [17, 115]. The phosphoinositide sensor YFP-PH-Grp1 therefore does not merely act as a reporter for PIP3 hydrolysis, but also competes with PTEN in binding to PIP3. When YFP-PH-Grp1 dissociates from PIP3, PTEN can bind to and dephosphorylate PIP3 to yield PIP2. The newly formed PIP2 can recruit more PTEN (via its PIP2 binding domain) to the membrane, which accelerates the PIP3 hydrolysis due to PTEN enrichment on the membrane. Furthermore, PTEN can be allosterically activated when bound to PIP2, which increases its phosphatase activity toward PIP3. In our model, we assume that PIP3 can be hydrolyzed by both membrane-bound PTEN devoid of PIP2 (PTEN) and by PIP2-bound PTEN (PTEN-PIP2). To account for PIP2 binding leading to allosteric activation of PTEN and thereby increasing its phosphatase activity, we defined an effective catalysis rate with the help of the Hill equation [116, 117] (Eq. 6). The reaction equilibria are listed below.

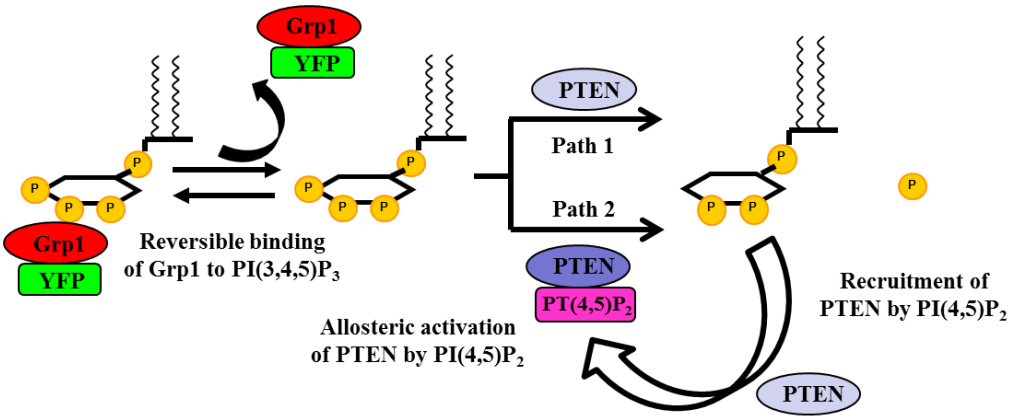

Fig 4.3 Theoretical model for PTEN kinetics. YFP-PH-Grp1 binds PIP3 competitively with PTEN, which can only bind to and hydrolyze PIP3 when Grp1 is not bound. We assume that free PIP3 can be hydrolyzed via two paths, either by PIP2-free PTEN (path 1, PTEN) or by PIP2-bound PTEN (path 2, PTEN-PIP2). When bound to PIP2, PTEN can be allosterically activated and increases its hydrolysis activity towards PIP3. Newly formed PIP2 can also recruit more PTEN from solution to the membrane.

$$Grp1_{comp\_sol} + [PIP3] \underset{k_d^{Grp1}}{\overset{k_a^{Grp1}}{\rightleftharpoons}} [Grp1 - PIP3] \tag{4.1}$$

$$PTEN_{comp\_sol} \underset{k_d^{PTEN}}{\overset{k_a^{PTEN}}{\rightleftharpoons}} PTEN_m \tag{4.2}$$

$$PTEN_{comp\_sol} + [PIP2]_m \underset{k_d^{PTEN-PIP2}}{\overset{k_a^{PTEN-PIP2}}{\rightleftharpoons}} [PTEN - PIP2]_m \tag{4.3}$$

$$PTEN_m + [PIP3]_m \xrightarrow{k_{cat}^{PTEN}} PTEN_m + [PIP2]_m \tag{4.4}$$

$$[PTEN - PIP2]_m + [PIP3]_m \xrightarrow{k_{cat}^{PTEN-PIP2}} [PTEN - PIP2]_m + [PIP2]_m \tag{4.5}$$

Reaction 4.1 describes the reversible binding of YFP-PH-Grp1 to PIP3. PIP2-independent and PIP2-dependent association of solution PTEN to the membrane are described by reactions 4.2 and 4.3, respectively. Two routes of PIP3 hydrolysis are then considered. In one way, PIP3 is hydrolyzed by PIP2-free PTEN, described by reaction 4.4. In the second way, PIP3 is hydrolyzed by PIP2-bound PTEN, described by reaction 4.5.

To further evaluate the autocatalytic nature PIP3 hydrolysis by PTEN, we varied the concentration of PIP2 within DOPS / DOPC mixtures and studied how the surface concentration YFP-PH-Grp1 changes with time after PTEN injection (Fig 4.4). Clearly, the PIP3 hydrolysis rate increases with increasing initial PIP2 content in the membrane.

In addition, we evaluated the effect of YFP-PH-Grp1 on PIP3 hydrolysis by varying the bulk concentration of YFP-PH-Grp1 systematically (Fig 4.5A). The PIP3 hydrolysis rate is observed to decrease with increasing YFP-PH-Grp1 bulk concentration (Fig 4.5B). The slower kinetics at high concentration of YFP-PH-Grp1 can be rationalized by the fact that competitive binding of Grp1 to PIP3 reduces the probability of PTEN accessing its substrate.

The global fitting result of PIP3 hydrolysis by PTEN at different surface concentrations of PIP2 and different YFP-PH-Grp1 bulk concentrations is shown as grey lines in Figs 4.4 and 4.5. The corresponding fitting parameters are listed in Table 4.1.

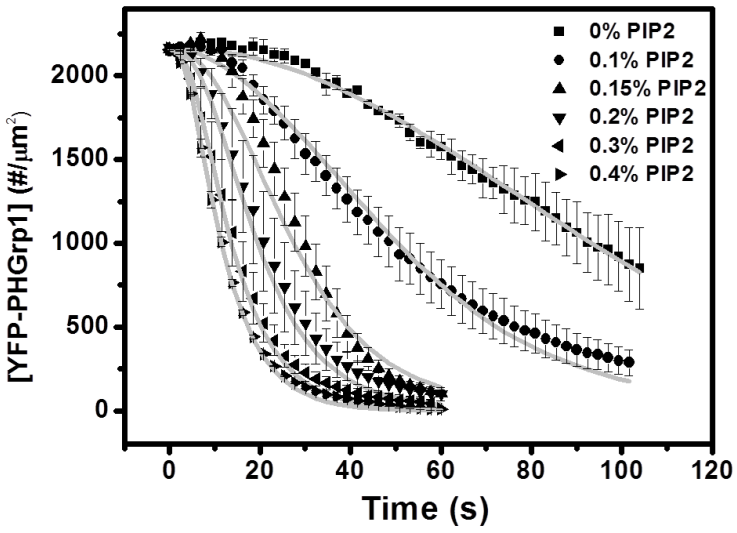

Fig 4.4 PIP3 hydrolysis kinetics by PTEN at DOPC / DOPS membrane with different % of PIP2. The membrane composition: 0.2% PIP3 + 5% DOPS + *n*% PIP2 + (94.6-*n*)% DOPC + 0.2% TR-DHPE. *n*=0 (square), *n*=0.1 (circle), *n*=0.15 (triangle), *n*=0.2 (down-pointing triangle), *n*=0.3 (left-pointing triangle), *n*=0.4 (right-pointing triangle). The y-axis represents the surface concentration of YFP-PH-Grp1. The bulk concentration of YFP-PH-Grp1 is 300 nM and the bulk concentration of PTEN is 100 nM. The global fitting curves based on our kinetic PTEN catalysis model (Fig 4.4, Eqs.1.13-1.14, 4.1 – 4.5) are shown as a grey solid line. The rate of YFP-PH-Grp1 signal decay and thus PTEN action increases with initial PIP2 surface concentration. Data points are mean ± SEM (typically $N \geqq 3$, but always $N \geqq 2$ measurements).

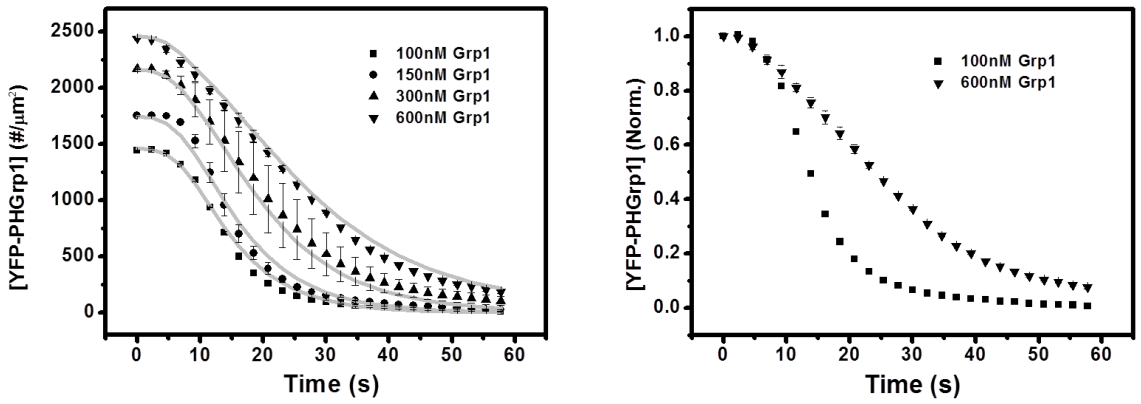

Fig 4.5 Kinetics of PIP3 hydrolysis by PTEN at different concentrations of YFP-PH-Grp1.

(A) The membrane composition is 0.2% PIP3 + 5% DOPS + 0.2% PIP2 + 94.4% DOPC + 0.2% TR-DHPE and the bulk concentration of YFP-PH-Grp1 is 100 nM (square), 150 nM (circle), 300 nM (triangle), and 600 nM (down-pointing triangle), respectively. The bulk concentration of PTEN is 100 nM. The grey solid lines are the global fitting results based on our kinetic PTEN catalysis model (Fig 4.4, Eqs. 1.13-1.14, 4.1 – 4.5). Data points are mean ± SEM (typically $N \geqq 3$, but always $N \geqq 2$ measurements).

(B) Normalized kinetic traces of PIP3 hydrolysis by PTEN at 100 nM (square) and 600 nM (down-pointing triangle) of YFP-PH-Grp1. The rate of YFP-PH-Grp1 signal decay upon PTEN injection increases with decreasing bulk YFP-PH-Grp1 concentration, which agrees with the model that YFP-PH-Grp1 competitively binds to PIP3 with PTEN.

Table 4.1. Value of fitting parameters obtained for fits to data shown in Figs 4.4, and 4.5A.

	Parameters	Values	Literature value
k_{cat}^{PTEN}	Dephosphorylation rate of PIP3 by PTEN	11±1 s^{-1}	15 s^{-1} (ref [118]) ; 0.5 s^{-1} (ref [119])
k_{a}^{PTEN}	Association rate of PTEN to lipid bilayer	(1.7±0.3)*10^{-3} m/s ; 0.71 μM^{-1} s^{-1}*	0.5 μM^{-1} s^{-1} (ref [120])
k_{d}^{PTEN}	Dissociation rate of PTEN from lipid bilayer	0.7±0.1 s^{-1}	1 s^{-1} (ref [118]) ; 3-7.7 s^{-1} (ref [112])
$k_{a}^{PTEN-PIP2}$	Association rate of PTEN to PIP2	200±22 μM^{-1} s^{-1}	50 μM^{-1} s^{-1} (ref [119], assumed)
$k_{d}^{PTEN-PIP2}$	Dissociation rate of PTEN from PIP2	0.30±0.05 s^{-1}	1 s^{-1} (ref [118]) ; 0.1 s^{-1} (ref [119], assumed)
$k_{cat}^{PTEN-PIP2}$	Dephosphorylation rate of PIP3 by PTEN-PIP2	19±2 s^{-1}	

K_M^{PTEN}	**Michaelis constant of PTEN dephosphorylation reaction**	**$(2.0\pm0.3)*10^{-3}$ μMm**	
$K_M^{PTEN\text{-}PIP2}$	**Michaelis constant of PTEN-PIP2 dephosphorylation reaction**	**$(2.3\pm0.2)*10^{-5}$ μMm**	**See Chapter 4.6 (ref [121])**
$K_{PTEN,PIP2}$		**$(7.9\pm0.2)*10^{-6}$ μMm**	
n	**Hill coefficient**	**2.0±0.1**	

*** Unit conversion for parameter comparison will be discussed in Chapter 4.6.**

The uncertainty of the fit parameters is the standard error.

4.3 Two Reaction Paths of PIP3 Hydrolysis by PTEN

Based on our model, PIP3 can be hydrolyzed by two different forms of PTEN: PIP2-free PTEN (path 1, PTEN) and PIP2-bound PTEN (path 2, PTEN-PIP2, shown in Fig 4.3). The next question we would like to answer is which path contributes more to PIP3 hydrolysis. We determined the ratio of PIP3 hydrolysis contributed by PTEN and

PTEN-PIP2 at different initial surface concentrations of PIP2 (Fig 4.6). By incorporating fitting parameters (Table 4.1) into our PTEN model, we found that the ratio of the number of PIP3 molecules hydrolyzed by PTEN-PIP2 to those hydrolyzed by PTEN increases with greater initial % of PIP2. In other words, which reaction path dominates PIP3 hydrolysis is determined by the initial PIP2 concentration of the membrane. When there was no initial PIP2 in the bilayer, path 1 was dominant in PIP3 hydrolysis. Path 2 became comparable to path 1 at initial 0.1% PIP2, and became dominant when the initial PIP2 increased to 0.15%. The routes of PIP3 hydrolysis switched from path 1 to path 2 when initial PIP2 surface concentration was increased from 0% to 0.15%.

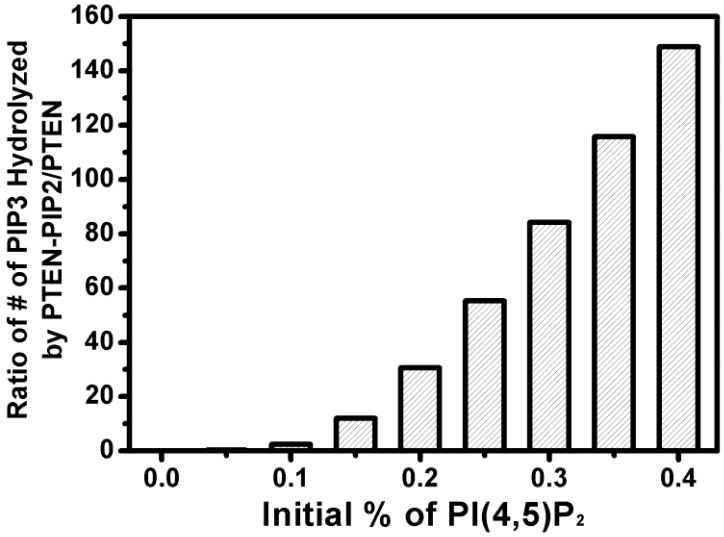

Fig 4.6 Simulation of PIP3 hydrolysis by PTEN-PIP2 and PTEN. Based on the theoretical model we proposed (Fig 4.3) and the fitting parameters it yielded (Table 4.1), we examined how the ratio of the number of PIP3 molecules hydrolyzed by PTEN-PIP2 versus PTEN increased with rising PIP2 concentration in the supported lipid bilayer.

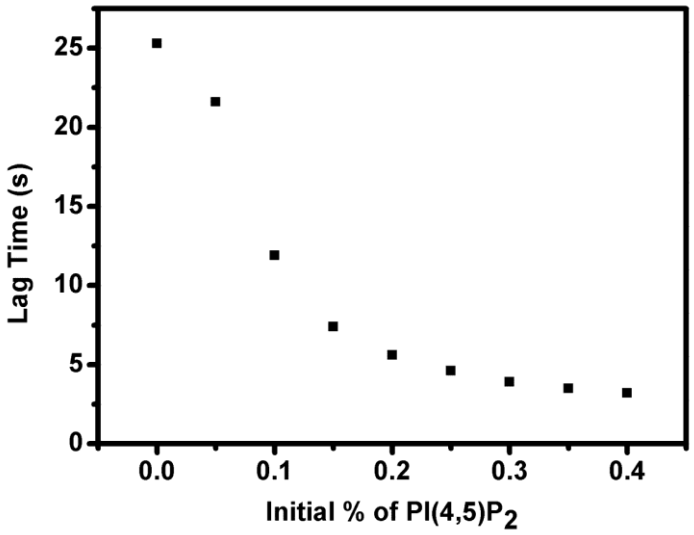

Fig 4.7 Simulation of change of lag time of PIP3 hydrolysis with initial % of PIP2. Based on the theoretical model we proposed (Fig 4.3) and the fitting parameters it yielded (Table 4.1), we predicted the lag time for YFP-PH-Grp1 signal decay after PTEN injection. We defined the lag time as the time needed for the YFP-PH-Grp1 signal to decay to 95% of its initial value. Clearly, the lag time shortens with increasing initial PIP2 % on the membrane.

4.4 Test of Minimal Kinetic Model for PTEN-PIP2 Autocatalytic Reaction

To answer the question whether the model we proposed can be viewed as a minimum kinetic model describing PIP3 hydrolysis by PTEN, we tested two simplified models: 1) a model assuming PIP2 induced recruitment of PTEN only, and 2) a model assuming PIP2 mediated allosteric activation of PTEN only. In the "recruitment only" model, PTEN and PTEN-PIP2 are assumed to have the same turnover number k_{cat} and

interfacial Michaelis-Menten constant K_M of PIP3. In other words, PIP2 affects membrane binding, but does not affect catalytic properties of PTEN at the molecular level. Therefore, the Hill equation was not included in this model. In the "allosteric activation only" model, PIP2 is assumed to be unable to promote PTEN membrane binding, but able to allosterically activate PTEN. We fitted PIP3 hydrolysis kinetics curves for different PIP2 surface concentrations as well as different YFP-PH-Grp1 bulk concentrations simultaneously with both models (Fig 4.8). From the fitting results we noticed that though the individual "recruitment only" model and "allosteric activation only" model fit some curves well, it can't globally fit all curves. Some fitting curves deviate dramatically from the kinetic curves. The results clearly demonstrate that neither one of these two models are sufficient to fit the data, strongly suggesting that the positive effect of PIP2 on PTEN hydrolysis of PIP3 results from a combination of both recruitment and allosteric activation effect.

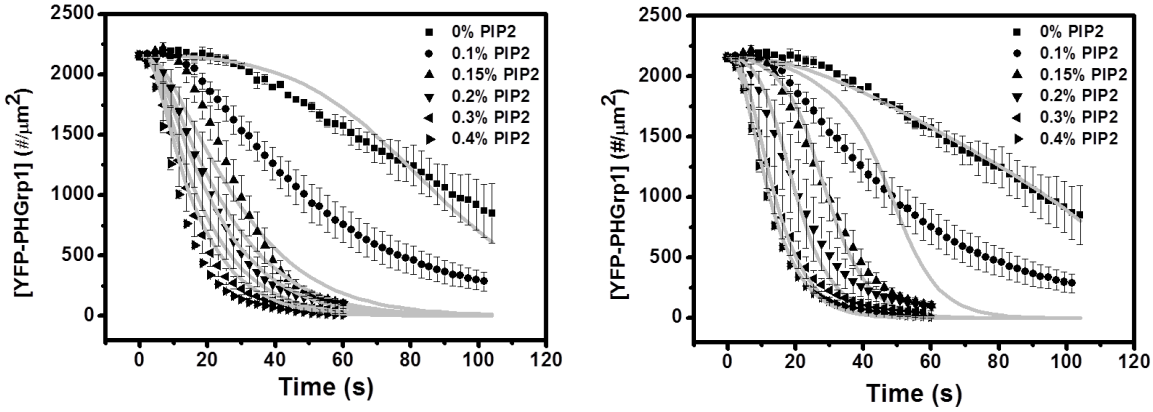

Fig 4.8 PIP3 hydrolysis kinetics by PTEN at DOPC / DOPS membrane with different % of PIP2. The membrane composition: 0.2% PIP3 + 5% DOPS + *n*% PIP2 + (94.6-*n*)% DOPC + 0.2% TR-DHPE. *n*=0 (square), *n*=0.1 (circle), *n*=0.15 (triangle),

n=0.2 (down-pointing triangle), *n*=0.3 (left-pointing triangle), *n*=0.4 (right-pointing triangle). Data points are mean ± SEM (typically $N \geqq 3$, but always $N \geqq 2$ measurements).

(A) Fit it with recruitment only model (Eqs. 4.6 – 4.10, 4.15, 4.16)

(B) Fit it with allosteric activation only model (Eqs. 4.6 – 4.9, 4.13, 4.14)

4.5 Summary of Differential Equations of PTEN Model

4.5.1 Association & Dissociation Reactions

$$\frac{\partial[Grp1-PIP3]}{\partial t} = k_a^{Grp1}[Grp1]_{comp\_sol}[PIP3]_m - k_d^{Grp1}[Grp1-PIP3]_m \tag{4.6}$$

$$\frac{\partial[Grp1]_{comp\_sol}}{\partial t} = \frac{1}{h}\{k_{tr}(Grp1_{B\_sol} - Grp1_{comp\_sol}) + k_d^{Grp1}[Grp1-PIP3]_m$$

$$-k_a^{Grp1}[Grp1]_{comp\_sol}[PIP3]_m\} \tag{4.7}$$

$$\frac{\partial[PTEN]_m}{\partial t} = k_a^{PTEN}[PTEN]_{comp\_sol} - k_d^{PTEN}[PTEN]_m \tag{4.8}$$

$$\frac{\partial[PTEN]_{comp\_sol}}{\partial t} = \frac{1}{h}\{k_{tr}(PTEN_{B\_sol} - PTEN_{comp\_sol}) - k_a^{PTEN}[PTEN]_{comp\_sol} + k_d^{PTEN}[PTEN]_m\} \tag{4.9}$$

$$\frac{\partial[PTEN-PIP2]_m}{\partial t} = k_a^{PTEN-PIP2}[PTEN]_{comp\_sol}[PIP2]_m - k_d^{PTEN-PIP2}[PTEN-PIP2]_m \tag{4.10}$$

4.5.2 Enzyme Dephosphorylation Reactions

$$\frac{\partial [PIP3]_m}{dt} = -k_{cat}^{PTEN}[PTEN]_m\left(\frac{[PIP3]_m}{K_M^{PTEN}+[PIP3]_m}\right) - k_{cat}^{eff}[PTEN-PIP2]_m\left(\frac{[PIP3]_m}{K_M^{PTEN-PIP2}+[PIP3]_m}\right)$$

$$+k_d^{Grp1}[Grp1-PIP3]_m - k_a^{Grp1}[Grp1]_{comp\_sol}[PIP3]_m \tag{4.11}$$

$$\frac{\partial [PIP2]_m}{dt} = k_{cat}^{PTEN}[PTEN]_m\left(\frac{[PIP3]_m}{K_M^{PTEN}+[PIP3]_m}\right) + k_{cat}^{eff}[PTEN-PIP2]_m\left(\frac{[PIP3]_m}{K_M^{PTEN-PIP2}+[PIP3]_m}\right)$$

$$-k_a^{PTEN-PIP2}[PTEN]_{comp\_sol}[PIP2]_m + k_d^{PTEN-PIP2}[PTEN-PIP2]_m \tag{4.12}$$

Where $k_{cat}^{eff} = k_{cat}^{PTEN-PIP2}\{\frac{[PIP2]_m^n}{(K_{PTEN,PIP2})^n+[PIP2]_m^n}\}$

Meaning of subscript:

a. m: protein or lipids are on the membrane

b. comp_sol: protein in the inner compartment of chamber

c. B_sol: protein in the bulk solution

4.5.3 Allostery Only Model (Eqs. 4.6 – 4.9, 4.13, 4.14)

$$\frac{\partial [PIP3]_m}{dt} = -k_{cat}^{PTEN}[PTEN]_m\left(\frac{[PIP3]_m}{K_M^{PTEN}+[PIP3]_m}\right) - k_{cat}^{eff}[PTEN]_m\left(\frac{[PIP3]_m}{K_M^{PTEN-PIP2}+[PIP3]_m}\right)$$

$$+k_d^{Grp1}[Grp1-PIP3]_m - k_a^{Grp1}[Grp1]_{comp\_sol}[PIP3]_m \tag{4.13}$$

$$\frac{\partial [PIP2]_m}{dt} = k_{cat}^{PTEN}[PTEN]_m\left(\frac{[PIP3]_m}{K_M^{PTEN}+[PIP3]_m}\right) + k_{cat}^{eff}[PTEN]_m\left(\frac{[PIP3]_m}{K_M^{PTEN-PIP2}+[PIP3]_m}\right) \tag{4.14}$$

4.5.4 Recruitment Only Model (Eqs. 4.6 – 4.10, 4.15, 4.16)

$$\frac{\partial[PIP3]_m}{dt} = -k_{cat}^{PTEN}([PTEN]_m + [PTEN-PIP2]_m)(\frac{[PIP3]_m}{K_M^{PTEN} + [PIP3]_m})$$

$$+k_d^{Grp1}[Grp1-PIP3]_m - k_a^{Grp1}[Grp1]_{comp\_sol}[PIP3]_m \quad (4.15)$$

$$\frac{\partial[PIP2]_m}{dt} = k_{cat}^{PTEN}([PTEN]_m + [PTEN-PIP2]_m)(\frac{[PIP3]_m}{K_M^{PTEN} + [PIP3]_m})$$

$$-k_a^{PTEN-PIP2}[PTEN]_{comp\_sol}[PIP2]_m + k_d^{PTEN-PIP2}[PTEN-PIP2]_m \quad (4.16)$$

4.6 Parameters in PTEN Kinetic Model Discussion

4.6.1 Comparison between Association Rate Constant of PTEN and the Literature Value

We obtained an association rate constant of PTEN to the membrane of k_a^{PTEN} = 1.67*10^{-3} m/s. This quantity is an effective adsorption rate constant, which corresponds to the association constant times the lipid concentration. So the association constant can be expressed by the effective adsorption rate constant divided by the lipid surface concentration as follows:

$$k_{on}(s^{-1}\mu M^{-1}) = k_a^{PTEN}(m/s)/[PC+PS](\mu M \cdot m)$$

Our membrane contains 5% DOPS and ~94% DOPC, which corresponds to 1.18*10^{-4} μMm and 2.22*10^{-3} μMm, respectively. With the help of the above formula we

obtained the association constant of k_{on} = 0.71 $\mu M^{-1} s^{-1}$, which is comparable to the literature value of 0.5 $\mu M^{-1} s^{-1}$ [120].

4.6.2 Combination of Hill Equation and Michaelis-Menten Equation

It has been shown that PIP2 can allosterically activate the catalytic activity of PTEN towards PIP3. To quantitatively account for this allosteric effect, we divide the PIP3 hydrolysis pathways into two pathways: membrane-bound PTEN unbound to PIP2 on the one hand, and membrane-bound and PIP2-bound PTEN (PTEN-PIP2).

According to a Campbell et al. study [100], the dose-dependent activation of PTEN towards PI(3,4)P2 (or PIP3) substrate in solution can be expressed as

$$V = \frac{V_{act}[PI(4,5)P2]}{K_{act} + [PI(4,5)P2]} \tag{4.17}$$

where V is the initial rate of PI(3,4)P2 (or PIP3) hydrolysis by PTEN. The rate V_{act} of PI(3,4)P2 hydrolysis by PTEN can also described by Michaelis-Menten kinetics as a function of PI(3,4)P2 (substrate). So V_{act} should be written as:

$$V_{act} = \frac{k_{act}[PTEN][PI(3,4)P2]}{K_M + [PI(3,4)P2]} \tag{4.18}$$

Combining Eq. 4.17 and 4.18, one obtains

$$V = \left(\frac{k_{act}[PTEN][PI(3,4)P2]}{K_M + [PI(3,4)P2]}\right)\left(\frac{[PI(4,5)P2]}{K_{act} + [PI(4,5)P2]}\right) \tag{4.19}$$

Equivalently, in our theoretical model, the rate of PIP3 hydrolysis by PTEN-PIP2 is assumed to follow:

$$k_{cat}^{eff}[PTEN-PI(4,5)P2]_m\{\frac{[PI(3,4,5)P3]_m}{K_M^{PTEN-PI(4,5)P2}+[PI(3,4,5)P3]_m}\} \tag{4.20}$$

where $k_{cat}^{eff}=k_{cat}^{PTEN-PI(4,5)P2}\{\frac{[PI(4,5)P2]_m{}^n}{(K_{PTEN,PI(4,5)P2})^n+[PI(4,5)P2]_m{}^n}\}$ (4.21)

Eqs. 4.18 and 4.20 have similar form except that we use the more general form of the Hill equation to describe the activation of PTEN by PIP2 on the membrane [116].

In summary, the rate of PIP3 hydrolysis by PTEN-PIP2 in our model is assumed to follow Michaelis-Menten kinetics, but the turnover number k_{cat} is PIP2-dependent.

4.7 Summary

In this chapter, we further described PTEN-mediated PIP3 hydrolysis on glass-supported lipid bilayers in the flow chamber. The hydrolysis rate of PIP3 increases with increasing initial PIP2 concentration, suggesting that product-mediated positive feedback occurs in this reaction. By fitting kinetic traces with the proposed theoretical model, we not only extracted a plethora of binding and catalytic parameters, but also identified mechanisms underlying the positive feedback loop. One mechanism is PIP2's recruitment of PTEN from the solution to the membrane, and the other is the PIP2-mediated allosteric activation of PTEN.

CHAPTER 5. Kinetics of PI3K-mediated PIP2 Phosphorylation on Solid Supported Lipid Bilayer[8]

In previous chapters, we classified the binding specificity and affinity of sensor proteins to phosphoinositides, as well as the dephosphorylation of PIP3 by PTEN on model lipid membranes (backward reaction of the PIP2-PIP3 phosphorylation-dephosphorylation cycle). we identified that PTEN-mediated PIP3 hydrolysis involved a positive feedback loop and uncovered mechanisms underlying this feedback. In this chapter, we will characterize the other half of phosphorylation-dephosphorylation cycle: the phosphorylation of PIP2 by PI3K. This contribution is organized as follows: effect of phosphopeptide on PI3K activation was first characterized, next we studied how the rate of PIP2 phosphorylation changes with different substrate and sensor protein concentrations, and finally, we characterized PI3K reaction in PDMS channel.

5.1 Effect of Phosphopeptide on PI3K Activation

To study PIP2 phosphorylation by PI3K, we used the planar bilayer in the Ibidi flow chamber as a platform, as described in the Chap 3. The production of PIP3 in the membrane after a PI3K pulse was introduced in the flow chamber was monitored by YFP-PH-Grp1 (Fig 5.1).

[8] Parts of this chapter are reproduced by currently submitted work: Liu, C.; Zimmerman, Z. E.; Grasso, M.; Gosh, A.; Marmorstein, R.; Radhakrishnan, R.; Baumgart, T., Bistable reaction behavior in PTEN / PI3K mediated phosphoinositide lipid conversion.

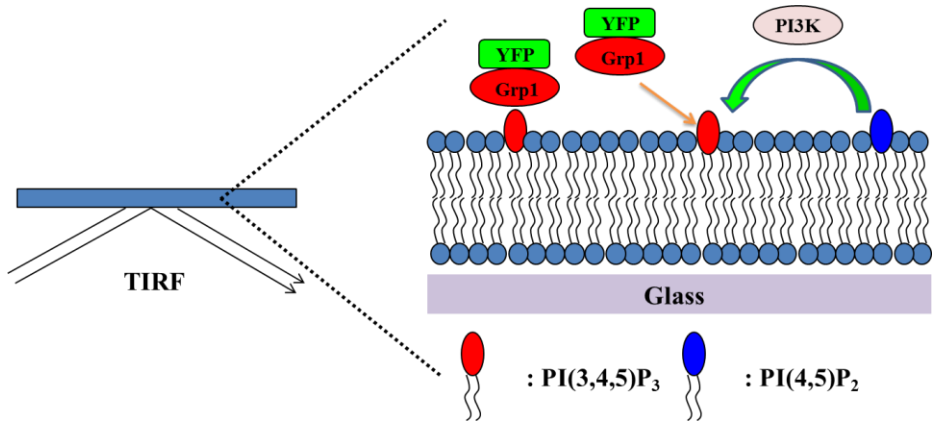

Fig 5.1 Schematic illustration of PIP2 phosphorylation by PI3K on a supported lipid bilayer in the flow chamber. Small unilamellar vesicles (SUV) are injected to form a supported lipid bilayer on the glass surface. Subsequently, YFP-PH-Grp1 and PI3K / YFP-PH-Grp1 are injected sequentially into the measurement chamber, and the YFP-PH-Grp1 signal change on the membrane is monitored by TIRF microscopy imaging.

Phosphopeptide (pY2) has been shown to bind to the p85 N-terminal SH2 domain [87], leading to abrogation of inhibition of the p110 catalytic domain of PI3K. This does not only occur in inhibition release, the phosphopeptide also increases PI3K binding to the membrane in vitro [122]. Therefore, we first characterized the effect of pY2 on PI3K activation on my model membrane system. PIP3 synthesis kinetics was monitored with the rise of YFP-PH-Grp1 on the membrane after a PI3K pulse was injected in the presence or absence of pY2 (Fig 5.2). In the presence of pY2, the signal of Grp1 on the membrane was not only higher in the plateau value, but also took less time to reach a plateau than the sample without pY2. The synthesized pY2 was therefore confirmed to increase PI3K activity on our model membrane, consistent with previous result. The PI3K-mediated PIP2 kinetics in the following sections are all done in the presence of pY2.

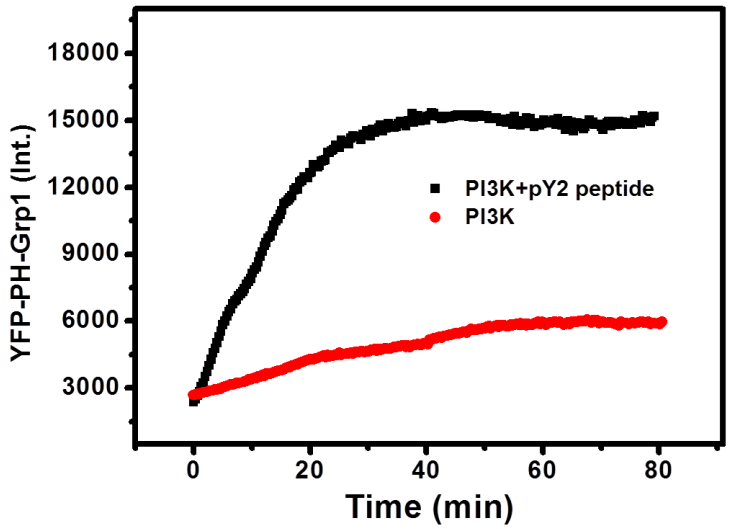

Fig 5.2 PI3K-mediated PIP2 phosphorylation with and without phosphopeptide pY2 in Ibidi chamber. The lipid composition is 1% PIP2 / 5% DOPS / 93.8% POPC / 0.2% DiI. The bulk concentrations of YFP-PH-Grp1, PI3K are 300 nM and 215 nM, respectively. For the sample with the phosphopeptide (pY2), the bulk concentration of pY2 is 25 μM.

5.2 Kinetics of PI3K-Mediated PIP2 Phosphorylation

Having confirmed the validity of using the sensor protein YFP-PH-Grp1 to monitor PIP3 synthesis as well as using pY2 to activate PI3K, we proceeded to characterize PI3K kinetics on the lipid membrane with different percentages of PIP2 content (Fig 5.3). The reaction follows Michaelis-Menten type kinetics, in which the rate of PIP3 synthesis increases with initial PIP2 content in membrane, and reaches a plateau when the PIP2 content is higher than 1% of total phospholipids. The Michaelis-Menten constant (K_m) is 1.06 ± 0.74 % (lipid mole fraction in membrane) of PIP2, which is on the same order of magnitude as the K_m obtained from the Barnett et al. result of recombinant human PI3K on PI / DMPM vesicles (K_m = 6 mole %) [123].

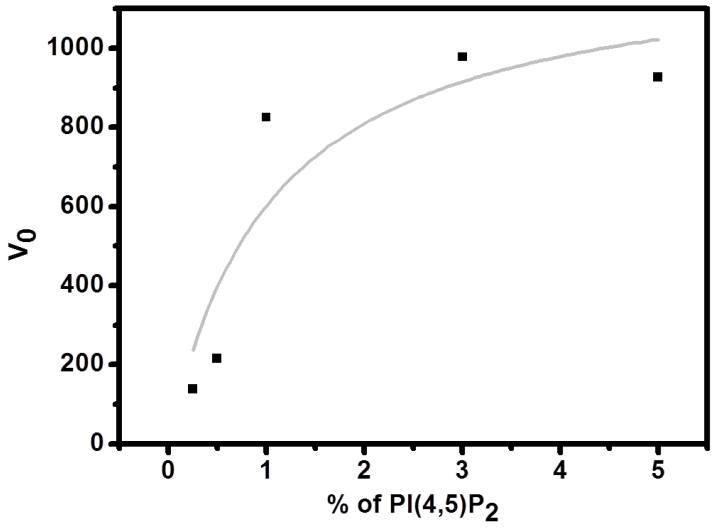

Fig 5.3 PIP2 phosphorylation kinetics by PI3K at a DOPC / DOPS membrane with different percentages of PIP2 content. The lipid composition is *n*% PIP2 / 5% DOPS / POPC / 0.2% DiI. *n* = 0.25, 0.5, 1, 3, 5. The y-axis represents the initial velocity of PIP2 phosphorylation. The bulk concentrations of YFP-PH-Grp1, PI3K, pY2 are 300 nM and 215 nM, and 25μM, respectively. The data was fitted with the Michaelis-Menten equation to yield K_m = 1.06 ± 0.74 % PIP2.

The presence of a sensor, however, might affect the observed interfacial enzyme catalysis, as we observed in the PTEN-mediated PIP3 dephosphorylation (Fig 4.5). To evaluate the effect of sensor proteins on the PI3K-mediated PIP2 phosphorylation kinetics, we monitored the rate of PIP3 synthesis at various bulk concentrations of Grp1 with the amount of PI3K fixed (Fig 5.4). There was no significant effect of bulk Grp1 concentration on PIP3 synthesis kinetics observed. This result could be rationalized by the fact that the sensor protein here is used to monitor product synthesis rather than substrate consumption in the PTEN-mediated reaction, so there is no competitive binding of substrate between the enzyme and sensor protein. In addition, the lack of an observed effect of sensor concentration on PI3K-mediated PIP2 phosphorylation suggests that

there is no product-related feedback loop that exists, further supporting the notion of a Michaelis-Menten type reaction.

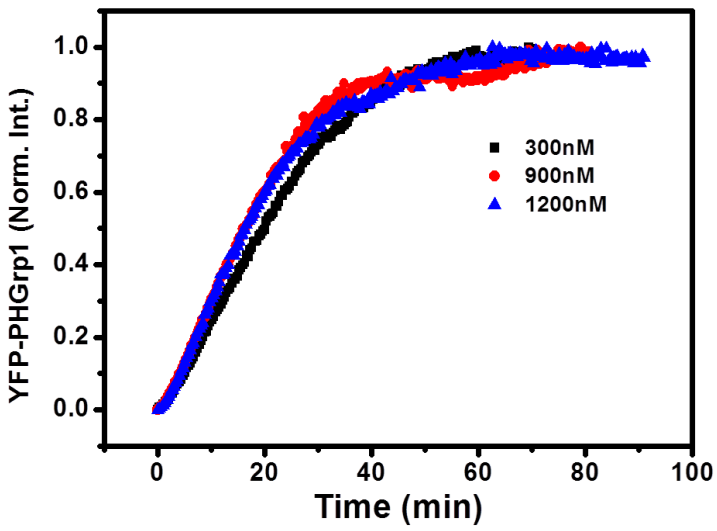

Fig 5.4 Kinetics of PIP2 phosphorylation by PI3K at different bulk concentrations of YFP-PH-Grp1. The lipid composition is 0.75% PIP2 / 5% DOPS / 94.05% POPC / 0.2% DiI. The bulk concentrations of PI3K and pY2 are 215 nM and 25 μM, respectively.

5.3 Characterizing PI3K-Mediated PIP2 Phosphorylation and Sensor Depletion in the PDMS Channel

Although the Ibidi chamber is commercially available and convenient to use, it uses up a large volume of a given sample for the experiment (about 100 μL of sample is needed to fill the chamber). In addition, the glass slide needs to be attached to the Ibidi chamber by double-sided tape, which has a chance of either the sample leaking or the glass cracking during chamber fabrication. The microfluidic system, which only needs a small volume of sample to fill the channel [124, 125], provides an alternative solution for sample saving. One of the most

commonly used materials for the microchannel is poly(dimethylsiloxane) (PDMS), which consists of repeating $–OSi(CH_3)_2–$ units and has the advantage of low cost, impermeability to water, and easy binding to glass without adhesives [126, 127]. Using the PDMS channel, it only takes about 1 μL sample to fill the channel, which saves roughly a hundred times more the sample compared to the Ibidi chamber. Also, PDMS binds glass tightly after an oxygen plasma treatment without using adhesives, so it reduces the risk of sample leakage or glass slide cracking during preparation. The lipid bilayer was prepared on a glass slide in the PDMS chamber as described in Chapter 2.

The bilayer was first equilibrated with YFP-PH-Grp1, and then PI3K was coinjected with Grp1 into the PDMS channel (Fig 5.5). However, we did not observe a significant Grp1 signal increase as observed in the Ibidi chamber. But when fresh Grp1 was pulse injected into the channel, the Grp1 signal on the membrane increased significantly. The signal increased in a stepwise manner after we pulse injected a sensor protein into the chamber.

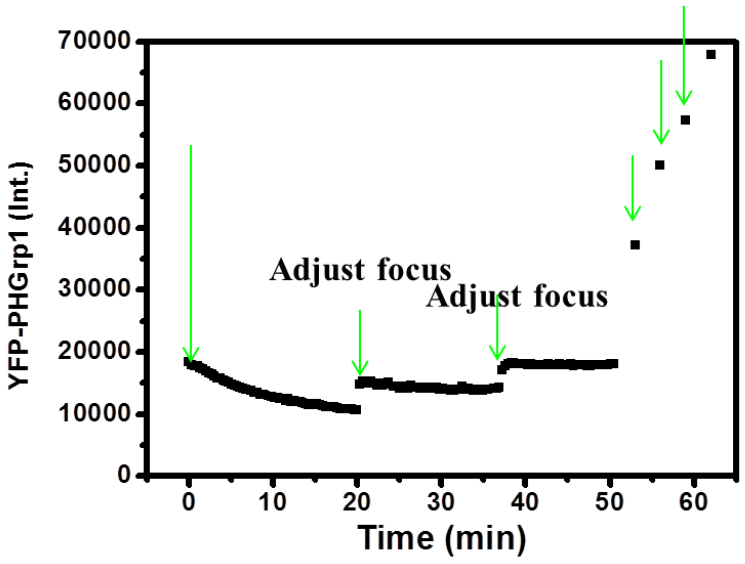

Fig 5.5 PI3K-mediated PIP2 phosphorylation reaction in the PDMS channel. The bilayer composition: 5% PIP2 / 0.5% PIP3 / 15% DOPS / 79.3% POPC / 0.2% DiI. The y-axis represents

the fluorescence intensity of Grp1 on the supported lipid bilayer. The bulk concentrations of YFP-PH-Grp1, PI3K, pY2 are 300 nM and 330 nM, and 25μM, respectively.

We considered two different hypotheses to explain these observations. The first one is that PI3K displaces bound Grp1 from the surface, and the second is that Grp1 is depleted from the solution by the newly generated PIP3 on the membrane. Other potential Grp1 binders, like chamber walls and tubing, are equilibrated with Grp1 prior to PI3K injection.

To test the first hypothesis, we co-injected PI3K with Grp1 but without ATP, which is required for the phosphorylation reaction (Fig 5.6). 40 minutes after the enzyme and sensor injection, fresh Grp1 was injected into the channel, but there was no significant increase of signal compared to the initial value. This result confirms that the rise of Grp1 signal on the membrane depends on the phosphorylation reaction, thus excluding the first hypothesis.

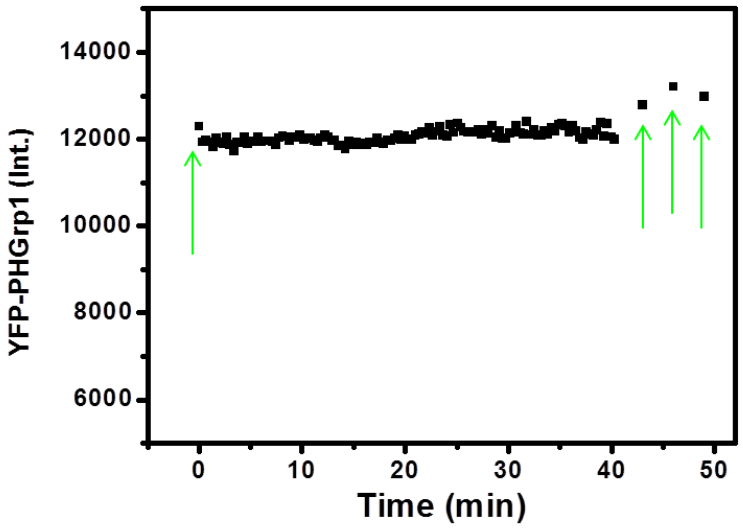

Fig 5.6 PI3K-mediated PIP2 phosphorylation reaction in the absence of ATP. The bilayer composition: 5% PIP2 / 0.5% PIP3 / 15% DOPS / 79.3% POPC / 0.2% DiI. The y-axis represents

the fluorescence intensity of Grp1 on the supported lipid bilayer. The bulk concentrations of YFP-PH-Grp1, PI3K, pY2 are 300 nM and 330 nM, and 25μM, respectively.

Before we demonstrate the results from testing hypothesis 2, it may be worth first discussing why the degree of protein depletion from solution could be higher in a PDMS channel than in an Ibidi chamber. The Lionello et al. simulation shows that at given binding characteristics, the level of protein depletion from solution decreases with increasing volume-to-surface ratio (height) of the chamber [128]. The height of an Ibidi chamber (about 500 μm) is roughly ten times higher than the height of a PDMS chamber (about 40 μm), so we would expect that protein depletion would be more severe in a PDMS chamber.

We tested hypothesis 2 by sequentially loading Grp1 into the PDMS chamber (Fig 5.7). The membrane-bound protein concentration should remain at the same plateau value no matter how many times new proteins are pulse injected if there no depletion occurs [129]. If the plateau value increases when the second pulse of protein is introduced, then it means that there is protein depletion from the solution in the chamber. In our PDMS chamber with supported lipid bilayer, 50 μL of Grp1 was injected and incubated until the signal remained stable on the membrane. Then a second pulse of 50 μL of Grp1 was injected. The Grp1 signal increased significantly, which suggests that the depletion of Grp1 from solution occurs in our PDMS chamber. The signal of Grp1 on the membrane remained stable after the third pulse injection.

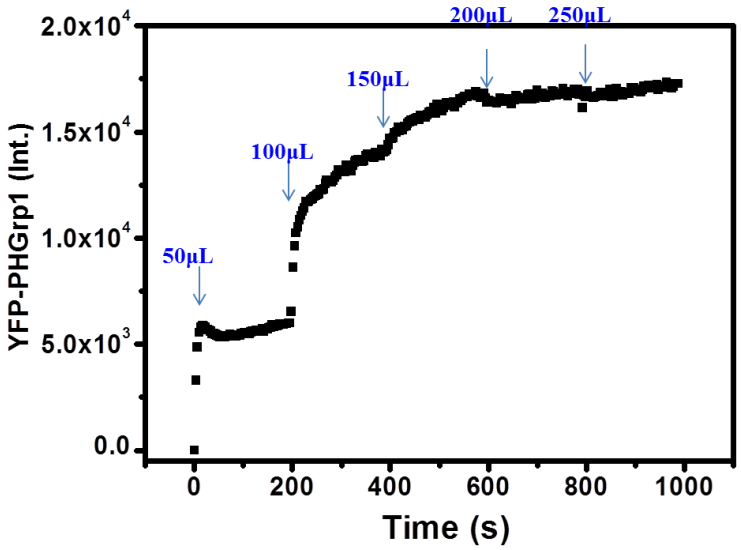

Fig 5.7 Pulse injection of Grp1 into PDMS chamber. The bilayer composition: 5% PIP2 / 0.5% PIP3 / 15% DOPS / 79.3% POPC / 0.2% DiI. The y-axis represents the fluorescence intensity of Grp1 on the supported lipid bilayer. The bulk concentrations of YFP-PH-Grp1, PI3K, pY2 are 300 nM and 330 nM, and 25µM, respectively.

CHAPTER 6. Effect of KRas on PI3K

The Ras GTPases are key regulators in signaling networks that control cell growth and differentiation [130]. They belong to the guanine nucleotide-binding (G) protein family, which are converted between an active GTP-bound state and an inactive GDP-bound state by guanine nucleotide exchange factors (GEFs) and GTPase-activating proteins (GAPs), respectively [131]. GEFs stimulate the exchange of GDP to GTP on Ras, which activates the Ras to bind downstream effectors to trigger signaling processes. The active state of Ras is deactivated when GAPs stimulates Ras to hydrolyze GTP to GDP [130]. Upon receptor tyrosine kinase (RTK) activation, RTKs autophosphorylate, and the phosphorylated tyrosine recruits binding to GRB2, and the GEF SOS, which activates Ras [132]. Two major signaling pathways initiated by activated Ras are: (i). MAPK pathway (Ras activates Raf, which phosphorylates MEK, and activated MEK then phosphorylates MAPK) and (ii). PI3K-Akt pathway (Ras activates PI3K, which phosphorylates PIP2 to form PIP3).

The localization of Ras to various subcellular membrane compartments is regulated by post-translational modifications (PTM) at the C-terminus [133]. There are four different isoforms of Ras: HRas, NRas, KRas4A, and KRas4B. The farnesylation (modified with a farnesyl lipid) at the CAAX-motif (C: cysteine; A: aliphatic amino acid; X: any amino acid) causes Ras to accumulate at the endoplasmic reticulum (ER). The further modification by palmitoylation at the Golgi apparatus causes HRas and NRas to traffic to the plasma membrane. In contrast, KRas4B binds to the cell membrane with

farnesyl group and its polybasic Lys-rich domain upstream of the CAAX-motif [133, 134].

Gain-of-function missense mutations in Ras are found in ~25% of all human cancers, and KRas is the predominantly mutated isoform (85%) [135]. Around 35 – 40% of colorectal cancers occur with single nucleotide point mutations in KRas (mostly in codon 12 or 13), which result in metastatic colorectal cancers that are resistant to anti-EGFR monoclonal antibody treatment [136, 137].

In Chapter 5, PI3K-mediated PIP2 phosphorylation and the effect of pY2 on PI3K activation were discussed. In this Chapter, we will discuss another key activator of PI3K, the GTPase KRas, and characterize the PIP2-PIP3 phosphorylation-dephosphorylation cycle on KRas-functionalized lipid membrane in a PDMS chamber. The discussion is organized as follows: We first describe the strategy to crosslink KRas4b, one of the isoforms of KRas, to a supported lipid bilayer. We then study the effect of KRas4b on PI3K-mediated PIP2 phosphorylation and PTEN-mediated PIP3 dephosphorylation. Lastly, we characterize the interconversion of PIP2 and PIP3 by injecting PI3K and PTEN sequentially into the channel, demonstrating that this setup provides a useful platform to study dynamic equilibrium of PIP2 / PIP3 in the presence of both PI3K and PTEN in the future.

6.1 Cross-Linking of KRas4b to a Supported Lipid Bilayer through Cys-Maleimide Coupling

In the cell, KRas4b binds to the membrane mainly through the insertion of its lipid anchor, which is attached to the C-terminus of KRas4b through posttranslational modification. In our *E. Coli* expression system, however, no posttranslational modification occurs; therefore, we crosslinked KRas4b to the model membrane through cysteine and maleimide coupling. There are two major rationales behind this design. First, crosslinking through covalent bonding is strong and irreversible. The maleimide-functionalized lipid membranes can be easily prepared by mixing a maleimide-containing lipid (mccPE) with other phospholipids in a stock solution and following the standard procedures to prepare lipid vesicles and then supported lipid bilayers (Chapter 2). Second, KRas binds to the membrane at the C-terminus *in vivo*, a feature that we can recreate through coupling. We mutated Cys118 to serine in KRas4b, leaving one cysteine at the C-terminus (position 186). Therefore, we could attach the KRas4b at the C-terminus and preserve its orientation on the model membrane. It has been shown that Ras remains active after cross-coupling to a lipid membrane using this strategy [114, 138].

To investigate the crosslinking of KRas4b to mccPE, we incubated KRas4b-Alexa488 with a lipid membrane with and without mCCPE for an hour and then removed unbound KRas4b with buffer. The Alexa488 fluorescence signal on the bilayer with mccPE was significantly higher than on the bilayer without mCCPE (Fig 6.1). From this, we concluded that maleimide-containing lipid mccPE is sufficient for the covalent linkage of KRas4b to the lipid membrane.

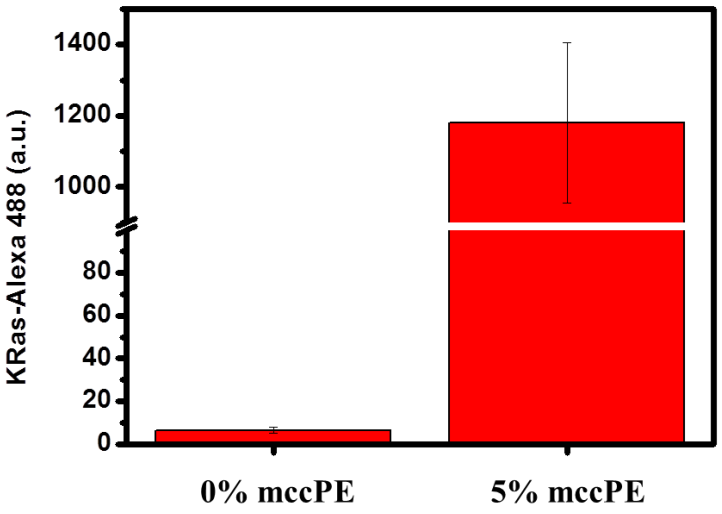

Fig 6.1 Fluorescence of KRas-Alexa 488 on lipid membranes containing 0% and 5% mccPE. The membrane composition: *n*% mccPE / 0.5% PIP3 / (99.3-*n*) % DOPC / 0.2% DiI. *n*=0 (left) and *n*=5 (right). Lipid membranes are incubated with KRas4b-Alexa488 for an hour and then washed with buffer. The y-axis represents the fluorescence intensity of Alexa 488. Data points are mean ± SEM (*N*=2 measurements).

6.2 Effect of KRas on PI3K Activation

Having characterized the coupling of KRas4b to the lipid membrane, we proceeded to study PI3K-mediated PIP2 phosphorylation in the presence of membrane-bound KRas4b and KRas4b in solution (Fig 6.2). Clearly, the PIP2 phosphorylation rate increased when the membrane was functionalized with KRas4b. Even when the KRas4b was merely in solution (i.e. not membrane-bound), the rate of PIP2 phosphorylation was still faster than the reaction without KRas4b.

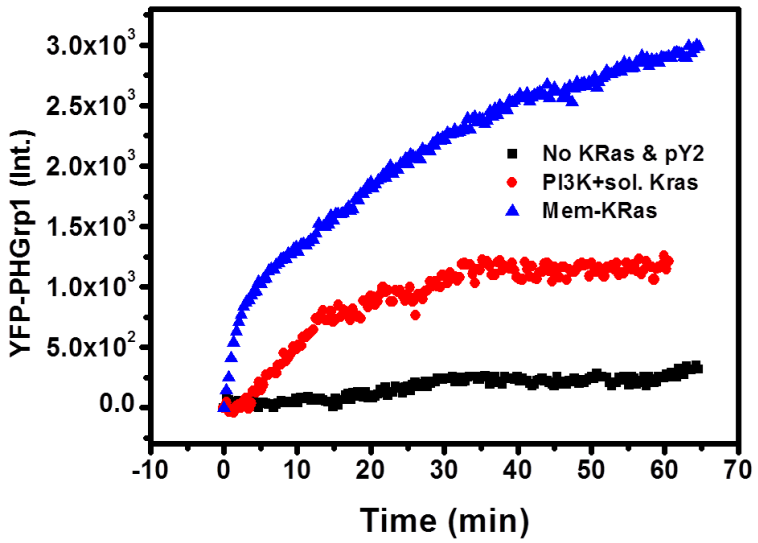

Fig 6.2 Effect of membrane-bound and solution KRas4b on PI3K activation. The membrane composition: 1% PIP2 / 5% mccPE / 15% DOPS / 78.8% POPC / 0.2% DiI. Bilayers are first equilibrated with YFP-PH-Grp1. Then, enzyme (i.e. PI3K, PI3K+KRas) is coinjected with YFP-PH-Grp1 and time-lapse imaging is started. The y-axis represents the fluorescence signal of YFP-PH-Grp1. The bulk concentration of YFP-PH-Grp1 and PI3K are 300 nM and 215 nM, respectively. No pY2 is involved in the reaction. The bulk concentration of KRas4b in solution (red circles) is 5 μM. The buffer contains [DTT] = 1 mM; [$MgCl_2$] = 5 mM; [ATP] = 100 μM. Preparation of membranes with and without membrane-bound KRas are described in Chapter 2.8 and 2.4, respectively.

The KRas4b and pY2 were shown to be able to activate PI3K, respectively, we then further asked the question that whether PI3K could be further activated in the presence of both KRas4b and pY2. To address this question, we studied the PI3K-mediated PIP2

phosphorylation in the presence / absence of KRas4b, pY2, or both, and the overall result was summarized in Fig 6.3. When PI3K is activated by both pY2 and membrane-bound KRas4b simultaneously, the rate of PIP3 synthesis is faster than the system with PI3K activated by either pY2 or KRas4b. The result shows that pY2 could activate PI3K with KRas4b synergistically, which is consistent with Vicinna et al. observation [139].

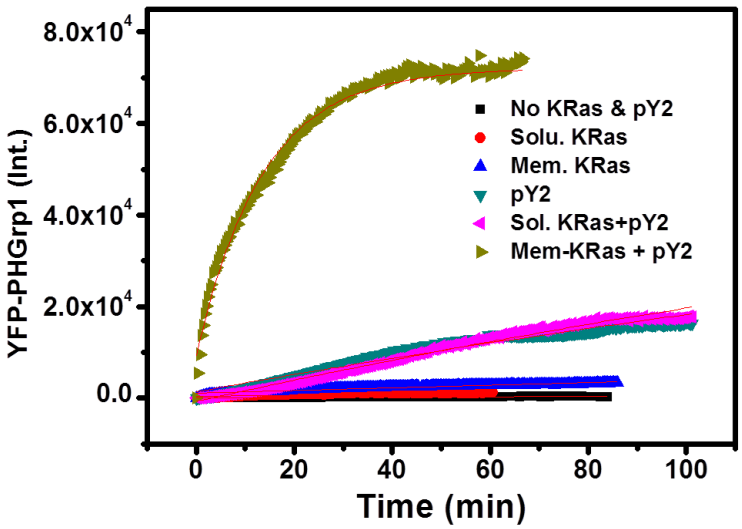

Fig 6.3 PI3K is activated by pY2 and membrane-bound KRas4b synergistically. The membrane composition: 1% PIP2 / 5% mccPE / 15% DOPS / 78.8% POPC / 0.2% DiI. Bilayers are first equilibrated with YFP-PH-Grp1. Then, enzyme is coinjected with YFP-PH-Grp1 and time-lapse imaging is started. The y-axis represents the fluorescence signal of YFP-PH-Grp1. The bulk concentrations of proteins are listed below: [YFP-PH-Grp1] = 300 nM, [PI3K] = 215 nM, [KRas4b] = 5 μM, [pY2] = 25 μM. The buffer contains [DTT] = 1 mM; [$MgCl_2$] = 5 mM; [ATP] = 100 μM. Preparation of membranes with and without membrane-bound KRas are described in Chapter 2.8 and 2.4, respectively.

6.3 Effect of Membrane-Bound KRas on PTEN Kinetics

Membrane-bound KRas4b serves as key activator of PI3K, but its effect on PTEN activity is not known. Before characterizing the interconversion of PIP2 / PIP3 by PI3K and PTEN, we first characterized how the density of KRas4b bound on the membrane affected PTEN-mediated PIP3 hydrolysis. PIP3 hydrolysis kinetics were monitored at the lipid membrane with different amounts of mccPE (0%, 1%, and 5%) in the presence or absence of KRas4b (Fig 6.4). The resulting kinetics data showed that in the presence of a KRas4b-functionalized membrane, the rate of PIP3 hydrolysis by PTEN decreased as KRas4b density increased, especially at 5% mccPE. In the absence of KRas4b, there was no significant difference of PIP3 hydrolysis rate between bilayers with 0% and 5% mccPE. This suggests that the amount of mccPE is not a critical factor affecting PIP3 dephosphorylation.

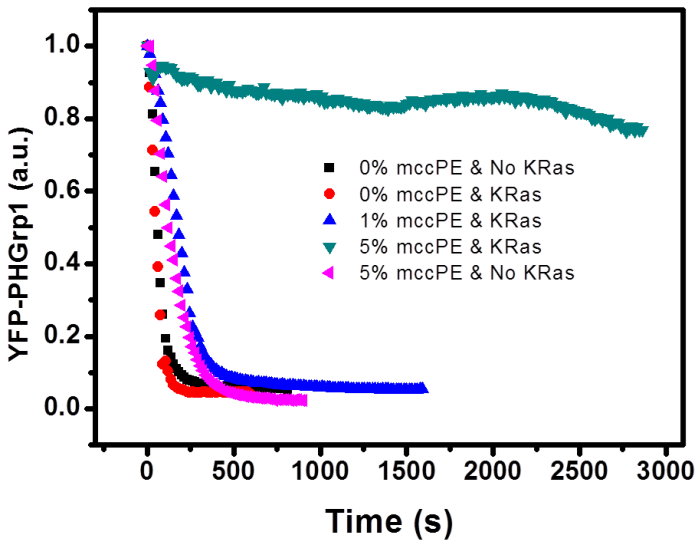

Fig 6.4 The rate of PIP3 hydrolysis kinetics by PTEN slow down with increasing density of membrane-bound KRas4b. The membrane composition: 1% PIP2 / 0.5% PIP3 / *n*% mccPE / 15% DOPS / (83.3-*n*) % DOPC / 0.2% DiI. Bilayers are first equilibrated with YFP-PH-Grp1. Then, PTEN is coinjected with YFP-PH-Grp1 and time-lapse imaging is started. The y-axis represents the fluorescence signal of YFP-PH-Grp1. The bulk concentrations of YFP-PH-Grp1 and PTEN are 300 nM. The buffer contains [DTT] = 1 mM; [$MgCl_2$] = 5 mM. Preparation of membranes with and without membrane-bound KRas are described in Chapter 2.8 and 2.4, respectively.

6.4 Forced PIP3 / PIP2 Oscillation on a KRas4b-Functionalized Membrane by Sequential PTEN / PI3K Injection in a PDMS Channel

Having characterized the effect of membrane-bound KRas4b on PTEN and PI3K kinetics, we proceeded to study whether the PIP2 / PIP3 phosphorylation-dephosphorylation cycle could be established dynamically and reversibly by injecting sensor protein, PTEN, and PI3K, sequentially into a PDMS chamber (Fig 6.5). After functionalizing with KRas4b, the bilayer was first equilibrated with the sensor protein YFP-PH-Grp1 (step 1). After injecting PTEN, membrane-bound Grp1 dissociated from the membrane (step 2). The fluorescence signal on the membrane remains low even after new Grp1 was injected (step 3), which excludes the possibility that Grp1 dissociation from the membrane is caused by competitive binding of PTEN, but rather is caused by PIP3 hydrolysis by PTEN. After pulse injecting PI3K, the Grp1 signal on the membrane increases (step 4). This signal was enhanced by adding more Grp1 (step 5). To exclude

the possibility that the signal increased due to nonspecific binding of sensor proteins to areas of exposed glass surface, which could be created when the bilayer is damaged by bubbles, PTEN was co-injected with Grp1 into the channel (step 6). The Grp1 signal decreased significantly and did not recover when more Grp1 was introduced (step 7), thus excluding the possibility that Grp1 was binding nonspecifically.

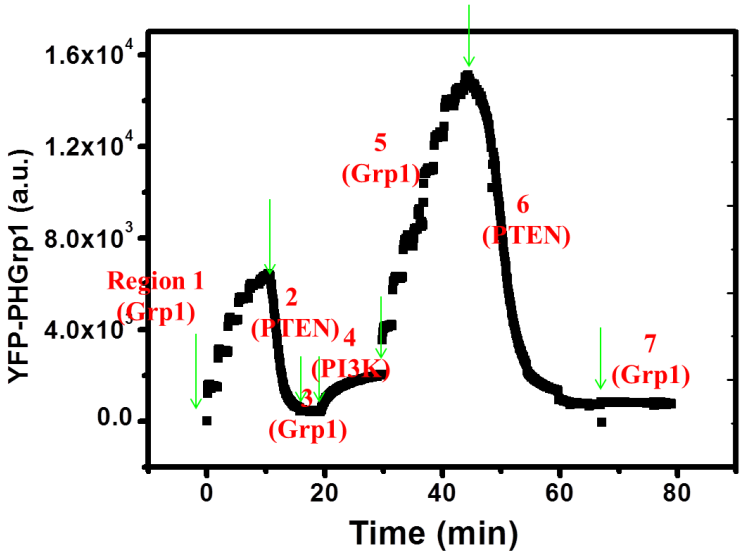

Fig 6.5 PIP3 oscillations forced by injecting PTEN and PI3K sequentially in a PDMS chamber with a KRas4b-functionalized lipid membrane. The membrane composition: 1% PIP2 / 0.5% PIP3 / 1% mccPE / 15% DOPS / 82.3% DOPC / 0.2% DiI. Seven steps of protein injection occur sequentially in the chamber: YFP-PH-Grp1 (step 1), PTEN and YFP-PH-Grp1 (step 2), YFP-PH-Grp1 (step 3), PI3K, pY2, and YFP-PH-Grp1 (step 4), YFP-PH-Grp1 (step 5), PTEN and YFP-PH-Grp1 (step 6), and YFP-PH-Grp1 (step 7). The bulk concentration of YFP-PH-Grp1, PTEN, PI3K, and pY2 are 300 nM, 300 nM, 320 nM, and 25μM, respectively. The buffer contains [DTT] = 1 mM;

[$MgCl_2$] = 5 mM; [ATP] = 100 μM. Preparation of KRas4b-functionalized membrane was described in Chapter 2.8.

To summarize, the essential findings displayed in Fig 6.5 demonstrates that the PDMS chamber and supported lipid bilayer provides a good micro reactor platform to characterize dynamic equilibrium of phosphoinositides in the presence of PTEN and PI3K.

6.5 Summary

In this chapter, we characterized the effect of KRas4b on PI3K-mediated PIP2 phosphorylation and PTEN-mediated PIP3 hydrolysis. On the one hand, membrane-bound KRas4b is shown to increase PIP2 phosphorylation not only by activating PI3K directly, but also by using the phosphopeptide pY2 to activate itsynergistically. On the other hand, high density membrane-bound KRas4b slows down the rate of PIP3 hydrolysis by PTEN significantly. This result can be rationalized by the hypothesis that high density KRas4b can slow down PTEN's access to the lipid substrate due to steric effects. This may provide a possible mechanism for how Ras GTPase regulates PIP3 hydrolysis on cell membrane: by affecting both PI3K and PTEN. Lastly, we characterized PIP2-PIP3 interconversion by PTEN / PI3K in the PDMS channel, which provides a good micro platform to characterize dynamic equilibrium of phosphoinositides.

Chapter 7. Complex Dynamics of Phosphoinositides Induced by a Kinase-Phosphatase Pair (PI3K and PTEN) on Si Bead-Supported Lipid Bilayer[9]

7.1 Characterization and Validation of an Experimental Platform to Study Enzymatic PIP2 and PIP3 Interconversion

In Chapter 3 we have fully characterized and validated our fluorescent sensor protein on the silica bead-supported lipid bilayer (BSM), we proceeded to employing them for further evaluation of the catalytic action of both enzymes (experimental design in Fig 3.1, Chap 3). To evaluate the function of PI3K on BSMs, sensor proteins were mixed with PI3K in microcentrifuge tubes and incubated between 0 and 3 min, then PIP2-rich BSMs were added and incubated for 10 min. In all of our experiments, PI3K was activated (through pre-incubation) with a phosphopeptide (pY2) with a sequence from the human platelet-derived growth factor receptor beta (PGFRβ) [87] (see Chapter 2.3.5 for details). After these incubations, BSMs were transferred to an imaging chamber and analysis of fluorescence intensities indicated the essentially complete conversion of PIP2-rich to PIP3-rich bilayers (Fig 7.1Ai, also compare Fig 3.2C, bottom right, for the initial state fluorescence distribution). Note that this transfer approach (as opposed to mixing components in the imaging chamber) greatly facilitates mixing of the components, as well as working with small volumes and amounts of enzymes.

[9] Parts of this chapter are reproduced by currently submitted work: Liu, C.; Zimmerman, Z. E.; Grasso, M.; Gosh, A.; Marmorstein, R.; Radhakrishnan, R.; Baumgart, T., Bistable reaction behavior in PTEN / PI3K mediated phosphoinositide lipid conversion.

We considered the artifactual possibility that enzymes were slowly inactivated through artifacts such as the adsorption to tube walls, or by the added BSMs, such as through adsorption of enzymes to defects in the solid supported membrane, potentially to an uneven extent comparing different beads, or by depletion from the solution through binding to BSMs membranes. Obviously, such phenomena would interfere with the analysis of steady state kinetics that is to follow below. To exclude effects from potential adsorption to tube walls, we varied enzyme incubation time in the microcentrifuge tube before adding BSMs. The results did not depend on an incubation window that spanned 0 – 3 min (not shown). To exclude enzyme inactivation by artifacts introduced by the BSMs, a new batch of PIP2-rich BSMs was added to the same sample tube after observing PI3K mediated catalytic conversion. Following this step, we also observed phosphorylation of the newly added PIP2-rich BSMs by PI3K (Fig 7.1Aii). Likewise, initially PIP3-rich beads were mixed with sensors and PTEN, resulting in conversion to PIP2-rich beads (Fig 7.1Bi). Fresh PIP3-rich beads added in a second step to the reaction mixture, were also converted to PIP2-rich BSMs (Fig 7.1Bii). Overall, these results imply that after substrate depletion, enzymes remain available for conversion of freshly added reactant.

To round off the description of our reaction system, we further discuss the dependence on product and substrate concentrations of the reactions catalyzed by PTEN, and PI3K, respectively. It has previously been shown that PIP3 dephosphorylation by PTEN is an autocatalytic reaction, i.e. the reaction rate is accelerated by the product PIP2 [84, 96, 100, 121]. Kinetic traces of PIP3 dephosphorylation by PTEN at various percentages of PIP2 (see Chapter 4, Fig 4.4) are shown in Fig 7.1C. The reaction rate

increased with increasing initial membrane PIP2 concentration, consistent with an autocatalytic reaction mechanism. Our prior research were consistent with the notion that the positive feedback can be explained by a combination of allosteric activation and membrane-recruitment of PTEN by PIP2, and comparison of kinetic data to a newly developed model (that will be further elaborated on below) allowed us to determine catalytic parameters for this complex reaction [78].

Kinetic analysis of PIP2 phosphorylation by PI3K on our BSMs is consistent with the reaction following Michaelis-Menten type kinetics (Fig 7.1D). The analysis of initial velocities (slopes of the progress curves in the insert of Fig 7.1D) as a function of PIP2 content of the membrane yielded a Michaelis-Menten constant of K_m = 1.06 ± 0.74 % PIP2. Contrary to PTEN, we do not presently have experimental evidence for a PI lipid mediated feedback mechanism in the function of PI3K.

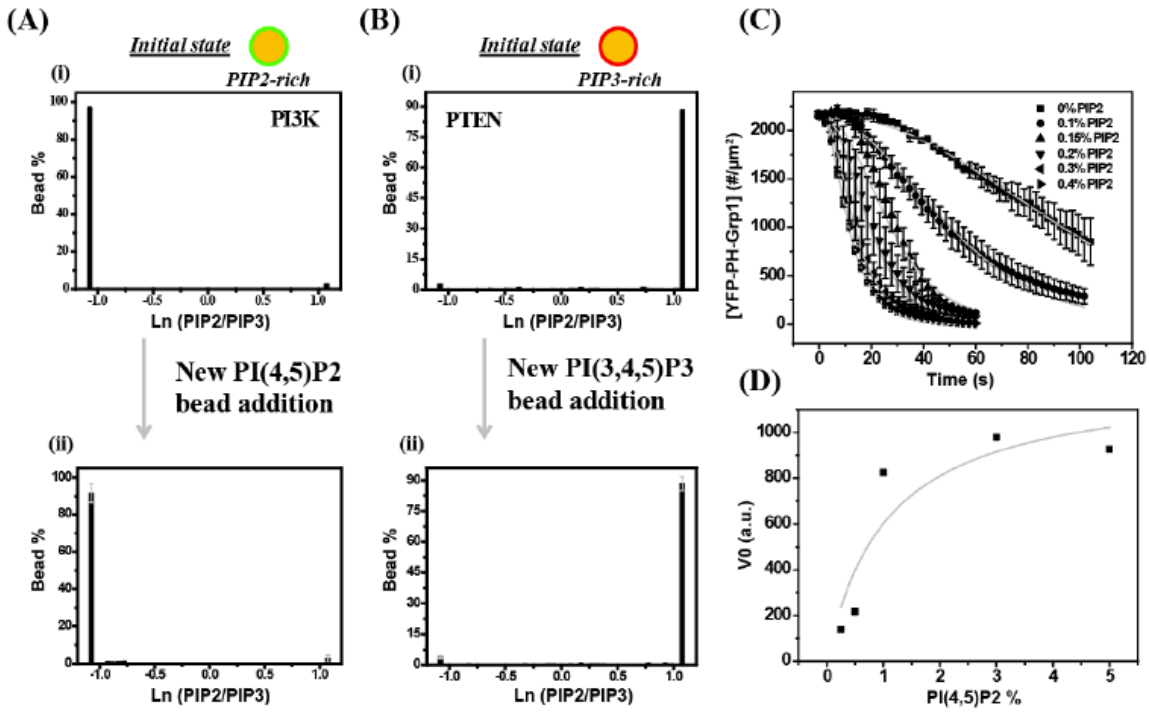

Fig 7.1. PIP2 and PIP3 on supported lipid bilayers are interconverted by a PI3K and PTEN. (A). (i). PI3K-mediated conversion of BSMs initially composed of 2% PIP2 / 5% DOPS / DOPC / 0.2% Naphthopyrene. The sensor proteins and PI3K were mixed in a microcentrifuge tube for 3 minutes, after which BSMs were added (top, [PI3K] = 570 nM). (ii). After the PIP2-rich BSMs were converted to PIP3 by PI3K (10 min), a new batch of PIP2-rich BSMs (preincubated with biosensors so as to not affect their final concentrations) was added (without adding fresh enzyme) and incubated for 20 min (bottom, [PI3K] = 220 nM, lower concentration results from dilution). The bulk concentrations of mCherry-PH-Grp1 and EGFP-PH-PLCδ1 were 110 nM and 375 nM, respectively, throughout the experiment. (B). (i). The distribution of PIP3 and PIP2 on BSMs composed 2% PIP3 / 5% DOPS / DOPC / 0.2% Naphthopyrene in the presence of PTEN. The sensor proteins and PTEN were mixed in a microcentrifuge tube for 3 minutes, then BSMs were added (top, [PTEN] = 12.5 nM). (ii). When the PIP3-rich BSMs were converted to PIP2 by PTEN, a new batch of PIP3-rich beads was added and incubated for 10 min (bottom, [PTEN] = 4.8 nM). The bulk concentration of mCherry-PH-Grp1 and EGFP-PH-PLCδ1 were 110 nM and 375 nM, respectively. Data points are mean ± SEM (Number of beads $\geqq$ 70, N = 2). The x-axis represents the natural log of the sensor fluorescence intensity ratio, corresponding to the number ratio of PIP2/PIP3. The threshold of ratio of PIP2/PIP3 or PIP3/PIP2 = 3. (C) PIP3 dephosphorylation kinetics by PTEN on planar supported lipid bilayer with various % of PIP2 (same as Figure 4.4). The lipid composition is 0.2% PIP3 / n% PIP2 / 5% DOPS / DOPC / 0.2% TR-DHPE. n = 0 (square), n = 0.1 (circle), n = 0.15 (triangle), n = 0.2 (down-pointing triangle), n = 0.3 (left-pointing triangle), n = 0.4 (right-pointing triangle). The bulk concentration of YFP-

PH-Grp1 and PTEN are 300 nM and 100 nM, respectively. The y-axis represents the surface concentration of YFP-PHGrp1. (D) PIP2 phosphorylation kinetics on planar lipid bilayer by PI3K. The lipid composition is n% PIP2 / 5% DOPS / POPC / 0.2% DiI. n = 0.25, 0.5, 1, 3, 5. The bulk concentration of YFP-PH-Grp1 and PI3K are 300 nM and 215 nM, respectively. The y-axis represents the initial velocity of PIP2 phosphorylation. The data was fitted with the Michaelis-Menten equation to yield K_m = 1.06 ± 0.74 % PIP2.

7.2 Bistable Steady-States of PIP3 / PIP2 are Observed at Intermediate PTEN / PI3K Ratios Dependent on the Initial Lipid Composition.

The presence of positive feedback through PIP2 in PTEN-mediated catalysis is expected to lead to complex reaction dynamics, such as the formation of bistable steady states, which would imply hysteresis [60, 140-142]. Therefore, having characterized sensor proteins and each enzyme separately via the BSM platform, we proceeded to ask the question how, in the simultaneous presence of both PTEN and PI3K, the observed BSM states would depend on a) initial PIP composition and b) on the concentration ratio of the two enzymes.

To address this question, we used two different initial BSM compositions containing either 2% PIP3 (no PIP2) or 2% PIP2 (no PIP3). We incubated these two different batches of BSMs with PI3K at a concentration that was held constant (along with ATP and pY2), while we varied the PTEN concentration in different directions: for BSMs initially rich in PIP3 we raised the PTEN concentration in three steps (via successive addition, path 1, Fig 7.2A), and for BSMs initially rich in PIP2 we decreased the PTEN

concentration in three steps (by successive dilution, path 2, Fig 7.2B). In other words, four different PTEN/PI3K concentration ratios were adjusted using the same population of BSMs for each of the two paths, and while varying enzyme concentration ratios in opposing directions. These enzyme concentration ratios were selected such that along each path, the BSMs would be close to completely converted into the PIP composition opposite to the initial one (compare first and last rows in Fig 7.2A, B).

The first striking observation that is made in the histogram analysis of BSM PIP2/PIP3 ratios along both paths, is that for intermediate concentration ratios (second and third row in Fig 7.2A, B), two bins are predominantly populated: those corresponding to the extreme PIP2/PIP3 ratios. Conversely, intermediate color distributions, such as observed for intermediate PIP2/PIP3 ratios in the absence of enzyme in the histogram shown in Fig 3.2C (middle of the bottom row, in Chap 3), are not significantly populated in the presence of the enzyme mixture. Probability distributions thus appear to be bimodal for the case of intermediate enzyme concentration ratios (second and third row in Fig 7.2A, B). In other words, individual BSMs appear to switch from a PIP3 rich to a PIP2 rich composition along path 1, and vice versa for path 2.

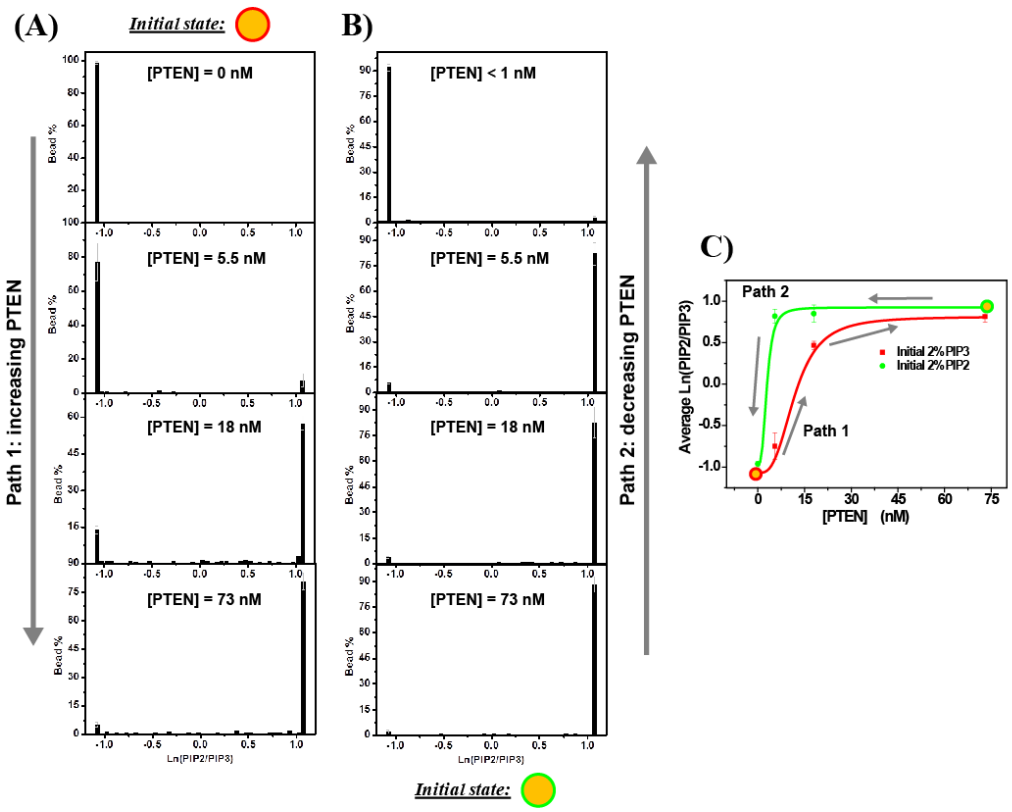

Fig 7.2. Hysteresis in PIP reaction cycle results from variation of PTEN concentration. (A). For path 1, we started with incubating PI3K and sensor proteins with PIP3-rich BSMs. Then we systematically increased the PTEN concentration until all PIP3 converted to PIP2 at fixed PI3K concentration for the same batch of BSMs (left column). (B). For path 2, we started with incubating PTEN and sensor proteins with PIP2-rich beads, then added PI3K, and then diluted PTEN systematically for the same batch of BSMs (right column). The PI3K concentration remained fixed during titration for both path 1 and 2 ([PI3K] = 570 nM). The PTEN concentration in path 1 and path 2 is 0, 5.5, 18, 73 nM from top to bottom. The initial BSM compositions were 2% PIP3 (left, indicated by BSM with red circle), or 2% PIP2 (right, green circle), each with 5% DOPS / DOPC / 0.2% Naphthopyrene. 2% PIP3 and 2% PIP2. The bulk concentration of

mCherry-PH-Grp1 and EGFP-PH-PLCδ1 are 110 nM and 375 nM, respectively. Data points are mean ± SEM (Number of BSMs $\geqq$ 90, N = 2). In all cases the BSMs were incubated with enzymes and sensor proteins for 10 min. (C). Hysteresis plot of PIP2 and PIP3 distribution as function of PTEN concentration (with PI3K concentration fixed).

We sought to support this conclusion through the following control experiments. We verified that the multiple pipetting steps did not lead to artifactual fluorescence changes of beads. A mock titration (in the absence of enzymes) corresponding to one of the paths in Fig 7.2 did not lead to measurable color changes of BSMs (Fig S7.1). Secondly, we added enzyme inhibitors to BSMs incubated with intermediate concentrations of both enzymes, where initially bimodal behavior was observed (Fig 7.2A). Inhibition of PI3K resulted in a conversion of BSMs from a bimodal distribution to one where close to all BSMs became PIP2 rich (Fig S7.2), and inhibition of PTEN turned the bimodal distribution into one where essentially all BSMs became PIP3 rich. Together, these results demonstrate that bimodal PIP composition distributions are actively maintained, and the last experiment also demonstrates that ATP does not become depleted over the time course of our experiments. Finally, we considered the possibility that a variable total PIP lipid content of different BSMs might cause variable enzymatic activity, resulting in beads with variable colors. To exclude this scenario, we verified absence of a correlation between fluorescence intensity ratio (i.e. BSM color) and total amount of fluorescence (sum of both biosensors), indicating the the total PI content of individual BSMs is

uncorrelated with the PIP2/PIP3 ratio observed in individual BSMs from the mixed population found at intermediate enzyme concentration ratio.

The observations above suggest complex reaction kinetics, and are consistent with the existence of two major stable reaction states in our system, i.e. bistability. The latter's hallmark is the phenomenon of hysteresis, where states of the system depend on its history [140, 142], which we will discuss in more detail in the following.

Comparing the histograms of Fig 7.2A,B for the corresponding enzyme concentration ratios in each path, differences in the distributions are observed. In other words, the resulting histogram for each enzyme concentration ratio appears to be dependent on the pathway along which it was obtained, i.e. to depend on the initial state of the BSM. In order to illustrate this graphically, we plotted the BSM composition average values obtained from each histogram in Fig 7.2A,B against the PTEN concentration, see Fig 7.2C. If the reaction system can reach only a single average value at a specific PTEN concentration, then the final phosphoinositide compositions evolving from the initial state compositions are expected to become identical for a given enzyme concentration ratio irrespective of whether initial bilayers consist of 2% PIP3, or of 2% PIP2, or any intermediate initial composition. If bistability were to be admissible over some range of enzyme concentrations, then we would expect, within that range, to observe different final states of the reaction system depending on the initial composition of the BSMs, wheras outside of that range, single average values would be found. This is precisely the behavior that is displayed in Fig 7.2C: identical average values are reached

at both the highest, and the lowest, PTEN concentrations independent from the pathway chosen. However, pathway dependence is obvious for intermediate concentrations.

We hypothesize that Fig 7.2 depicts steady states of the reaction system, an assumption that requires further discussion. The notion of a steady state (as opposed to transient, or equilibrium states) in a cyclic reaction system implies in our case that a) PIP composition does not change over a time scale comparable to reaction times observed in the absence of a counter-acting enzyme (see Fig 7.1) and that b) ATP remains available to drive the steady state reaction (which, as mentioned above, we demonstrated through inhibition of PTEN, see Fig S7.2). We tested the first condition by using a doubled incubation time (i.e. comparing 20 min to 10 min incubation) – the resulting histograms did not change significantly (data not shown), indicating that the results displayed in Fig 7.2 do not correspond to transient states of the reaction system. We emphasize again that the finding of bimodal histograms in the presence of PTEN and PI3K cannot be explained by the artifactual inactivation of one or both of the enzymes (or by alternative irreversible phenomena) over the course of the experiment, as we have demonstrated through results shown in Fig 7.1, as well as through inhibition of one of the enzymes. We also note that the bimodal behavior is highly reproducible, as the error bars in Figs 7.2A,B show. Potential random pipetting errors therefore also cannot explain the bimodal behavior with hysteresis.

Having excluded these potential artifacts further raised confidence in the hypothesis that hysteresis and bimodality and are a result of ongoing cyclic catalysis in a bistable reaction system affected by noise (the latter of which we will further discuss below). So

far we have assessed hysteresis by varying the concentration of PTEN, an enzyme for which solid evidence of product-related feedback exists [78, 100, 121]. Modeling of our catalytic system with a deterministic reaction model (see further below) predicts that hysteresis ought to be observable through variation of PI3K for a fixed concentration of PTEN, even in the absence of any feedback in the reaction mechanism of the kinase. Furthermore, from a biological point of view, it is generally believed that in response to receptor engagement, PI3K is being recruited to the membrane, raising its local concentration [43, 119]. Therefore, variation of the kinase concentration provides a biologically relevant scenario for us to biophysically explore, and this provided further opportunity to test our main hypothesis.

We therefore designed an experiment equivalent to that shown in Fig 7.2, but instead of varying the PTEN concentration, we changed the PI3K concentration (via addition, path 1, Fig 7.3A, or by dilution, path 2, Fig 7.3B), while holding PTEN concentration constant. The results are fully consistent with earlier observations: in an intermediate concentration range, the typical bimodal probability distribution of PI composition is observed (Fig 7.3A,B) with insignificant population of intermediate PIP2/PIP3 ratios even for intermediate enzyme concentration ratios. Furthermore, average values determined from the histograms referring to the two different paths in Fig 7.3A,B show hysteresis (Fig 7.3C). This experiment therefore further supports the notion of bistability (leading to steady state hysteresis) in a noisy reaction system (leading to bimodal probability distributions of BSM compositions).

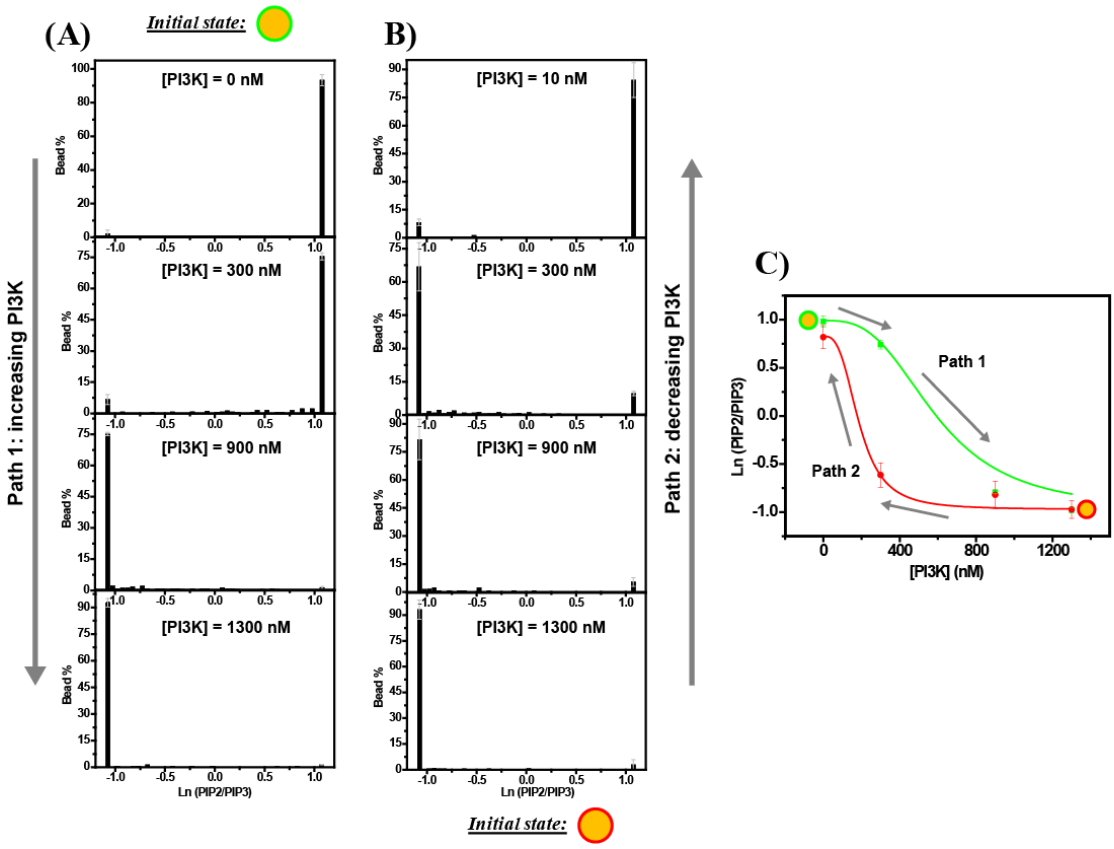

Fig 7.3. Hysteresis in PIP reaction cycle results from variation of PI3K concentration. (A). For path 1, we first incubated PTEN and sensor proteins with PIP2-rich BSMs. Then we increased the PI3K concentration in three steps until all PIP2 converted to PIP3 at fixed PTEN concentration for the same batch of BSMs (left column). (B). For path 2, we first incubated PI3K and sensor proteins with PIP3-rich BSMs. Then we added PTEN and gradually diluted PI3K for the same batch of BSM. The PTEN concentration remained fixed at 7.5 nM during titration for both paths. The PI3K concentrations were 0, 300, 900, 1300 nM from top to bottom. Initial BSM compositions were 2% PIP2 (A) or 2% PIP3 (B) with 5% DOPS / DOPC / 0.2% Naphthopyrene. The bulk concentration of mCherry-PH-Grp1 and EGFP-PH-PLCδ1 was

110 nM and 375 nM, respectively. Data points are mean ± SEM (Number of BSMs ≧ 90, $N = 2$). In all cases, the BSMs were incubated with enzymes and sensor proteins for 10 min before transfer to the imaging chamber. (C). Plot of average values of logarithmic PIP2/PIP3 ratios resulting from the histograms displayed in (A) and (B).

The evidence giving rise to our main hypothesis thus far has relied in part on a series of addition and dilution (of enzymes) steps to reveal hysteresis. This experimental mode allowed us to demonstrate that a given BSM population remained responsive to enzyme concentration ratio changes over the time course of each experimental series. The reproducibility of our histograms allowed us to exclude *random* pipetting errors that might lead to erroneously concluding the existence of pathway dependence. However, in the experimental mode underlying the results presented so far, there remains a possibility that *systematic* errors introduced artifactual pathway dependence. Such errors might include artifactual contributors such as systematic pipetting errors, enzyme depletion through adsorption to reaction chamber walls and pipette tips, among others. Such types of errors might result in an artifactual pathway dependence. In order to be able to exclude the possibility of such systematic errors related to solution exchanges, we designed an experiment where all solutions were handled identically – the sole difference for a given enzyme concentration ratio in this alternative experiment was the intial lipid composition of the BSMs. Accordingly, one set of incubations used initially PIP2 rich BSMs (Fig 7.4A), and the other set used initially PIP3 rich BSMs (Fig 7.4B).

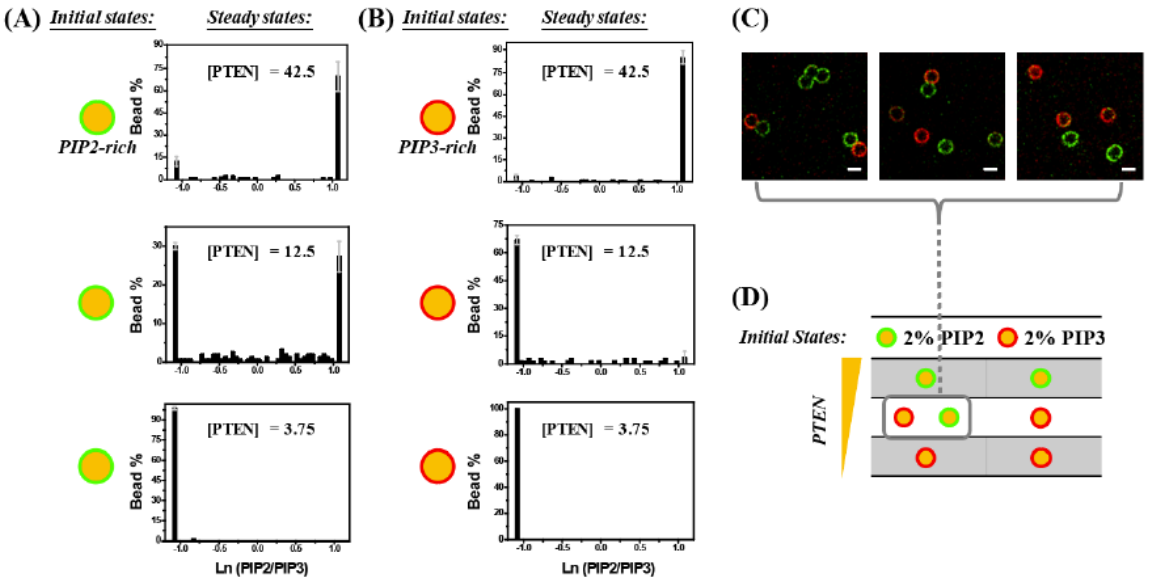

Fig 7.4. Steady-states in PIP3 / PIP2 reaction cycle depend on initial PIP state and PTEN concentration. Histogram of steady-states of PIP3 / PIP2 on bilayer at different PTEN concentrations with PI3K concentration fixed ([PI3K] = 570 nM). BSMs were simultaneously mixed with sensor proteins and enzymes and incubated for 30 min before observation. Each BSM sample at specific PTEN concentration involved separate incubation. Data points are mean ± SEM (Number of BSMs $\geqq$ 90, N = 2). Initial BSM compositions were 2% PIP2 or 2% PIP3 / 5% DOPS / DOPC / 0.2% Naphthopyrene. (A). 2% PIP2 (left, green circle) and (B). 2% PIP3 (right, red circle). The bulk concentrations of mCherry-PH-Grp1 and EGFP-PH-PLCδ1 were 110 nM and 375 nM, respectively. The x-axis represents the natural log of number ratio of PIP2 and PIP3. The threshold of ratio of PIP2/PIP3 or PIP3/PIP2 = 3. (C). The representative images of mixture of PIP3-rich and PIP2-rich BSMs at the intermediate PTEN concentration (with PI3K fixed) are shown. Scale bars: 30 μm. (D). Summary of steady-state of PIP3 / PIP2 at different

PTEN concentration with PI3K concentration fixed. The steady-state of PIP2-rich beads shows up as a green circle and PIP3-rich BSMs are shown in red.

Consistent with the findings presented in Figs 7.2 and 7.3, at both low (3.75 nM) and high (42.5 nM) concentration of PTEN, the same final state of the reaction system was reached regardless of whether BSMs initially consisted of 2% PIP3 or of 2% PIP2, see Fig 7.4A,B. At low PTEN concentration (3.75 nM), the system was PIP3-rich, while at high PTEN concentration (42.5 nM), it was PIP2-rich. At the intermediate concentration of PTEN (12.5 nM), different final states were reached dependening on the initial composition of the BSMs. In particular, for this intermediate PTEN concentration, initially 2% PIP3 containing BSMs remained PIP3-rich, whereas initially 2% PIP2 containing beads evolved into a mixed, bimodally distributed population of PIP3-rich and PIP2-rich BSMs (see Fig 7.4A, B middle row). Representative fluorescence images showing the mixed population resulting from the PIP2 rich initial state are available in Fig 7.4C. A schematic summary of final states of phosphoinositide compositions at different PTEN concentrations, observed with two different initial lipid compositions, is shown in Fig 7.4D.

We note that the middle panel of Fig 7.4A shows the most extreme evidence for a bimodal probability distribution that we have presented. That said, it has to be noted that while about 60% of BSMs have compositions corresponding to the extremal bins (Fig 7.4A middle), the remaining fraction shows a wide distribution of colors. At this point we can only speculate as to the origin of this heterogeneity. One possible reason might be the

occurrence of incompletely fused lipid bilayers on BSMs. Under bistable conditions, such membrane patches might assume different lipid compositions. If patch dimensions are below the optical resolution limit, this might macroscopically lead to the observation of some BSMs with mixed color. However, we emphasize again the dramatic difference of the distribution in Fig 7.4A (middle) compared to the case in the absence of enzymes shown in Fig 3.2D, middle panel of bottom row. In both cases, the average value of fluorescence intensity ratios is close to PIP2/PIP3 = 1. However, a monomodal distribution is obtained in the absence of enzymes (Fig 3.2D, in Chapter 3).

To summarize, the essential findings displayed in Figs 7.2 and 7.3 are reproduced with the different experimental protocol underlying results shown in Fig 7.4. To conclude, our experiments have provided strong evidence for bistable reaction behavior and hysteresis. A quantitative reaction model based on our earlier characterization of PTEN is presented in the discussion. The results of this model will lend further support to the notion of bistability in the PTEN / PI3K reaction system.

7.3 Theoretical Model of PI(3,4,5)P3 / PI(4,5)P2 Bistability Induced by a Kinase-Phosphatase Pair with a Positive Feedback Loop

It is well know that a single-site reaction cycle involving phosphatase and kinase as well as phosphorylated (M^p) and dephosphorylated (M) species can yield a bistable switch if M exerts positive feedback on the phosphatase [60, 142]. Steady state solutions of such a kinetic system involves an unstable state found in between two stable steady states, at high M and low M. We had shown earlier (Chapter 4, [78]) that the two known mechanisms, allostery and membrane recruitment, [84, 96, 100, 121] underlying PIP2-

modulated auto-catalysis (i.e. positive feedback) in PTEN-mediated PIP3 hydrolysis can be expressed through a single PIP2 production rate term. The fitting of this reaction model to kinetic data enabled us to determine reaction parameters that allow to fully describe the autocatalytic reaction kinetics of PTEN in our in-vitro system (Chapter 4, [78]). We demonstrate here that bistability can be observed through the amendment of our kinetic model for PIP3 hydrolysis through PTEN by a simple Michaelis-Menten term to account for PIP2 phosphorylation by PI3K.

In our model, concentration changes free PIP3 in the membrane are considered to be affected by the following rate terms (see Eq. 7.1): (1) hydrolysis through PTEN on the membrane not bound to PIP2, (2) hydrolysis through PIP2 bound PTEN, (3) phosphorylation of PIP3 by PI3K, as well as (4) binding and (5) unbinding of biosensor Grp1-PH. Concentration changes of free PIP2 are expressed through similar rate terms, additionally involving binding and unbinding of PTEN to PIP2 (see Eq. 7.2). Completing the model, additional rate laws (Eqs. 7.3-7.6) describe the membrane binding/unbinding kinetics of PTEN, of PLC, and of Grp1, as well as conservation of total PI lipid content of the membranes.

$$\begin{aligned}\frac{\partial[PIP3]_m}{dt} = &-k_{cat}^{PTEN}\frac{k_a^{PTEN}}{k_d^{PTEN}}[PTEN]_B\frac{[PIP3]_m}{K_M^{PTEN}+[PIP3]_m} - \\ &-k_{cat}^{PTEN-PIP2}\frac{[PIP2]_m^{\,n}}{(K_{PTEN-PIP2})^n+[PIP2]_m^{\,n}}[PTEN-PIP2]_m\frac{[PIP3]_m}{K_M^{PTEN-PIP2}+[PIP3]_m} \\ &+V_{\max}^{PI3K}\frac{[PIP2]_m}{K_M^{PI3K}+[PIP2]_m} - k_a^{Grp1}[Grp1]_B[PIP3]_m + k_d^{Grp1}[Grp1-PIP3]_m\end{aligned} \tag{7.1}$$

$$\frac{\partial [PIP2]_m}{dt} = k_{cat}^{PTEN} \frac{k_a^{PTEN}}{k_d^{PTEN}} [PTEN]_B \frac{[PIP3]_m}{K_M^{PTEN} + [PIP3]_m} +$$
$$+ k_{cat}^{PTEN-PIP2} \frac{[PIP2]_m^{\ n}}{(K_{PTEN-PIP2})^n + [PIP2]_m^{\ n}} [PTEN - PIP2]_m \frac{[PIP3]_m}{K_M^{PTEN-PIP2} + [PIP3]_m} \quad (7.2)$$
$$- V_{\max}^{PI3K} \frac{[PIP2]_m}{K_M^{PI3K} + [PIP2]_m} - k_a^{PLC} [PLC]_B [PIP2]_m + k_d^{PLC} [PLC - PIP2]_m$$
$$- k_a^{PTEN-PIP2} [PTEN]_B [PIP2]_m + k_d^{PTEN-PIP2} [PTEN - PIP2]_m$$

$$\frac{\partial [PTEN - PIP2]_m}{\partial t} = k_a^{PTEN-PIP2} [PTEN]_B [PIP2]_m - k_d^{PTEN-PIP2} [PTEN - PIP2]_m \quad (7.3)$$

$$\frac{\partial [PLC - PIP2]_m}{\partial t} = k_a^{PLC} [PLC]_B [PIP2]_m - k_d^{PLC} [PLC - PIP2]_m \quad (7.4)$$

$$\frac{\partial [Grp1 - PIP3]_m}{\partial t} = k_a^{Grp1} [Grp1]_B [PIP3]_m - k_d^{Grp1} [Grp1 - PIP3]_m \quad (7.5)$$

$$[PIP]_{total} = [PIP3]_m + [PIP2]_m + [Grp1 - PIP3]_m + [PLC - PIP2]_m + [PTEN - PIP2]_m \quad (7.6)$$

$[PTEN]_B$, $[Grp1]_B$, and $[PLC]_B$ (unit: μM) are bulk concentration of PTEN, Grp1, and PLC, respectively. $[PIP3]_m$, $[PIP2]_m$, $[PTEN\text{-}PIP2]_m$, $[PLC\text{-}PIP2]_m$, and $[Grp1\text{-}PIP3]_m$ (unit: μMm) are surface concentration. The association constant is k_a (unit: m/s for k_a^{PTEN} and $\mu M^{-1}s^{-1}$ for $k_a^{PTEN-PIP2}$), the dissociation constant is k_d (unit: s^{-1}), and the Michaelis-Menten constant is K_M (unit: μMm).

Based on this reaction model, a steady state diagram was computed using the software COPASI, showing PIP2 and corresponding PIP3 concentrations in the membrane at steady state for a given PTEN bulk concentration, see Fig 7.5A. This steady

state diagram corresponds to the experiments shown in Figs 7.2 and 7.4, where hysteresis was found for varying PTEN concentrations. Within the grey zone (Fig 7.5A), for each PTEN concentration, two stable states (filled symbols) are separated by an unstable state (open symbols). This grey zone indicates where hysteresis occurs, since a line of stable steady states extents from lowest (or highest) PTEN concentration to the right (or left) boundary of the grey box. Outside of the grey zone, only a single steady state is found. This variation of steady state stability depending on PTEN concentration is further illustrated in Fig 7.5B, where we have plotted PIP3 reaction velocities for three fixed PTEN concentrations. For a PTEN concentration to the left of the grey box in Fig 7.5A, the reaction velocity becomes zero at a high PIP3 concentration. This steady state is stable, i.e. local perturbations in PIP3 concentration decay (see arrows in Fig 7.5Bi). For an intermediate PTEN concentration, three steady states are found (Fig 7.5Bii). At the intermediate PIP3 concentration, local fluctuations become amplified, rendering that steady state instable. At a PTEN concentration to the right of the grey box, a single stable steady state is found at low PIP3 concentration in the membrane (Fig 7.5Biii). Consistent with this discussion, linear steady stability analysis of the steady states shown in Fig 7.5A yields Eigenvalues of the reduced Jacobian matrix the real components of which are found to be exclusively negative outside of the grey box (details described in Chapter 7.5). The same is true for two of the steady states for a given PTEN concentration within the grey box, whereas for the middle steady state a positive Eigenvalue is found, consistent with an unstable condition.

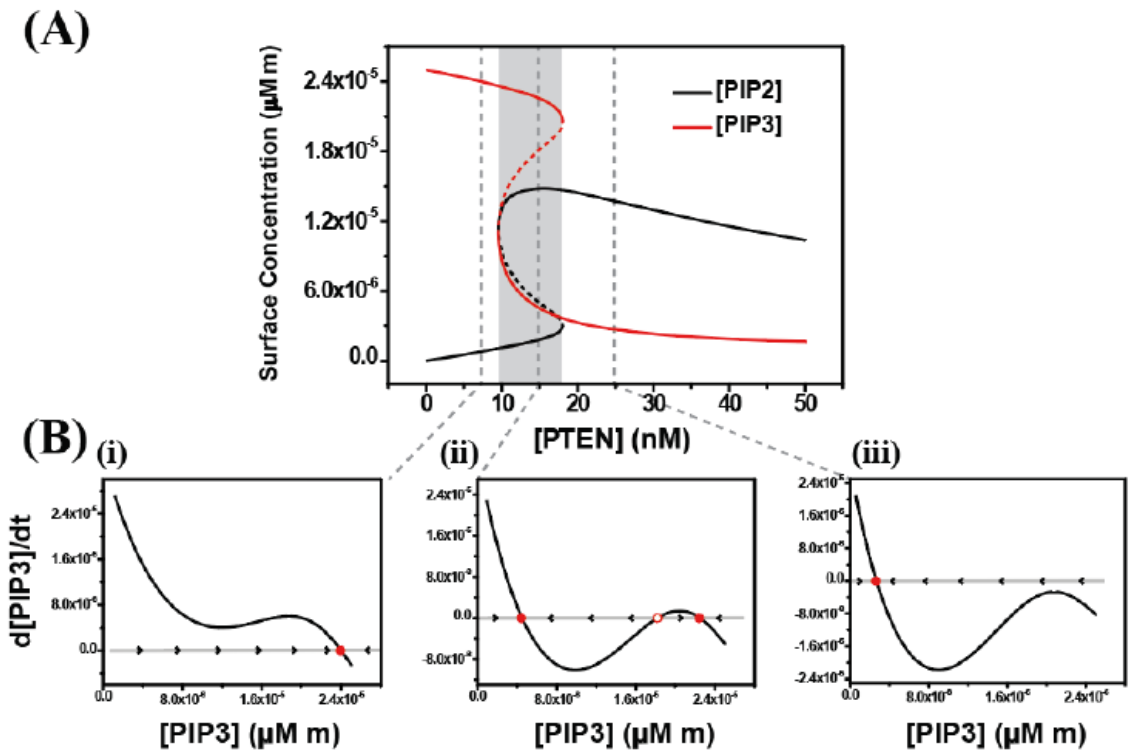

Fig 7.5. Simulation of bistability of PIP2-PIP3 phosphorylation-dephosphorylation cycle.

(A). Change of steady-state of phosphoinositides with PTEN concentration. The stable steady-states of PIP3 (red solid. lines), unstable steady-states of PIP3 (red dashed line), stable steady-states of PIP2 (black solid line), and unstable steady-states of PIP2 (black dashed line) are shown.

(B). The velocity plot of change of PIP3 (d[PIP3]/dt) against amount of PIP3 ([PIP3]) at different PTEN concentration. The fixed points are labeled with ● when the steady-state is stable, and the points are labeled with ○ when the steady-state is unstable. (i). There is one stable steady-state ([PIP3] = $2.4*10^{-5}$ μMm) at [PTEN] = 7.5 nM. (ii) There are two stable steady-states ([PIP3] = $4.5*10^{-6}$ μMm and $2.2*10^{-5}$ μMm) and one unstable steady-

state ([PIP3] = $1.8*10^{-5}$ μMm) at [PTEN] = 15 nM. (iii) There is one stable steady-state ([PIP3] = $2.7*10^{-6}$ μMm) at [PTEN] = 25 nM.

Parameter values were chosen as follows: $k_{cat}^{PTEN} = 11 s^{-1}$ [*], $k_a^{PTEN} = 1.7*10^{-3} m/s$ [*], $k_d^{PTEN} = 0.7 s^{-1}$ [*], $k_M^{PTEN} = 2*10^{-3} \mu Mm$ [*], $k_{cat}^{PTEN-PIP2} = 19 s^{-1}$ [*], $K_{PTEN,PIP2} = 7.9*10^{-6} \mu Mm$ [*], $k_M^{PTEN-PIP2} = 2.3*10^{-5} \mu Mm$ [*], $V_{\max}^{PI3K} = 7.5*10^{-5} \mu Mms^{-1}$ (arbitrarily chosen), $k_M^{PI3K} = 2.5*10^{-5} \mu Mm$ [**], $K_D^{PTEN-PIP2} = \frac{k_d^{PTEN-PIP@}}{k_a^{PTEN-PIP2}} = 0.02 \mu M$ [***], $K_D^{Grp1} = \frac{k_d^{Grp1}}{k_a^{Grp1}} = 0.11 \mu M$ [****], $K_D^{PLC} = \frac{k_d^{PLC}}{k_a^{PLC}} = 0.375 \mu M$ [****]. Steady state calculations were performed with COPASI (Fig 7.5A) and MATLAB (Fig 7.5B). [*] Values are from our previous work (Chapter 4, [78]); [**] K_M^{PI3K} was determined in this work (Fig 7.1D; K_m is 1.06% PIP2, which corresponds to $2.5*10^{-5}$ μMm); [***] The $K_D^{PTEN-PIP2}$ value is comparable to the value determined by Shenoy et al. (50 nM, [143]), [****] K_D^{Grp1} and K_D^{PLC} were determined in this work (Fig 3.2A). Enzyme and sensor concentrations: [Grp1] = 110 nM, [PLC] = 375 nM.

We note that the steady state diagram (Fig 7.5A) was computed based on parameters comparable to those measured experimentally (if known). Fig 7.5A is consistent with the notion that the strength of the PIP2 mediated feedback, which we evaluated previously [78], is sufficient to produce a bistable region within the variable space. Quantitative agreement between this theoretical prediction and our experimentally obtained hysteresis diagram (Fig 7.2C) is not expected for several reasons: a) kinetic parameters determined in Ref. [78] were obtained using a slightly different lipid composition (lower PI lipid content), b) the catalytic rate of PI3K is not yet available for our membrane system, and

c) the rate constants of PLC binding/unbinding to the membrane are not available (determination of these unknowns is in progress but is beyond the scope of the current contribution). Nevertheless, the qualitative agreement between Fig 7.5A and 7.2C is encouraging and is consistent with the notion of steady state hysteresis mediated by feedback through an autocatalysis mechanism with PTEN. We note on passing that the time to reach the steady state, calculated with the parameter set used to obtain Fig 7.5, is below 10 min for all conditions considered in the experimental Figs 7.2-7.4, providing additional confidence that this incubation time was sufficient in experiments to reach steady state conditions.

7.4 Biosensor-Mediated PTEN / PI3K Toggle Switch

The simulations presented above plausibly support the notion of deterministic bistability in the PTEN/PI3K reaction cycle. However, the model does not explain why experimental histograms of bead compositions (Figs 7.2-7.4) can be bimodal. Several different mechanisms might contribute to this behavior. One contribution might result from uneven distributions of biosensors on different beads (see Figs 3.2C). To illustrate how biosensor content of BSMs can sensitively toggle the bimodal composition switch, we simulated steady states based on both the model, and the parameters used for Fig 7.5, and titrated Grp1 concentration while holding both enzyme as well as PLC concentrations fixed. As Fig 7.6A shows, this type of titration produces a hysteresis loop, consistent with the notion of bistable switching through sequestration of PIP3. Similarly, titration of PLC for fixed enzyme concentrations and fixed Grp1 also produces a hysteresis loop (Fig

7.6B) consistent with bistable switching through sequestration of PIP2. Fig 7.6 thus implies that for specific enzyme concentrations, minute differences in BSM biosensor content (near the bifurcations from single to multiple steady states) can have substantial effects on PIP composition through toggling of the PTEN/PI3K steady state switch. This effect is reminiscent of that of substrate sequestration through competing enzymes in leading to ultrasensitivity and bistability [144]. A second mechanism, of course, could be afforded through uneven distributions of enzymes among BSMs. While verification of that hypothesis would require fluorescence labeling of enzymes, Fig. 7.5 clearly illustrates how fluctuations in BSM enzyme content can have substantial effects on PIP composition close to bifurcations from single to multiple steady states. Figs 7.5 and 7.6 then suggest that fluctuations of enzyme and biosensor concentrations content of BSMs could mutually amplify their effects on PIP content of BSMs in the bistable regime, consistent with the observation of bimodal PIP composition histograms. Such statistical effects of enzyme and biosensor binding to BSMs might be further amplified through potential cooperative binding effects of biosensors and / or enzymes [145], as well as through fluctuations in enzyme activities on the BSMs [146]. Consistent with this discussion, positive feedback in general is known to amplify noise in numerous biological signaling scenarios [147-149].

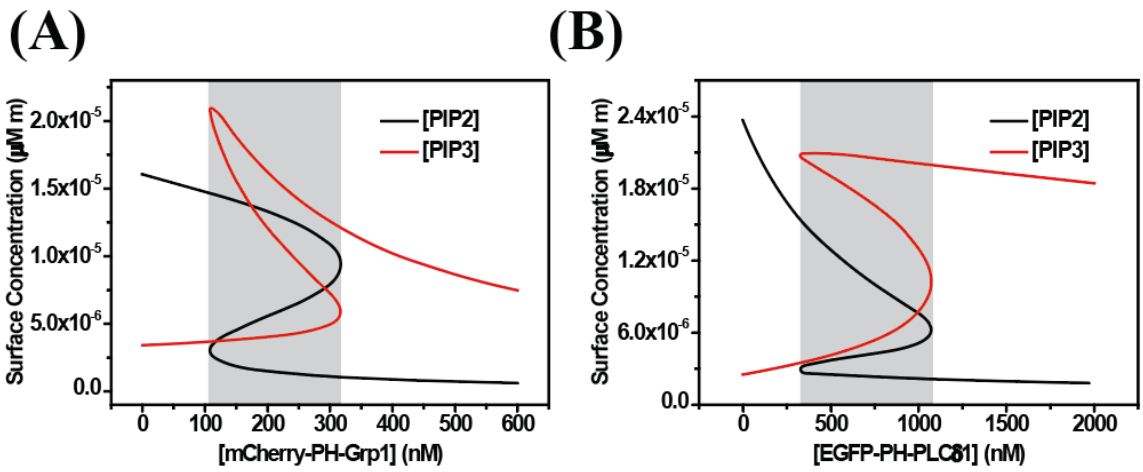

Fig 7.6. Simulation of biosensor-mediated toggling of PTEN/PI3K switch. Change of steady-state concentrations of phosphoinositides with mCherry-PH-Grp1 (A) and EGFP-PH-PLCδ1 (B) concentration, respectively. The steady-states of PIP2 (-, black) and PIP3 (-, red) are shown in both figures. The bistable region of phosphoinositides, which has two stable steady-states and one unstable steady-state, is labeled in grey. The rest of the regions only have one stable steady-state. Both steady state calculations were performed with COPASI. All parameters are the same as in figure 7.5. Enzyme and sensor concentrations: [PTEN] = 18 nM, [EGFP-PH-PLCδ1] = 375 nM in (A), [mCherry-PH-Grp1] = 110 nM in (B).

Supplementary Figures

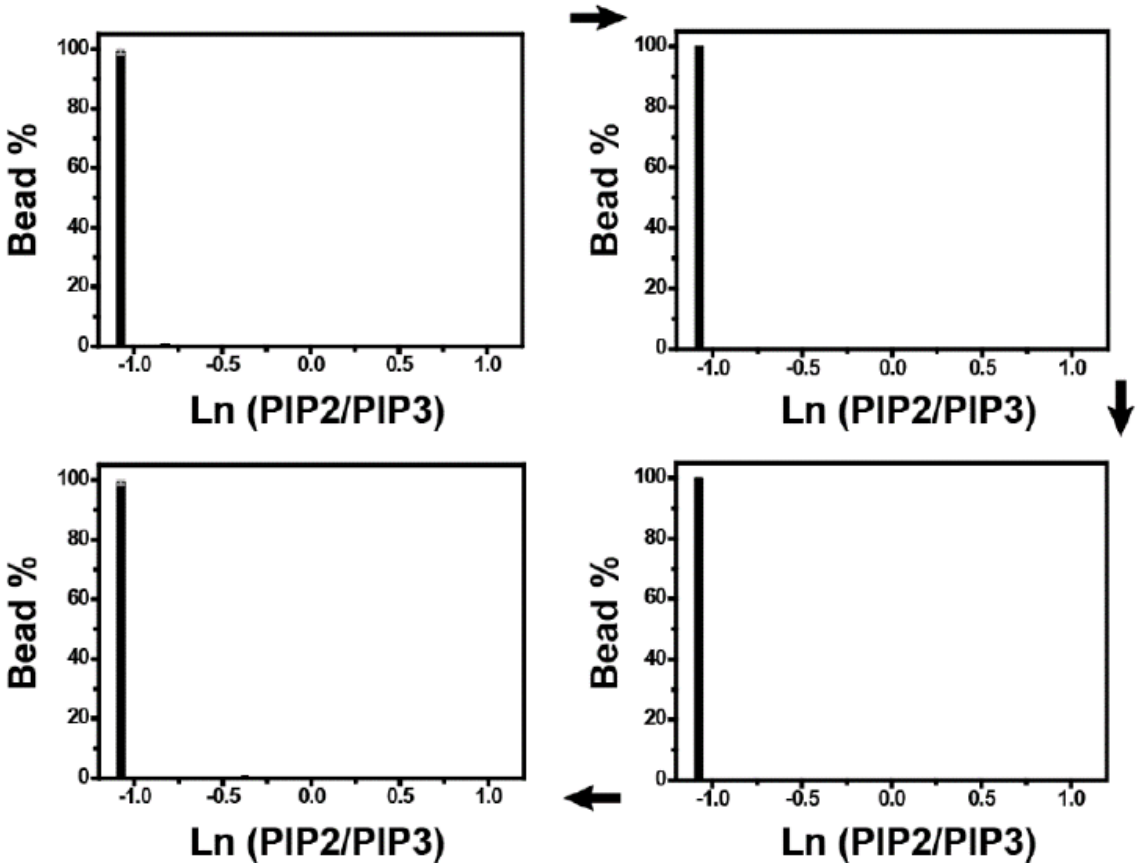

Fig S7.1 Mock (i.e. enzyme-free) titration involving BSM samples. The composition for this experiment was 2% PIP3 / 5% DOPS / DOPC / 0.2% Naphthopyrene. The same titration procedures (in the sequence indicated by the arrows) as shown in Fig 7.2 were followed but only involving sensor proteins (no enzymes). The resulting histograms did not significantly change appearance.

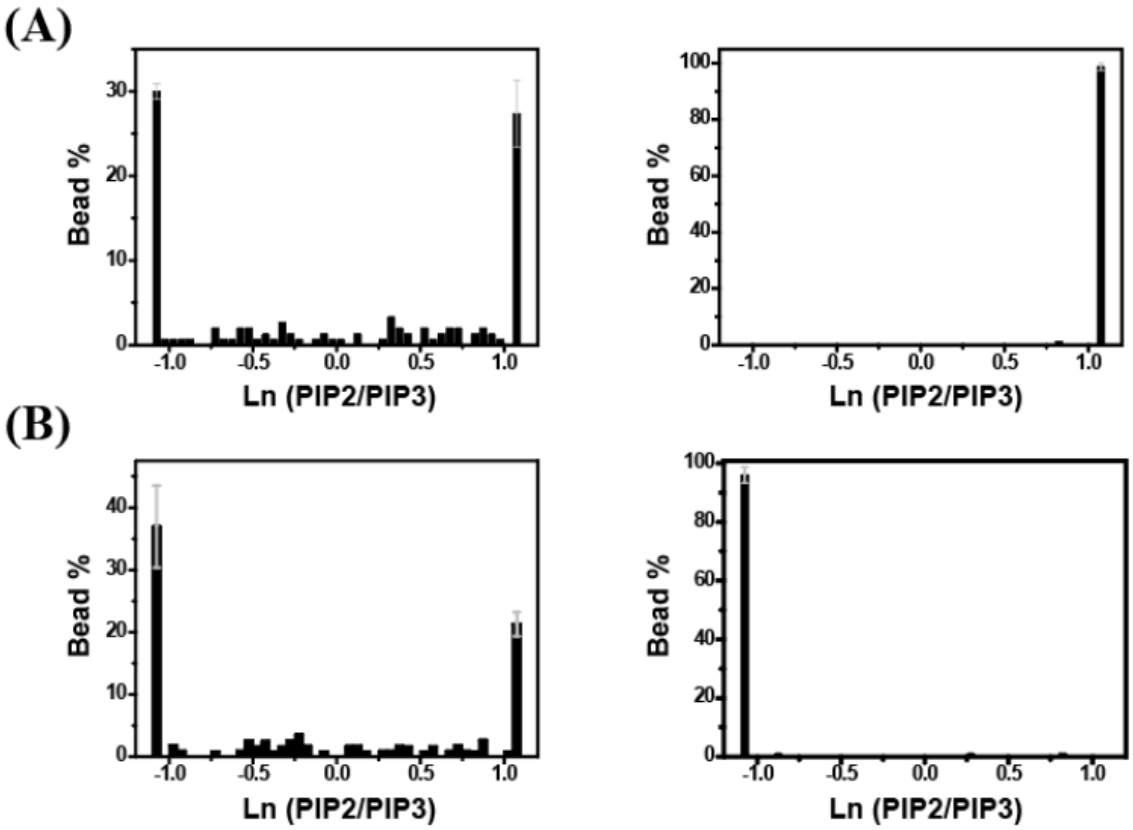

Fig S7.2 Pharmacological inhibition of enzymes supports the notion of steady state conditions for BSM reaction systems showing bimodality. (A) PIP2-rich BSMs were first mixed with both enzymes and both biosensors and were converted into a state characterized by the presence of both PIP2-rich and PIP3-rich BSMs (left, also see Fig 7.4A, middle). The PI3K inhibitor wortmannin was then added to the reaction (final concentration 700 nM), incubated with the reaction system for 10 min), and the system was observed to return to a PIP2-rich state (right). The initial BSM composition used here was 2% PIP2 / 5% DOPS / DOPC / 0.2% Naphthopyrene. (B) PIP3-rich BSMs were first mixed with both enzymes and both biosensors and were converted into a PIP2-rich and PIP3-rich mixed state (left). The PTEN inhibitor VO-OHpic was then added to the reaction system (final concentration of 15 μM, incubated with the reaction system for 20

min) and the system was observed to be converted to a PIP3-rich state (right). The initial BSM composition used here was 2% PIP2 / 5% DOPS / DOPC / 0.2% Naphthopyrene.

7.5 Stability Analysis of Steady-State

From above model simulation we can determine how steady-state change with the amount of PTEN (Fig 7A) and the biosensors (Fig 8), but how do we know whether the steady-state calculated is stable or not? Here we'd like to adapt the stability analysis method described in Strogatz book [150], then use it to analyze the stability of steady-state. The stability analysis method is described in Chapter 1.11.

In the current COPASI file, the bulk concentrations of enzyme and sensor concentrations are fixed: PTEN, Grp1, PLC. We have five species change with time: Grp1-PIP3, PIP2, PIP3, PLC-PIP2, and PTEN-PIP2. In the simulation file, we have five corresponding differential equations and one constraint (total PIs concentration is conserved). So we have four independent variables in our system, and it matches the number of eigenvalues of the Jacobian matrix. First we performed the stability analysis in COPASI at different PTEN concentrations: 7.5, 15, and 25 nM (Table 7.1). At 7.5 nM, all four eigenvalues are negative, which suggest that this steady-state is a *stable fixed point*. At 25 nM, two eigenvalues are complex numbers but all real parts of eigenvalues are negative, which suggest this steady-state is a *stable spiral*. We got three steady-states at 15 nM: the first one belongs to a *stable fixed point* (with all negative eigenvalues), the second one belongs to a *saddle point* (with one positive and three negative eigenvalues),

and the third one belongs to a *stable spiral* (with the complex eigenvalues and all the real parts are negative).

Table 7.1. Stability analysis of dynamic system at specific PTEN concentration (corresponds to Fig 7.5A)

PTEN (nM)	[PIP2]eq (μM m)	[PIP3]eq (μM m)	λ_1	λ_2	λ_3	λ_4
7.5	$8.30*10^{-7}$	$2.40*10^{-5}$	-0.097	-0.214	-0.294	-3.059
15	$1.83*10^{-6}$	$2.25*10^{-5}$	-0.095	-0.183	-0.281	-2.523
	$4.95*10^{-6}$	$1.2*10^{-5}$	0.41	-0.102	-0.245	-1.019
	$1.49*10^{-5}$	$4.50*10^{-6}$	- 0.115 - 0.011i	- 0.115 + 0.011i	-0.484	-5.853
25	$1.37*10^{-5}$	$2.70*10^{-6}$	- 0.116 - 0.006i	- 0.116 + 0.006i	-0.674	-9.366

The result of above stability analysis is in consistent with the velocity plot result in Fig 7.5B.

Table 7.2. Stability analysis of dynamic system at specific Grp1 concentration (corresponds to Fig 7.6A)

Grp1 (nM)	[PIP2]eq (μM m)	[PIP3]eq (μM m)	λ_1	λ_2	λ_3	λ_4
70	$1.52*10^{-5}$	$3.57*10^{-6}$	-0.114	-0.127	-0.542	-7.481
200	$1.33*10^{-5}$	$4.03*10^{-6}$	- 0.105 - 0.015i	- 0.105 + 0.015i	-0.559	-6.157
	$5.54*10^{-6}$	$1.20*10^{-5}$	0.338	-0.102	-0.390	-1.163
	$1.49*10^{-6}$	$1.62*10^{-5}$	-0.095	-0.209	-0.360	-2.865
450	$7.84*10^{-7}$	$9.37*10^{-6}$	- 0.096	- 0.256	-0.568	-3.375

Table 7.3. Stability analysis of dynamic system at specific PLCδ1 concentration (corresponds to Fig 7.6B)

PLCδ1 (nM)	[PIP2]eq (μM m)	[PIP3]eq (μM m)	λ_1	λ_2	λ_3	λ_4
150	$1.92*10^{-5}$	$2.95*10^{-6}$	- 0.108 - 0.009i	- 0.108 + 0.009i	-0.543	-10.462
750	$1.00*10^{-5}$	$5.41*10^{-6}$	-0.120	-0.128	-0.522	-3.569
	$4.30*10^{-6}$	$1.66*10^{-5}$	0.235	-0.105	-0.250	-1.108
	$2.31*10^{-6}$	$2.05*10^{-5}$	-0.084	-0.164	-0.272	-2.189
1500	$1.96*10^{-6}$	$1.92*10^{-5}$	-0.085	-0.206	-0.284	-2.702

Chap 8 Future Outlooks

8.1 Testing an Intermediate-Depletion Mechanism for Surface Wave Generation

Chemotaxis is a process of directional migration of the cell towards a chemoattractant, including the migration of neutrophils to a wound [151] and leukocytes to the site of infections [152]. During chemotaxis in *Dictyostelium*, PI3K is localized at the leading edge of the cell and PTEN is localized at the rear of the cell [43, 153, 154]. Both enzymes distribute reciprocally on the membrane, and their proper localization is important for chemotaxis. On the other hand, the reciprocal distribution of PIP3 and PTEN was reported to occur spontaneously without chemoattractant [118]. The spatial and temporal evolution of the PTEN-rich and PIP3-rich domains along the membrane was also observed. Many theoretical models have been proposed to explain it, like the "local excitation / global inhibition model" [155] and "intermediate depletion model" [156] among others. However, no phosphatidylinositol polarization and relaxation oscillation has ever been reconstructed in model membrane systems based on the proposed models. The detailed mechanism of chemoattractant-induced and self-organized cell polarization is still under debate.

To test the intermediate-depletion model and detect potential spatial distribution of PIP2-rich and PIP3-rich domains on lipid membranes, PDMS channels with supported lipid bilayers provide good platforms. PDMS channel-lipid bilayer systems not only allow protein and enzyme exchange easily with flow, but also deplete target proteins from solution due to the large surface to volume ratio. In addition, the planar bilayer platform can be combined with surface sensitive detection methods, like TIRF, to allow

for observation of the potential spatial and temporal changes of phosphoinositides with PTEN / PI3K.

In Chapters 5 and 6, we characterized forced PH-Grp1 oscillations on lipid membranes by injecting PTEN and PI3K sequentially into the PDMS channel. We also showed that changes of PIP3 and PIP2 concentrations on lipid membranes can be detected with mCherry-PH-Grp1 and EGFP-PH-PLCδ1, respectively. By combining these two fluorescent sensor proteins with the PDMS channel-lipid bilayer system, we could systematically vary PTEN / PI3K ratios and observe how steady-states of phosphoinositides change spatially and temporally on model lipid membranes.

8.2 Characterizing Other Potential Feedback Loops in the PTEN / PI3K System

In Chapter 7, we characterized the hysteresis cycle and bistable behavior of PIP2 / PIP3 on lipid membranes with PTEN / PI3K. Based on the simulation, we proposed that a positive feedback loop of PTEN-PIP2 was critical in establishing this bistability, which disappeared when we removed the feedback term. Additional feedback mechanisms, however, may exist for this phosphorylation-dephosphorylation cycle. Mutual inhibition between PIP3 and PTEN binding, for example, has recently been observed in cells [157], but it is not yet clear if this mechanism would be at work in our *in-vitro* system. In the future, we can test this mechanism by characterizing binding of PTEN on lipid bilayers with different amounts of PIP3. To achieve this goal, the first step would be to label PTEN such as with fluorescent proteins for detection. Next, we would mutate PTEN to

abolish its phosphatase activity and to avoid PIP3 hydrolysis during the PTEN binding study. However, a point mutation at a catalytic site may not only affect phosphatase activity but also binding ability. Cysteine 124, which is essential for PTEN phosphatase activity, was reported to enhance the membrane-binding ability of PTEN when mutated to serine both *in vivo* and *in vitro* [16, 111, 158]. R130G, another catalytic site mutation, was reported not to increase membrane association of PTEN in *Dictyostelium* cells. $PTEN_{R130G}$ may therefore be a good candidate to study this association regulation.

The N-terminal SH3-BH region of p85α is shown to interact with PTEN in the cell, leading to increased phosphatase activity of PTEN [159] and providing additional feedback for regulation. This region is absent in our niSH2 truncate of p85α. It would be very interesting to examine how this direct interaction of this p85 subunit with PTEN affects the bistable behavior of PIP2 / PIP3 by using full length PI3K in the future.

8.3 Detecting Potential Lipid Bilayer Patches on Bead-Supported Lipid Bilayers with Super-Resolution Methods

In Chapter 7, we observed that though the majority of PIP2 / PIP3 population on BSMs are either PIP2-rich or PIP3-rich, the remaining populations show wide phosphoinositide distributions. We hypothesized that the origin of this heterogeneity is caused by the occurrence of incompletely fused lipid bilayers on BSMs. Under bistable conditions, different phosphoinositide compositions occur on different lipid membrane patches, which are below the optical resolution limit.

To test this hypothesis, super-resolution fluorescence microscopy can be used to detect these potential membrane patches. Several microscopy methods have been developed over the past several years to achieve super-resolution detection (resolution beyond the diffraction limit), including stimulated emission depletion microscopy (STED), photoactivated localization microscopy (PALM), and stochastic optical reconstruction microscopy (STORM) [160]. STED is based on laser scanning confocal microscopy with two laser beams at different wavelengths. One laser beam with shorter wavelength is responsible for fluorophore excitation, while the second laser with longer wavelength, donut-shaped beam is responsible for stimulated emission, reducing the effective point spread function (PSF) to achieve super-resolution.

PALM was first achieved using photoconvertible fluorescent proteins, in which the emission wavelength can be switched to another wavelength region through optical conversion. Super-resolution can be achieved when only a small portion of fluorophores is photo-converted. Since 2002, numerous photoactivatable and photoswitchable fluorescent proteins have been developed and can be applied to super-resolution imaging [161]. Photoactivatable fluorescent proteins can be activated from a dark state to a fluorescent state, while photoswitchable fluorescent proteins can be switched on and off at distinct wavelength. STORM, sharing similar principles with PALM, was originally carried out using a Cy3-Cy5 dye system, where Cy5 is a photoswitchable dye and Cy3 is a dye to facilitate the switching process of Cy5.

In summary, we can use either STED or PALM microscopy to characterize our system. For the STED method, we can directly use a commercially available STED

super-resolution microscope for observation. For the PALM method, we would first need to fuse either photoconvertible or photoactivatable fluorescent proteins to the lipid sensors, then detect with PALM imaging.

APPENDIX

In the Appendix, we include four MATLAB codes for data fitting and analysis:

(i). Association and dissociation kinetics of ligand / protein to the membrane.

(ii). PTEN-mediated PIP3 hydrolysis at various PIP2 and YFP-PH-Grp1 concentration.

(iii). Analyze fluorescence intensity around BSMs.

(iv). Simulate how rate of PIP3 hydrolysis change with different PIP3 content in the membrane

A. Association and Dissociation Kinetics

Goal: The files are used to globally fit association and dissociation kinetics of ligand to the membrane. Two MATLAB files are included. The first one is "exe.m" file, which includes fitting parameters (with initial values), input file names, and output settings. The second file is "proteinBinding.m" file, which includes differential equations of fitting model, cost function, and cost function minimization method.

Instructions

1. Open the "exe.m" file → change file name
2. Click "run" directly
3. The analysis result will show

(i). A figure with y axis: Grp1 density (μMm); x axis: time (s)

(ii). Four optimized fitting parameters ratios (optP), which corresponds to k_a, k_d, k_{tr}, and h, respectively, will show in command window. The final optimized values will be these optimized ratios (optP) times each initial values (realP0), respectively.

Code 1: exe.m

```
clc
clear
close all
set(0, 'defaultaxesFontSize', 20);
set(0, 'defaulttextFontSize', 20);

global P0 realP0 Ka0 Kd0 Ktr0 h0 PIP30

%% Initial Value Setting
%% NEVER set any two guesses to be the same in P0
Ka0= 2.43 % s^{-1} uM^{-1}
Kd0= 0.31 % s^{-1}
Ktr0= 0.3*10^-6 % m/s (at linear flow rate: 1 cm/s)
h0= 1*10^-5 % m

PIP30= 4.75*10^-6 ; % uM m ; 2850 molecule/um^2
%%
dirName=  '';

fileName1= '75nM_Ass.txt';
fileName2= '150nM_Ass.txt';
```

```
fileName3= '300nM_Ass.txt';

fileName4= '800nM_Ass.txt';

fileName5= '75nM_Diss.txt';

fileName6= '150nM_Diss.txt';

fileName7= '300nM_Diss.txt';

fileName8= '800nM_Diss.txt';


filePath= {fileName1 fileName2 fileName3 fileName4 fileName5 fileName6 fileName7
fileName8}


realP0= [Ka0; Kd0; Ktr0; h0];

P0= ones(size(realP0));


tic

[optP,err]= proteinBinding(filePath)

time= toc;

ss= sprintf('%d seconds\noptP vs P0:', time);

disp(ss)

disp([optP P0])

disp([optP.* realP0 P0.* realP0])
```

Code 2: proteinBinding.m

```
function [optP,err]= proteinBinding(fileName)

set(0, 'defaultaxesFontSize', 20);

set(0, 'defaulttextFontSize', 20);
```

```
%% P0= [];
maxIter= 5000;
global P0
global colTime colInt vExp tSpan data numfiles vFit vT N

%%
colTime= [1];
colInt= [2];
numfiles = 8;
% Initialize cell arrays of vExp and tSpan
vExp = cell(1,numfiles);
tSpan = cell(1,numfiles);
N = cell(1,numfiles);

% Load data sequentially into cell arrays
for j = 1:numfiles
   data = load(char(fileName(j)));
   vExp{j} = data(:, colInt);
   tSpan{j} = data(:, colTime);
   [N{j} M] = size(data(:, colInt));
   j=j+1;
end

%% use patternsearch
% [nKa, nKd, nKtr, nh] = P0.*realP0
            %realP0: initial guess (constant)
            %P0: the coefficient (Vary in each fitting iteration)
```

```
            % Varying P0 to minimize costFunc
options = optimset('MaxIter', maxIter,'Display','iter', 'MaxFunEvals', 40000);
conA=[];
conB=[];
conAeq=[];
conBeq=[];
conlb= 0*P0;
conub= 10*P0;
connonlcon=[];
[optP err]= patternsearch(@(Pn)costFunc(Pn,0), P0, conA, conB,
conAeq,conBeq,conlb,conub,connonlcon,options);
%% given optP, solve solFunc again...
%% plot Int

for m = 1:numfiles
    plot(tSpan{m}, vExp{m}, 'xb', vT{m}, vFit{m},'g', 'LineWidth', 2, 'MarkerSize', 12);
    hold on
    m=m+1;
end
   legend('Exp', 'Fit', 'Location', 'best');
   xlabel('t (s)');
   ylabel('Grp1 Density (uM m)');
end

% costFunc: the error function between experimental data and fitting value
% Fitting value is get by solFunc(optP,y0,tSpan)
function err= costFunc(Pn,costcase)
```

```
global realP0 PIP30 vExp tSpan numfiles vFit vT


Grp10 = {0.075 0.15 0.3 0.8 0 0 0 0}; % Initial Grp1 concentration in the outer compartment ; Put element into cell array

CT = [0 0 0 0 0.075 0.15 0.3 0.8]; % Initial Grp1 concentration in the inner compartment


    par = Pn.*realP0; % par = [nKa, nKd, nKtr, nh];

    nKeq= par(1)/par(2); % nKeq= nKa/nKd;

    nBint= (nKeq*CT*PIP30)./(1+nKeq*CT); % nBint = [nBint(1) nBint(2) ...nBint(8)]

    y0 = [CT; nBint];


    vFit = cell(1,numfiles); %initialize cell arrays

    vT = cell(1,numfiles);


  % Take different y0 and Grp10 into solFunc, respectively

 for j=1:numfiles

    [vT_s vFit_s]= solFunc(Pn,y0(:,j),tSpan{j}, Grp10{j}, par);

    vFit{j} = vFit_s(:,2); % vFit_s(:,2): Grp1-PIP3

    vT{j} = vT_s;

    vErr= vFit{j}- vExp{j}; % Adding weighting factor (using average fluorescence intensity)

    err(j)=norm(vErr);


    j=j+1;


    err = sum(err); % sum each element of err(:,i)

 end
```

```
end

 %solFunc: Using ode solver to solve diff. eqn.
function [vT vFit]= solFunc(Pn,y0,tSpan, Grp10, par)

odeoption = [];
Tim=linspace(tSpan(1),tSpan(end),200);
[vT vFit]= ode23s(@diffFunc, Tim, y0, odeoption, Grp10, par);
vFit= interp1(vT, vFit, tSpan);
vT= tSpan;
end

%Diff Eqn.:       %dydt(1)= (nKtr/nh)*(Grp10-y(1)) - nKa*y(1)*((PIP30-y(2))/nh) +
nKd*(y(2)/nh);
              %dydt(2)= nKa*y(1)*(PIP30-y(2)) - nKd*y(2);
  function dydt=diffFunc(t, y, Grp10, par)
      global PIP30
      dydt = zeros(2,1);
      dydt(1)= (par(3)/par(4))*(Grp10-y(1)) - par(1)*y(1)*((PIP30-y(2))/par(4)) +
par(2)*(y(2)/par(4));
      dydt(2)= par(1)*y(1)*(PIP30-y(2)) - par(2)*y(2);
  end
```

B. PTEN Kinetics

Goal: The files are used to globally fit PTEN-mediated PIP3 hydrolysis kinetics. Two files are included, the first file is “exe.m” file, and the second one is “PTEN.m” file.

Instructions

4. Open the “exe.m” file → change file name
5. Click "run" directly
6. The analysis result will show

(i). A figure with y axis: PIP3 concentration (μMm); x axis: time (s)

(ii). Ten optimized fitting parameters ratios (optP), which corresponds to k_{cat}^{PTEN}, k_{a}^{PTEN}, k_{d}^{PTEN}, $k_{a}^{PTEN-PIP2}$, $k_{d}^{PTEN-PIP2}$, $k_{cat}^{PTEN-PIP2}$, k_{M}^{PTEN}, $k_{M}^{PTEN-PIP2}$, $k_{PTEN.PIP2}$, and n, respectively, will show in command window. The final optimized values will be these optimized ratios (optP) times each initial values (realP0), respectively.

Code 1: exe.m file

```
clc
clear
close all
set(0, 'defaultaxesFontSize', 20);
set(0, 'defaulttextFontSize', 20);

global P0 realP0 k4 k5 ktr h k30 k60 k70 k80 k90 Kpten0 PIP30 PTEN0 PTENB k100
t10 Kcat0 Kpten_10

PIP30= 4.75*10^-6 %uM m  ; it corresponds to 2.85*10^3 #/um^2;
PTEN0= 0.1; % uM
PTENB= PTEN0;

%% Initial Values
```

```
%% NEVER set any two guesses to be the same in P0
  % Fix kon, koff, ktr, h based on Grp1 Ass. & Diss experiment
k4= 1.68  % s-1 uM-1 (Grp1 association...from my Exp)
k5= 0.16  % s-1 (Grp1 dissociation...from my Exp.)
ktr= 1.5*10^-6 % m/s (from my Exp. on Grp1 Ass. & Diss.)
h= 1.783*10^-5  % m ; (from my Exp. on Grp1 Ass. & Diss.)

k30= 10;          % k3=PTEN kcat
Kpten0= 0.5*3.8*10^-3;  % Kpten=Michaelis constant for PTEN

k60= 1*10^-3;       % k6=PTEN association constant to membrane
k70= 0.3;         % k7=PTEN dissociation constant from membrane
k80= 200;      % k8=PTEN,PIP2 association constant
k90= 0.3;      % k9=PTEN,PIP2 dissociation constant

k100= 16.7;       % k10=PTEN-PIP2 kcat
t10=2;           % t1=n ...Hill coefficient
Kcat0=7.9*10^-6;         % Kcat=Kpten,pip2
Kpten_10=2.3*10^-5;   % Kpten_1=Michaelis constant for PTEN-PIP2

%% Load Data & Define P0
dirName=  '';
fileName1= '0.2%PIP3.txt';
fileName2= '0.2%PIP3+0.1%PIP2.txt';
fileName3= '0.2%PIP3+0.15%PIP2.txt';
fileName4= '0.2%PIP3+0.2%PIP2.txt';
fileName5= '0.2%PIP3+0.3%PIP2.txt';
```

```
fileName6= '0.2%PIP3+0.4%PIP2.txt';

fileName7= '0.2%PIP3+0.2%PIP2_100nMGrp1.txt';

fileName8= '0.2%PIP3+0.2%PIP2_150nMGrp1.txt';

fileName9= '0.2%PIP3+0.2%PIP2_600nMGrp1.txt';


filePath= {fileName1 fileName2 fileName3 fileName4 fileName5 fileName6 fileName7
fileName8 fileName9};


realP0= [k30, Kpten0, k60, k70, k80, k90, k100, t10, Kcat0, Kpten_10];

P0= ones(size(realP0));


tic

[optP,err]= PTEN(filePath)

time= toc;

ss= sprintf('%d seconds\noptP vs P0:', time);

disp(ss)

disp([optP P0])

disp([optP.* realP0 P0.* realP0])
```

Code 2: PTEN.m file

```
function [optP,err]= PTEN(fileName)

set(0, 'defaultaxesFontSize', 20);

set(0, 'defaulttextFontSize', 20);


maxIter= 5000;
```

```
global P0
global data colTime colInt vExp tSpan numfiles vT vFit

colTime = [1];
colInt = [2];
numfiles = 9;

%% Define vExp and tSpan as cell array
vExp = cell(1:numfiles);
tSpan = cell(1:numfiles);

%% Load experimental data sequentially
   i=1;
for j = 1:numfiles
   data = load(char(fileName(j)));
   vExp{i} = data(:,colInt);
   tSpan{i} = data(:,colTime);
   i=i+1;
end
%% Patternsearch
options = optimset('MaxIter', maxIter,'Display','iter','MaxFunEvals', 60000);
conA=[];
conB=[];
conAeq=[];
conBeq=[];
conlb= [0, 0, 0, 0, 0, 0, 0, 0, 0, 0];
conub= 5*P0;
```

```
connonlcon=[];

[optP err]= patternsearch(@costFunc, P0, conA, conB,
conAeq,conBeq,conlb,conub,connonlcon,options);


%% given optP, solve solFunc again

%% plot Int


   k=1;

for m = 1:numfiles

   plot(tSpan{m}, vExp{m}, 'xb', vT{m}, vFit{m},'g', 'LineWidth', 2, 'MarkerSize', 12);

   hold on

   k=k+1;

end

  legend('Int_{exp}', 'Int_{fit}', 'Location', 'best');

  xlabel('t/ s');

  ylabel('Int');


end


function err= costFunc(Pn)

  global P0 realP0 PIP30 vFit vT vExp numfiles tSpan k4 k5

  PIP20 = [0*PIP30, 0.5*PIP30, 0.75*PIP30, 1*PIP30, 1.5*PIP30, 2*PIP30, 1*PIP30,
1*PIP30, 1*PIP30];

  Grp1B = [0.3 0.3 0.3 0.3 0.3 0.3 0.1 0.15 0.6]; % Grp1 concentration in the outer
compartment = Initial Grp1 in inner comp.


  par = Pn.*realP0; % par = [k3, Kpten, k6, k7, k8, k9, k10, t1, Kcat, Kpten_1]

  nKeq= k4/k5; % nKeq= nKa/nKd;
```

```
  nBint = (nKeq*Grp1B*PIP30)./(1+nKeq*Grp1B); %[Grp1-PIP3]int


  % Set initial value: y0 = [Grp1-PIP3 PIP3 PTENm PTEN-PIP2 PTEN_compsol PIP2
Grp1_compsol]
       [PIP3] = PIP30 - nBint;
       Z = zeros(1,numfiles); % Z = PTENm = PTEN-PIP2 = PTEN_compsol =0 ...initial
    y0 = [nBint; PIP3; Z; Z; Z; PIP20; Grp1B];


  vFit = cell(1:numfiles);
  vT = cell(1:numfiles);
  i=1;
  for j=1:numfiles
     [vT_s vFit_s]=solFunc(Pn, tSpan{j}, y0(:,j), Grp1B(:,j), par);
     vFit{i} = vFit_s(:,1); % vFit_s(:,1) = Grp1-PIP3
     vT{i} = vT_s;
     vErr = vFit{i}-vExp{i};
     err(:,i) = norm(vErr);
     i=i+1;
  end
     err = sum(err);
end


function [vT vFit]= solFunc(Pn, tSpan, y0, Grp1B, par)
odeoption = [];
Tim=linspace(tSpan(1),tSpan(end),200);
[vT vFit]= ode23s(@diffFunc, Tim, y0, odeoption, Grp1B, par);
vFit= interp1(vT, vFit, tSpan);
```

```
vT= tSpan;


 %% Define diffFunc


 % par = [k3,   Kpten,  k6,    k7,    k8,    k9,    k10,   t1,   Kcat,  Kpten_1]
 %      par(1)  par(2)  par(3)  par(4)  par(5)  par(6)  par(7)  par(8)  par(9)  par(10)
     function dydt= diffFunc(t, y, Grp1B, par)
        global k4 k5 ktr h PTENB
     dydt = zeros(7,1);
     dydt(1)= k4*y(2)*y(7) - k5*y(1);
     dydt(2)= -par(1)*y(3)*(y(2)/(par(2)+y(2))) -
(y(6)^(par(8))/(par(9)^(par(8))+y(6)^(par(8))))*par(7)*y(4)*(y(2)/(par(10)+y(2))) -
k4*y(2)*y(7) + k5*y(1);
     dydt(3)= par(3)*y(5) - par(4)*y(3);
     dydt(4)= par(5)*y(5)*y(6) - par(6)*y(4);
     dydt(5)= (ktr/h)*(PTENB-y(5)) - par(3)*y(5)/h + par(4)*y(3)/h;
     dydt(6)= par(1)*y(3)*(y(2)/(par(2)+y(2))) +
(y(6)^(par(8))/(par(9)^(par(8))+y(6)^(par(8))))*par(7)*y(4)*(y(2)/(par(10)+y(2))) -
par(5)*y(5)*y(6) + par(6)*y(4);
     dydt(7)= (ktr/h)*(Grp1B-y(7)) - k4*y(2)*y(7)/h + k5*y(1)/h ;


     %dydt(1)= k4*y(2)*y(7) - k5*y(1);
     %dydt(2)= -nk3*y(3)*(y(2)/(nKpten+y(2))) -
(y(6)^(nt1)/(nKcat^(nt1)+y(6)^(nt1)))*nk10*y(4)*(y(2)/(nKpten_1+y(2))) - k4*y(2)*y(7)
+ k5*y(1);
     %dydt(3)= nk6*y(5) - nk7*y(3);
     %dydt(4)= nk8*y(5)*y(6) - nk9*y(4);
     %dydt(5)= (ktr/h)*(PTENB-y(5)) - nk6*y(5)/h + nk7*y(3)/h;
     %dydt(6)= nk3*y(3)*(y(2)/(nKpten+y(2))) +
(y(6)^(nt1)/(nKcat^(nt1)+y(6)^(nt1)))*nk10*y(4)*(y(2)/(nKpten_1+y(2))) -
```

```
nk8*y(5)*y(6) + nk9*y(4);
    %dydt(7)= (ktr/h)*(Grp1B-y(7)) - k4*y(2)*y(7)/h + k5*y(1)/h ;
    end
end
```

C. Fluorescence Intensity on BSMs

Goal: The file is used to quantify the fluorescence intensity around the bead.

Instructions

1. In the MATLAB command window, type the command below

multibeadfit(startframe, endframe, image_name.tif, radius_approx_pixel)

i.e. multibeadfit(1, 2, '1%PIP2+1%PIP3.tif', 11)

2. click “Enter”, then we will see three figures show up

3. Draw a box on "Figure 3" region without any beads as a background

4. The analysis result will show in txt file with the name "result1_2"

5. We extract the fluorescence intensity from column 5:

The first 10 results are from beads 1-10, fluorescence channel 1 (EGFP-PLC).

Next 10 results are from beads 1-10, fluorescence channel 2 (mCherry-Grp1).

6. Output: Bead number(column 1), Raw intensity per pixel (column 2), Radius (column 3), Width (column 4), Corrected intensity (column 5), Radius in micrometer (column 6)

Code

```
function results = multibeadfit(startframe,endframe,image,radius_approx_pixel,varargin)


%%
global a b adjustedimage num xmat ymat circlefit;


%% default parameters
mult = 16;
z = 2;  % zoom, default (z=2)
%% Load optional arguments
if not(isempty(varargin))
   try
      z = varargin{1}; %zoom is first optional argument
     %  index = varargin{2};
      mult = varargin{2}; % multiplier to convert 12 bit image to 16 bit image
   catch e
      e.message
   end
end


%%segregating images based on input variables
for i = startframe:endframe;


   J = imread(image,i);
   J = J*mult;
   filefrac = int2str(i);
   name = [filefrac '.tif'];
   imwrite (J, name);
```

```
end

framenum1 = int2str (startframe);
name1 = [framenum1 '.tif'];
J1 = imread(name1);

framenum2 = int2str (endframe);
name2 = [framenum2 '.tif'];
J2 = imread(name2);

J=J1+J2;

%global b_in b_out bmat
height = size (J,1);
width = size (J,2);

margin = 10; % margin around image

SF = 0.414320379601492/z; % set scale factor based on zoom

%% initialize values
startsigma = 40;%may need to change depending on the quality of the data , good ones, sigma<20
a = 2000;%may need to change

%%SS - added
Kmedian = medfilt2(J); % median filter to remove shot noise
```

```
cont = imadjust(Kmedian); % redajusted contrast


blow_up_fac = 10;
%resizing image continuously to close the edges
for i = 1:10
    cont = imresize(cont,blow_up_fac);
    cont = imresize(cont, 1/blow_up_fac);
end
figure, imshow(cont);
level = graythresh(cont);
BW = im2bw(cont,level); % converting from grayscale to binary image
figure, imshow(BW)
rad_range_max = radius_approx_pixel + 5;
rad_range_min = radius_approx_pixel - 5;
[centers radii] = imfindcircles(BW,[rad_range_min rad_range_max]); %approximate
radius range in pixels provided as an input for imfindcircles


numGUVs = size(radii,1);


numFrames = endframe-startframe+1;
intensity = zeros((numGUVs*numFrames),6);


%% background
figure, imshow (J), title 'Draw a box to select background' %background area needs to be
selected only once
ROI = getrect;
close all
```

```
%% main fitting loop: loop once for each set of points
for m = endframe:-1:startframe;
    framenum = int2str (m);
    name = [framenum '.tif'];
    J = imread(name);

    %% background

    bd = sum(sum(J(int16(ROI(2)):int16(ROI(2)+ROI(4)),
int16(ROI(1)):int16(ROI(1)+ROI(3)))))
    area = ROI(3)*ROI(4)
    b_out = bd/area
    if(b_out == 0)
        b_out = 1;
    end
    b = b_out

    %%
    for k = 1:numGUVs;
        % GUVnum = ceil(k/2) %get actual GUV number, since each GUV has two points
        %%load center point, initialize values

        x0 = round(centers(k,1));
        y0 = round(centers(k,2));
        r0 = floor(radii(k,1));

        xi = (x0 - r0 - margin);
```

```
if (xi <= 0); xi = 1; end
yi = (y0 - r0 - margin);
if (yi <= 0); yi = 1; end
xe = (x0 + r0 + margin);
if (xe > width); xe = width; end
ye = (y0 + r0 + margin);
if (ye > height); ye = height; end
adjustedimage = double (J(yi:ye,xi:xe));
imshow(adjustedimage,[]);
num=0;%number of fitting

awidth = size(adjustedimage,2);
aheight = size(adjustedimage,1);
xy = [x0-xi,y0-yi,r0,startsigma,a]; %x0 must be relative to new adjusted image

%% background
bd_w = sum(adjustedimage(:, 1:3));
bd_w = sum(bd_w)/3/aheight;
bd_e = sum(adjustedimage(:,awidth-2:awidth));
bd_e = sum (bd_e)/3/aheight;
J2 = adjustedimage';

bd_s = sum(J2(:,aheight-2:aheight));
bd_s = sum(bd_s)/awidth/3;
bd_n = sum(J2(:,1:3));
bd_n = sum(bd_n)/awidth/3;
b_out = (bd_e+bd_w+bd_n+bd_s)/4;
```

```
b2 = b_out;
%%
xvec = 1:awidth;
xmat = xvec;
yvec = (1:aheight)';
ymat = yvec;
for i = 1:awidth-1
   ymat = cat(2,ymat,yvec);
end
for i = 1:aheight-1
   xmat = cat(1,xmat,xvec);
end

%% fitting
xy0 = xy;

[xy,fval,exitflag] = fminsearch (@circlefitter,xy,optimset('TolX',1e-5,'TolFun',1e-
3));

%num
xy

imshow(circlefit,[]); % displaying fitted gaussian image

GUVnum = k;

%% save data
```

```
        j = (m - startframe)*numGUVs + GUVnum; %intensity index
        if (((abs(xy(3)-xy0(3))/xy0(3)>0.5)||(abs(xy(4)-xy0(4))/xy0(4)>2)))
            xy = xy0;
            fprintf ('frame %d is wrong!\n', GUVnum)
            intensity (j,1) = GUVnum;
            intensity (j,2:6) = 0;%delete one line intead of keeping all zeros
        else
            intensity (j,1) = GUVnum; %frame #
            intensity (j,2) = (sum(sum(circlefit)) -
b*awidth*aheight)/(2*pi*xy(3))/sqrt(xy(4)); %raw intensity per pixel
            intensity (j,3) = xy(3);%radius
            intensity (j,4) = (xy(4)).^0.5;%WIDTH
            intensity (j,5) = intensity (j,2)*intensity (j,4)/z;%intensity corrected
            intensity (j,6) = (intensity (j,3)+intensity (j,4)-5)*SF;% radius in um
        end

    end
end

%% save text file with results
framenum0 = int2str (startframe);
framenum1 = int2str (endframe);
name = ['result' framenum0 '_' framenum1 '.txt'];
save(name, 'intensity', '-ASCII');
results = intensity;

end
```

```
function [sse] = circlefitter(xy)

global  b adjustedimage num xmat ymat circlefit;
x0 = xy(1);
y0 = xy(2);
r0 = xy(3);
sigma_r = xy (4);
a0 = xy (5);
rmat = ((xmat-x0).^2+(ymat-y0).^2).^0.5;
circlefit = a0*exp(-(rmat-r0).^2/sigma_r)+b;

sse = sum(sum((adjustedimage - circlefit).^2));
num = num+1;
end
```

D. Velocity Plot

Goal: This file is used to simulate how PIP3 hydrolysis rate change with PIP3 content at certain sensor proteins and enzyme concentrations.

Instructions

1. Click "run" directly

2. The analysis result will show in txt file with the name "results-2"

3. First column: PIP3 concentration; second column: rate of PIP3 hydrolysis

Code

```
%% Parameters
% PIP3 Hydrolysis
kc1=11; % s-1; % Kcat of PTEN
ka_PTEN = 0.0017; % m/s; % Associaiton of PTEN to membrane
kd_PTEN = 0.7; % s-1; % Dissociaiton of PTEN to membrane
KM1 = 0.002; % uMm; % Michaelis-Menten constant of PTEN
kc2 = 19; % s-1; % Catalytic constant of PTEN-PIP2 to PIP3
n=2; % Hill coefficient
KM2 = 7.9E-6; % uMm
KM3 = 2.3E-5; % uMm; % Michaelis-Menten constant of PTEN-PIP2
KM4 = 2.5e-5; % uMm; % Michaelis-Menten constant of PI3K
Vmax=7.5e-5; % uMm*s-1; % Max. velocity of PIP3 formation by PI3K

%PIP2-PTEN Binding (We only care equilibrium binding constant
        % KD = kd_PTEN_PIP2 / ka_PTEN_PIP2 = 0.02 uM)
ka_PTEN_PIP2 = 15; % Association constant of PTEN to PIP2
kd_PTEN_PIP2 = 0.3; % Dissociation constant of PTEN to PIP2

% PIP3-Grp1 Binding (We only care equilibrium binding constant
        % KD = kd_Grp1 / ka_Grp1 = 0.11 uM)
ka_Grp1 = 1; % Association constant of Grp1 to PIP3
kd_Grp1 = 0.11; % Dissociation constant of Grp1 to PIP3

% PIP2-PLC Binding (We only care equilibrium binding constant
        % KD = kd_PLC / ka_PLC = 0.375 uM)
```

```
ka_PLC = 0.267; % Association constant of PLC to PIP2

kd_PLC = 0.1; % Dissociation constant of PLC to PIP2


% Sensors & Enzymes

PIT=5E-5; % uMm; % For 2% PIP total

Grp1 = 0.11; % uM

PLC = 0.375; % uM


%% Binding Equilibrium

   % Scanning PIP2_Init

PTEN = 0.025; % uM


vPIP3_Matrix = [];

PIP3_Matrix = [];

for PIP2 = 0:0.0025*PIT:0.3*PIT;


   PTEN_PIP2 = (ka_PTEN_PIP2/kd_PTEN_PIP2)*PTEN*PIP2;

   PLC_PIP2 = (ka_PLC/kd_PLC)*PLC*PIP2;

   PIP3 = (PIT - PIP2 - PTEN_PIP2 - PLC_PIP2)/(1+(ka_Grp1/kd_Grp1)*Grp1);

                        Grp1_PIP3 = (ka_Grp1/kd_Grp1)*Grp1*PIP3;


   vPIP3 = -kc1*(ka_PTEN/kd_PTEN)*PTEN*(PIP3/(KM1+PIP3)) -
kc2*(PIP2)^n/(KM2^n+PIP2^n)*(PTEN_PIP2)*(PIP3/(KM3+PIP3))+Vmax*(PIP2/(KM
4+PIP2));


   PIP3_Matrix = [PIP3_Matrix; PIP3];

   vPIP3_Matrix = [vPIP3_Matrix; vPIP3]; %%add solution data points (vPIP3) to
existing array
```

```
scatter(PIP3, vPIP3)
hold on

end

savedata = [PIP3_Matrix, vPIP3_Matrix]; %concantenate [PIP3] and vPIP3
name = ['results-' int2str(n) '.txt'];
save(name, 'savedata', '-ASCII');
```

BIBLOGRAPHY

1. Vanhaesebroeck B, Stephens L, Hawkins P. PI3K signalling: the path to discovery and understanding. Nature reviews Molecular cell biology. 2012;13(3):195-203. doi: 10.1038/nrm3290. PubMed PMID: 22358332.
2. Chalhoub N, Baker SJ. PTEN and the PI3-kinase pathway in cancer. Annual review of pathology. 2009;4:127-50. doi: 10.1146/annurev.pathol.4.110807.092311. PubMed PMID: 18767981; PubMed Central PMCID: PMC2710138.
3. Thorpe LM, Yuzugullu H, Zhao JJ. PI3K in cancer: divergent roles of isoforms, modes of activation and therapeutic targeting. Nature Reviews Cancer. 2015;15(1):7-24. doi: 10.1038/nrc3860. PubMed PMID: WOS:000346833100006.
4. Mayer IA, Arteaga CL. The PI3K/AKT Pathway as a Target for Cancer Treatment. In: Caskey CT, editor. Annual Review of Medicine, Vol 67. Annual Review of Medicine. 67. Palo Alto: Annual Reviews; 2016. p. 11-28.
5. Hennessy BT, Smith DL, Ram PT, Lu YL, Mills GB. Exploiting the PI3K/AKT pathway for cancer drug discovery. Nat Rev Drug Discov. 2005;4(12):988-1004. doi: 10.1038/nrd1902. PubMed PMID: WOS:000233774900020.
6. Martelli AM, Evangelisti C, Chiarini F, McCubrey JA. The phosphatidylinositol 3-kinase/Akt/mTOR signaling network as a therapeutic target in acute myelogenous leukemia patients. Oncotarget. 2010;1(2):89-103. doi: 10.18632/oncotarget.114. PubMed PMID: WOS:000293476000004.
7. Chalhoub N, Baker SJ. PTEN and the PI3-Kinase Pathway in Cancer. Annual Review of Pathology-Mechanisms of Disease. Annual Review of Pathology-Mechanisms of Disease. 4. Palo Alto: Annual Reviews; 2009. p. 127-50.
8. Engelman JA, Luo J, Cantley LC. The evolution of phosphatidylinositol 3-kinases as regulators of growth and metabolism. Nat Rev Genet. 2006;7(8):606-19. doi: 10.1038/nrg1879. PubMed PMID: WOS:000239118400013.
9. Yu JH, Wjasow C, Backer JM. Regulation of the p85/p110 alpha Phosphatidylinositol 3 '-kinase - Distinct roles for the N-terminal and C-terminal SH2 domains. J Biol Chem. 1998;273(46):30199-203. doi: 10.1074/jbc.273.46.30199. PubMed PMID: WOS:000077008100023.
10. Yu JH, Zhang YT, McIlroy J, Rordorf-Nikolic T, Orr GA, Backer JM. Regulation of the p85/p110 phosphatidylinositol 3 '-kinase: Stabilization and inhibition of the p110 alpha catalytic subunit by the p85 regulatory subunit. Mol Cell Biol. 1998;18(3):1379-87. doi: 10.1128/mcb.18.3.1379. PubMed PMID: WOS:000072131700026.
11. Thorpe LM, Yuzugullu H, Zhao JJ. PI3K in cancer: divergent roles of isoforms, modes of activation and therapeutic targeting. Nature reviews Cancer. 2015;15(1):7-24. doi: 10.1038/nrc3860. PubMed PMID: 25533673; PubMed Central PMCID: PMC4384662.
12. Samuels Y, Wang ZH, Bardelli A, Silliman N, Ptak J, Szabo S, et al. High frequency of mutations of the PIK3CA gene in human cancers. Science. 2004;304(5670):554-. doi: 10.1126/science.1096502. PubMed PMID: WOS:000220975100039.
13. Lee JY, Engelman JA, Cantley LC. Biochemistry - PI3K charges ahead. Science. 2007;317(5835):206-7. doi: 10.1126/science.1146073. PubMed PMID: WOS:000247968600027.
14. Worby CA, Dixon JE. PTEN. In: Kornberg RD, editor. Annual Review of Biochemistry, Vol 83. Annual Review of Biochemistry. 83. Palo Alto: Annual Reviews; 2014. p. 641-69.

15. Ross AH, Gericke A. Phosphorylation keeps PTEN phosphatase closed for business. Proc Natl Acad Sci U S A. 2009;106(5):1297-8. doi: 10.1073/pnas.0812473106. PubMed PMID: WOS:000263074600002.
16. Rahdar M, Inoue T, Meyer T, Zhang J, Vazquez F, Devreotes PN. A phosphorylation-dependent intramolecular interaction regulates the membrane association and activity of the tumor suppressor PTEN. Proceedings of the National Academy of Sciences of the United States of America. 2009;106(2):480-5. doi: 10.1073/pnas.811212106. PubMed PMID: WOS:000262804000024.
17. Lee JO, Yang HJ, Georgescu MM, Di Cristofano A, Maehama T, Shi YG, et al. Crystal structure of the PTEN tumor suppressor: Implications for its phosphoinositide phosphatase activity and membrane association. Cell. 1999;99(3):323-34. doi: Doi 10.1016/S0092-8674(00)81663-3. PubMed PMID: WOS:000083440600010.
18. Song MS, Salmena L, Pandolfi PP. The functions and regulation of the PTEN tumour suppressor. Nat Rev Mol Cell Biol. 2012;13(5):283-96. doi: 10.1038/nrm3330. PubMed PMID: WOS:000303111800012.
19. Hollander MC, Blumenthal GM, Dennis PA. PTEN loss in the continuum of common cancers, rare syndromes and mouse models. Nature Reviews Cancer. 2011;11(4):289-301. doi: 10.1038/nrc3037. PubMed PMID: WOS:000288741300014.
20. Hobert JA, Eng C. PTEN hamartoma tumor syndrome: An overview. Genetics in Medicine. 2009;11(10):687-94. doi: 10.1097/GIM.0b013e3181ac9aea. PubMed PMID: WOS:000271449800001.
21. Milella M, Falcone I, Conciatori F, Incani UC, Del Curatolo A, Inzerilli N, et al. PTEN: multiple functions in human malignant tumors. Front Oncol. 2015;5. doi: 10.3389/fonc.2015.00024. PubMed PMID: WOS:000359076100001.
22. Di Paolo G, De Camilli P. Phosphoinositides in cell regulation and membrane dynamics. Nature. 2006;443(7112):651-7. doi: 10.1038/nature05185. PubMed PMID: WOS:000241160500037.
23. Schink KO, Tan KW, Stenmark H. Phosphoinositides in Control of Membrane Dynamics. In: Schekman R, editor. Annual Review of Cell and Developmental Biology, Vol 32. Annual Review of Cell and Developmental Biology. 32. Palo Alto: Annual Reviews; 2016. p. 143-71.
24. Behnia R, Munro S. Organelle identity and the signposts for membrane traffic. Nature. 2005;438(7068):597-604. doi: 10.1038/nature04397. PubMed PMID: WOS:000233593100037.
25. Guo J, Wenk MR, Pellegrini L, Onofri F, Benfenati F, De Camilli P. Phosphatidylinositol 4-kinase type II alpha is responsible for the phosphatidylinositol 4-kinase activity associated with synaptic vesicles. Proc Natl Acad Sci U S A. 2003;100(7):3995-4000. doi: 10.1073/pnas.0230488100. PubMed PMID: WOS:000182058400084.
26. Ketel K, Krauss M, Nicot AS, Puchkov D, Wieffer M, Muller R, et al. A phosphoinositide conversion mechanism for exit from endosomes. Nature. 2016;529(7586):408-+. doi: 10.1038/nature16516. PubMed PMID: WOS:000368354800049.
27. Rohatgi R, Ho HYH, Kirschner MW. Mechanism of N-WASP activation by CDC42 and phosphatidylinositol 4,5-bisphosphate. J Cell Biol. 2000;150(6):1299-309. doi: 10.1083/jcb.150.6.1299. PubMed PMID: WOS:000089454500009.
28. Pollard TD, Borisy GG. Cellular motility driven by assembly and disassembly of actin filaments. Cell. 2003;112(4):453-65. doi: 10.1016/s0092-8674(03)00120-x. PubMed PMID: WOS:000181252600005.

29. Chen CL, Wang Y, Sesaki H, Iijima M. Myosin I Links PIP3 Signaling to Remodeling of the Actin Cytoskeleton in Chemotaxis. Sci Signal. 2012;5(209). doi: 10.1126/scisignal.2002446. PubMed PMID: WOS:000300222600001.
30. Lim JP, Wang JTH, Kerr MC, Teasdale RD, Gleeson PA. A role for SNX5 in the regulation of macropinocytosis. BMC Cell Biol. 2008;9. doi: 10.1186/1471-2121-9-58. PubMed PMID: WOS:000264917300001.
31. Haslam RJ, Koide HB, Hemmings BA. PLECKSTRIN DOMAIN HOMOLOGY. Nature. 1993;363(6427):309-10. doi: 10.1038/363309b0. PubMed PMID: WOS:A1993LD91700036.
32. Mayer BJ, Ren RB, Clark KL, Baltimore D. A PUTATIVE MODULAR DOMAIN PRESENT IN DIVERSE SIGNALING PROTEINS. Cell. 1993;73(4):629-30. doi: 10.1016/0092-8674(93)90244-k. PubMed PMID: WOS:A1993LD83000003.
33. Maffucci T, Falasca M. Specificity in pleckstrin homology (PH) domain membrane targeting: a role for a phosphoinositide-protein co-operative mechanism. FEBS Lett. 2001;506(3):173-9. doi: 10.1016/s0014-5793(01)02909-x. PubMed PMID: WOS:000171688200002.
34. Prashek J, Truong T, Yao XL. Crystal Structure of the Pleckstrin Homology Domain from the Ceramide Transfer Protein: Implications for Conformational Change upon Ligand Binding. PLoS One. 2013;8(11). doi: 10.1371/journal.pone.0079590. PubMed PMID: WOS:000327308500079.
35. Lemmon MA, Ferguson KM. Signal-dependent membrane targeting by pleckstrin homology (PH) domains. Biochem J. 2000;350:1-18. doi: 10.1042/0264-6021:3500001. PubMed PMID: WOS:000089067100001.
36. Garcia P, Gupta R, Shah S, Morris AJ, Rudge SA, Scarlata S, et al. The pleckstrin homology domain of phospholipase C-delta(1) binds with high affinity to phosphatidylinositol 4,5-bisphosphate in bilayer membranes. Biochemistry. 1995;34(49):16228-34. doi: 10.1021/bi00049a039. PubMed PMID: WOS:A1995TK39200039.
37. Lemmon MA, Ferguson KM, Obrien R, Sigler PB, Schlessinger J. SPECIFIC AND HIGH-AFFINITY BINDING OF INOSITOL PHOSPHATES TO AN ISOLATED PLECKSTRIN HOMOLOGY DOMAIN. Proc Natl Acad Sci U S A. 1995;92(23):10472-6. doi: 10.1073/pnas.92.23.10472. PubMed PMID: WOS:A1995TD89000006.
38. Razzini G, Ingrosso A, Brancaccio A, Sciacchitano S, Esposito DL, Falasca M. Different subcellular localization and phosphoinositides binding of insulin receptor substrate protein pleckstrin homology domains. Mol Endocrinol. 2000;14(6):823-36. doi: 10.1210/me.14.6.823. PubMed PMID: WOS:000087430600008.
39. Cantley LC. The phosphoinositide 3-kinase pathway. Science. 2002;296(5573):1655-7. doi: 10.1126/science.296.5573.1655. PubMed PMID: WOS:000175976200049.
40. Miao B, Skidan I, Yang J, You Z, Fu X, Famulok M, et al. Inhibition of cell migration by PITENINs: the role of ARF6. Oncogene. 2012;31(39):4317-32. doi: 10.1038/onc.2011.593. PubMed PMID: WOS:000309520200006.
41. Kavran JM, Klein DE, Lee A, Falasca M, Isakoff SJ, Skolnik EY, et al. Specificity and promiscuity in phosphoinositide binding by Pleckstrin homology domains. J Biol Chem. 1998;273(46):30497-508. doi: DOI 10.1074/jbc.273.46.30497. PubMed PMID: WOS:000077008100065.
42. Venkateswarlu K, Oatey PB, Tavare JM, Cullen PJ. Insulin-dependent translocation of ARNO to the plasma membrane of adipocytes requires phosphatidylinositol 3-kinase. Curr Biol. 1998;8(8):463-6. doi: 10.1016/s0960-9822(98)70181-2. PubMed PMID: WOS:000073081000019.

43. Janetopoulos C, Ma L, Devreotes PN, Iglesias PA. Chemoattractant-induced phosphatidylinositol 3,4,5-trisphosphate accumulation is spatially amplified and adapts, independent of the actin cytoskeleton. Proceedings of the National Academy of Sciences of the United States of America. 2004;101(24):8951-6. doi: DOI 10.1073/pnas.0402152101. PubMed PMID: WOS:000222104900023.
44. Billadeau DD. PTEN gives neutrophils direction. Nat Immunol. 2008;9(7):716-8. doi: 10.1038/ni0708-716. PubMed PMID: WOS:000256904900006.
45. Iglesias PA, Devreotes PN. Navigating through models of chemotaxis. Curr Opin Cell Biol. 2008;20(1):35-40. doi: 10.1016/j.ceb.2007.11.011. PubMed PMID: WOS:000253545200006.
46. Shi CJ, Huang CH, Devreotes PN, Iglesias PA. Interaction of Motility, Directional Sensing, and Polarity Modules Recreates the Behaviors of Chemotaxing Cells. PLoS Comput Biol. 2013;9(7). doi: 10.1371/journal.pcbi.1003122. PubMed PMID: WOS:000322320200010.
47. Parent CA, Devreotes PN. A cell's sense of direction. Science. 1999;284(5415):765-70. doi: 10.1126/science.284.5415.765. PubMed PMID: WOS:000080056200035.
48. Devreotes P, Janetopoulos C. Eukaryotic chemotaxis: Distinctions between directional sensing and polarization. J Biol Chem. 2003;278(23):20445-8. doi: 10.1074/jbc.R300010200. PubMed PMID: WOS:000183230500001.
49. Bryant DM, Mostov KE. From cells to organs: building polarized tissue. Nat Rev Mol Cell Biol. 2008;9(11):887-901. doi: 10.1038/nrm2523. PubMed PMID: WOS:000260312700014.
50. Martin-Belmonte F, Gassama A, Datta A, Yu W, Rescher U, Gerke V, et al. PTEN-mediated apical segregation of phosphoinositides controls epithelial morphogenesis through Cdc42. Cell. 2007;128(2):383-97. doi: 10.1016/j.cell.2006.11.051. PubMed PMID: WOS:000244420500021.
51. Pinal N, Goberdhan DCI, Collinson L, Fujita Y, Cox IM, Wilson C, et al. Regulated and polarized Ptdins(3,4,5)P3 accumulation is essential for apical membrane morphogenesis in photoreceptor epithelial cells (vol 16, pg 140, 2006). Curr Biol. 2006;16(3):332-. doi: 10.1016/j.cub.2006.01.049. PubMed PMID: WOS:000235347400036.
52. Veglio A, Gamba A, Nicodemi M, Bussolino F, Serini G. Symmetry breaking mechanism for epithelial cell polarization. Phys Rev E. 2009;80(3). doi: 10.1103/PhysRevE.80.031919. PubMed PMID: WOS:000270383400118.
53. Semplice M, Veglio A, Naldi G, Serini G, Gamba A. A Bistable Model of Cell Polarity. PLoS One. 2012;7(2). doi: 10.1371/journal.pone.0030977. PubMed PMID: WOS:000302916100012.
54. Matsuoka S, Ueda M. Mutual inhibition between PTEN and PIP3 generates bistability for polarity in motile cells. Nature Communications. 2018;9(1):4481. doi: 10.1038/s41467-018-06856-0.
55. Ferrell JE, Ha SH. Ultrasensitivity part I: Michaelian responses and zero-order ultrasensitivity. Trends BiochemSci. 2014;39(10):496-503. doi: 10.1016/j.tibs.2014.08.003. PubMed PMID: WOS:000343069300009.
56. Gomez-Uribe C, Verghese GC, Mirny LA. Operating regimes of signaling cycles: Statics, dynamics, and noise filtering. PLoS Comput Biol. 2007;3(12):2487-97. doi: 10.1371/journal.pcbi.0030246. PubMed PMID: WOS:000252564300008.
57. Ferrell JE, Ha SH. Ultrasensitivity part II: multisite phosphorylation, stoichiometric inhibitors, and positive feedback. Trends BiochemSci. 2014;39(11):556-69. doi: 10.1016/j.tibs.2014.09.003. PubMed PMID: WOS:000344905900008.
58. Ferrell JE, Ha SH. Ultrasensitivity part III: cascades, bistable switches, and oscillators. Trends BiochemSci. 2014;39(12):612-8. doi: 10.1016/j.tibs.2014.10.002. PubMed PMID: WOS:000346233300007.

59. Kim SY, Ferrell JE. Substrate competition as a source of ultrasensitivity in the inactivation of Wee1. Cell. 2007;128(6):1133-45. doi: 10.1016/j.cell.2007.01.039. PubMed PMID: WOS:000245396200019.
60. Xiong W, Ferrell JE. A positive-feedback-based bistable 'memory module' that governs a cell fate decision. Nature. 2003;426(6965):460-5. doi: 10.1038/nature02089. PubMed PMID: WOS:000186800800042.
61. Angeli D, Ferrell JE, Sontag ED. Detection of multistability, bifurcations, and hysteresis in a large class of biological positive-feed back systems. Proc Natl Acad Sci U S A. 2004;101(7):1822-7. doi: 10.1073/pnas.0308265100. PubMed PMID: WOS:000189032600008.
62. Novak B, Tyson JJ. Design principles of biochemical oscillators. Nat Rev Mol Cell Biol. 2008;9(12):981-91. doi: 10.1038/nrm2530. PubMed PMID: WOS:000261126800017.
63. Legewie S, Bluthgen N, Herzel H. Quantitative analysis of ultrasensitive responses. Febs J. 2005;272(16):4071-9. doi: 10.1111/j.1742-4658.2005.04818.x. PubMed PMID: WOS:000231021400006.
64. Hardie DG, Salt IP, Hawley SA, Davies SP. AMP-activated protein kinase: an ultrasensitive system for monitoring cellular energy charge. Biochem J. 1999;338:717-22. doi: 10.1042/0264-6021:3380717. PubMed PMID: WOS:000079304600020.
65. Bradshaw JM, Kubota Y, Meyer T, Schulman H. An ultrasensitive Ca2+/calmodulin-dependent protein kinase II-protein phosphatase 1 switch facilitates specificity in postsynaptic calcium signaling. Proc Natl Acad Sci U S A. 2003;100(18):10512-7. doi: 10.1073/pnas.1932759100. PubMed PMID: WOS:000185119300068.
66. Kaech SM, Cui WG. Transcriptional control of effector and memory CD8(+) T cell differentiation. Nat Rev Immunol. 2012;12(11):749-61. doi: 10.1038/nri3307. PubMed PMID: WOS:000310523400009.
67. Zhang LJ, Tschumi BO, Lopez-Mejia IC, Oberle SG, Meyer M, Samson G, et al. Mammalian Target of Rapamycin Complex 2 Controls CD8 T Cell Memory Differentiation in a Foxo1-Dependent Manner. Cell Reports. 2016;14(5):1206-17. doi: 10.1016/j.celrep.2015.12.095. PubMed PMID: WOS:000369616100021.
68. Saltiel AR, Kahn CR. Insulin signalling and the regulation of glucose and lipid metabolism. Nature. 2001;414(6865):799-806. doi: 10.1038/414799a. PubMed PMID: WOS:000172676200060.
69. Cizmeci D, Arkun Y. Regulatory Networks and Complex Interactions between the Insulin and Angiotensin II Signalling Systems: Models and Implications for Hypertension and Diabetes. PLoS One. 2013;8(12). doi: 10.1371/journal.pone.0083640. PubMed PMID: WOS:000329325200098.
70. Arkun Y. Dynamic Modeling and Analysis of the CrossTalk between Insulin/AKT and MAPK/ERK Signaling Pathways. PloS one. 2016;11(3). doi: 10.1371/journal.pone.0149684. PubMed PMID: WOS:000371434500042.
71. Wee KB, Aguda BD. Akt versus p53 in a network of oncogenes and tumor suppressor genes regulating cell survival and death. Biophysical journal. 2006;91(3):857-65. doi: 10.1529/biophysj.105.077693. PubMed PMID: WOS:000239086800011.
72. Nguyen HH, Park J, Kang S, Kim M. Surface Plasmon Resonance: A Versatile Technique for Biosensor Applications. Sensors. 2015;15(5):10481-510. doi: 10.3390/s150510481. PubMed PMID: WOS:000357183100046.
73. Deng SJ, Wang P, Yu XL. Phase-Sensitive Surface Plasmon Resonance Sensors: Recent Progress and Future Prospects. Sensors. 2017;17(12). doi: 10.3390/s17122819. PubMed PMID: WOS:000423285800119.

74. Goldstein B, Coombs D, He XY, Pineda AR, Wofsy C. The influence of transport on the kinetics of binding to surface receptors: application to cells and BIAcore. J Mol Recognit. 1999;12(5):293-9. doi: 10.1002/(sici)1099-1352(199909/10)12:5<293::aid-jmr472>3.3.co;2-d. PubMed PMID: WOS:000084108400004.
75. Mason T, Pineda AR, Wofsy C, Goldstein B. Effective rate models for the analysis of transport-dependent biosensor data. Math Biosci. 1999;159(2):123-44. doi: 10.1016/s0025-5564(99)00023-1. PubMed PMID: WOS:000081384100003.
76. Myszka DG, He X, Dembo M, Morton TA, Goldstein B. Extending the range of rate constants available from BIACORE: Interpreting mass transport-influenced binding data. Biophys J. 1998;75(2):583-94. PubMed PMID: WOS:000075206000002.
77. Strogatz SH. Nonlinear Dynamics and Chaos : With Applications to Physics, Biology, Chemistry, and Engineering 2018. Available from: https://www.taylorfrancis.com/books/9780429961113.
78. Liu C, Deb S, Ferreira VS, Xu E, Baumgart T. Kinetics of PTEN-mediated PI(3,4,5)P3 hydrolysis on solid supported membranes. PloS one. 2018;13(2). doi: 10.1371/journal.pone.0192667. PubMed PMID: WOS:000425283900045.
79. Kawase T, Ohki R, Shibata T, Tsutsumi S, Kamimura N, Inazawa J, et al. PH Domain-Only Protein PHLDA3 Is a p53-Regulated Repressor of Akt. Cell. 2009;136(3):535-50. doi: 10.1016/j.cell.2008.12.002. PubMed PMID: WOS:000263120600022.
80. Varnai P, Bondeva T, Tamas P, Toth B, Buday L, Hunyady L, et al. Selective cellular effects of overexpressed pleckstrin-homology domains that recognize PtdIns(3,4,5)P-3 suggest their interaction with protein binding partners. J Cell Sci. 2005;118(20):4879-88. doi: 10.1242/jcs.02606. PubMed PMID: WOS:000233392300025.
81. Varnai P, Balla T. Visualization of phosphoinositides that bind pleckstrin homology domains: Calcium- and agonist-induced dynamic changes and relationship to myo- H-3 inositol-labeled phosphoinositide pools. J Cell Biol. 1998;143(2):501-10. doi: 10.1083/jcb.143.2.501. PubMed PMID: WOS:000076618200018.
82. Varnai P, Lin X, Lee SB, Tuymetova G, Bondeva T, Spat A, et al. Inositol lipid binding and membrane localization of isolated pleckstrin homology (PH) domains - Studies on the PH domains of phospholipase C delta(1) and p130. J Biol Chem. 2002;277(30):27412-22. doi: 10.1074/jbc.M109672200. PubMed PMID: WOS:000177055900091.
83. Huang CH, Mandelker D, Schmidt-Kittler O, Samuels Y, Velculescu VE, Kinzler KW, et al. The structure of a human p110 alpha/p85 alpha complex elucidates the effects of oncogenic PI3K alpha mutations. Science. 2007;318(5857):1744-8. doi: 10.1126/science.1150799. PubMed PMID: WOS:000251616800031.
84. Redfern RE, Redfern D, Furgason MLM, Munson M, Ross AH, Gericke A. PTEN phosphatase selectively binds phosphoinositides and undergoes structural changes. Biochemistry. 2008;47:2162-71. doi: 10.1021/bi702114w. PubMed PMID: WOS:000253102000034.
85. Khan F, He MY, Taussig MJ. Double-hexahistidine tag with high-affinity binding for protein immobilization, purification, and detection on Ni-nitrilotriacetic acid surfaces. Anal Chem. 2006;78(9):3072-9. doi: 10.1021/ac060184l. PubMed PMID: WOS:000237456400029.
86. Redfern RE, Redfern D, Furgason MLM, Munson M, Ross AH, Gericke A. PTEN phosphatase selectively binds phosphoinositides and undergoes structural changes. Biochemistry. 2008;47(7):2162-71. doi: 10.1021/bi702114w. PubMed PMID: WOS:000253102000034.

87. Zhou SY, Shoelson SE, Chaudhuri M, Gish G, Pawson T, Haser WG, et al. SH2 DOMAINS RECOGNIZE SPECIFIC PHOSPHOPEPTIDE SEQUENCES. Cell. 1993;72(5):767-78. doi: 10.1016/0092-8674(93)90404-e. PubMed PMID: WOS:A1993KR43600012.
88. Lee JN, Park C, Whitesides GM. Solvent compatibility of poly(dimethylsiloxane)-based microfluidic devices. Anal Chem. 2003;75(23):6544-54. doi: 10.1021/ac0346712. PubMed PMID: WOS:000186986000028.
89. Weibel DB, Siegel AC, Lee A, George AH, Whitesides GM. Pumping fluids in microfluidic systems using the elastic deformation of poly(dimethylsiloxane). Lab Chip. 2007;7(12):1832-6. doi: 10.1039/b714664g. PubMed PMID: WOS:000251121000037.
90. Brian AA, McConnell HM. Allogeneic stimulation of cytotoxic T cells by supported planar membranes. Proceedings of the National Academy of Sciences. 1984;81(19):6159-63. doi: 10.1073/pnas.81.19.6159.
91. Reviakine I, Brisson A. Formation of supported phospholipid bilayers from unilamellar vesicles investigated by atomic force microscopy. Langmuir. 2000;16(4):1806-15. doi: 10.1021/la9903043. PubMed PMID: WOS:000085412600048.
92. Yang TL, Jung SY, Mao HB, Cremer PS. Fabrication of phospholipid bilayer-coated microchannels for on-chip immunoassays. Anal Chem. 2001;73(2):165-9. doi: 10.1021/ac000997o. PubMed PMID: WOS:000166366000004.
93. Lai CL, Srivastava A, Pilling C, Chase AR, Falke JJ, Voth GA. Molecular Mechanism of Membrane Binding of the GRP1 PH Domain. J Mol Biol. 2013;425(17):3073-90. doi: DOI 10.1016/j.jmb.2013.05.026. PubMed PMID: WOS:000323860300005.
94. Jennissen HP. Boundary-layer exchange by bubble: A novel method for generating transient nanofluidic layers. Phys Fluids. 2005;17(10). doi: 10.1063/1.1990207. PubMed PMID: WOS:000232939200017.
95. Czech MP. PIP2 and PIP3: Complex roles at the cell surface. Cell. 2000;100(6):603-6. doi: Doi 10.1016/S0092-8674(00)80696-0. PubMed PMID: WOS:000085983800002.
96. Leslie NR, Batty IH, Maccario H, Davidson L, Downes CP. Understanding PTEN regulation: PIP(2), polarity and protein stability. Oncogene. 2008;27:5464-76. doi: 10.1038/onc.2008.243. PubMed PMID: WOS:000259280700008.
97. McConnachie G, Pass I, Walker SM, Downes CP. Interfacial kinetic analysis of the tumour suppressor phosphatase, PTEN: evidence for activation by anionic phospholipids. The Biochemical journal. 2003;371(Pt 3):947-55. doi: 10.1042/BJ20021848. PubMed PMID: 12534371; PubMed Central PMCID: PMC1223325.
98. Yasui M, Matsuoka S, Ueda M. PTEN hopping on the cell membrane is regulated via a positively-charged C2 domain. PLoS computational biology. 2014;10(9):e1003817. doi: 10.1371/journal.pcbi.1003817. PubMed PMID: 25211206; PubMed Central PMCID: PMC4161299.
99. Lumb CN, Sansom MSP. Defining the Membrane-Associated State of the PTEN Tumor Suppressor Protein. Biophys J. 2013;104(3):613-21. doi: DOI 10.1016/j.bpj.2012.12.002. PubMed PMID: WOS:000314619900012.
100. Campbell RB, Liu FH, Ross AH. Allosteric activation of PTEN phosphatase by phosphatidylinositol 4,5-bisphosphate. J Biol Chem. 2003;278(36):33617-20. doi: DOI 10.1074/jbc.C300296200. PubMed PMID: WOS:000185047500003.
101. Maehama T, Dixon JE. The tumor suppressor, PTEN/MMAC1, dephosphorylates the lipid second messenger, phosphatidylinositol 3,4,5-trisphosphate. The Journal of biological chemistry. 1998;273(22):13375-8. PubMed PMID: 9593664.

102. Maehama T, Taylor GS, Slama JT, Dixon JE. A sensitive assay for phosphoinositide phosphatases. Analytical biochemistry. 2000;279(2):248-50. doi: 10.1006/abio.2000.4497. PubMed PMID: 10706796.
103. Campbell RB, Liu F, Ross AH. Allosteric activation of PTEN phosphatase by phosphatidylinositol 4,5-bisphosphate. The Journal of biological chemistry. 2003;278(36):33617-20. doi: 10.1074/jbc.C300296200. PubMed PMID: 12857747.
104. Mak LH, Vilar R, Woscholski R. Characterisation of the PTEN inhibitor VO-OHpic. Journal of chemical biology. 2010;3(4):157-63. doi: 10.1007/s12154-010-0041-7. PubMed PMID: 21643420; PubMed Central PMCID: PMC2957887.
105. Verger R, Mieras MC, de Haas GH. Action of phospholipase A at interfaces. The Journal of biological chemistry. 1973;248(11):4023-34. PubMed PMID: 4736081.
106. Spinelli L, Leslie NR. Assaying PTEN catalysis in vitro. Methods. 2015;77-78:51-7. doi: 10.1016/j.ymeth.2014.11.003. PubMed PMID: 25461809.
107. Maehama T, Taylor GS, Slama JT, Dixon JE. A sensitive assay for phosphoinositide phosphatases. Anal Biochem. 2000;279(2):248-50. doi: DOI 10.1006/abio.2000.4497. PubMed PMID: WOS:000086021600017.
108. Larsen J, Hatzakis NS, Stamou D. Observation of Inhomogeneity in the Lipid Composition of Individual Nanoscale Liposomes. J Am Chem Soc. 2011;133(28):10685-7. doi: Doi 10.1021/Ja203984j. PubMed PMID: WOS:000293113200003.
109. Cremer PS, Boxer SG. Formation and spreading of lipid bilayers on planar glass supports. J Phys Chem B. 1999;103(13):2554-9. doi: Doi 10.1021/Jp983996x. PubMed PMID: WOS:000079612000030.
110. Harishchandra R, Neumann B, Gericke A, Ross A. Biophysical methods for the characterization of PTEN/Lipid bilayer interactions. Methods. 2015;77-78:125 - 35.
111. Shenoy S, Shekhar P, Heinrich F, Daou MC, Gericke A, Ross AH, et al. Membrane Association of the PTEN Tumor Suppressor: Molecular Details of the Protein-Membrane Complex from SPR Binding Studies and Neutron Reflection. PloS one. 2012;7(4). doi: 10.1371/journal.pone.0032591. PubMed PMID: WOS:000305297500005.
112. Vazquez F, Matsuoka S, Sellers WR, Yanagida T, Ueda M, Devreotes PN. Tumor suppressor PTEN acts through dynamic interaction with the plasma membrane. Proc Natl Acad Sci U S A. 2006;103(10):3633-8. doi: DOI 10.1073/pnas.0510570103. PubMed PMID: WOS:000236225300026.
113. Loose M, Fischer-Friedrich E, Ries J, Kruse K, Schwille P. Spatial regulators for bacterial cell division self-organize into surface waves in vitro. Science. 2008;320(5877):789-92. doi: 10.1126/science.1154413. PubMed PMID: WOS:000255644400039.
114. Iversen L, Tu HL, Lin WC, Christensen SM, Abel SM, Iwig J, et al. Ras activation by SOS: Allosteric regulation by altered fluctuation dynamics. Science. 2014;345(6192):50-4. doi: 10.1126/science.1250373. PubMed PMID: WOS:000338284400045.
115. Lietzke SE, Bose S, Cronin T, Klarlund J, Chawla A, Czech MP, et al. Structural basis of 3-phosphoinositide recognition by pleckstrin homology domains. Molecular Cell. 2000;6(2):385-94. doi: Doi 10.1016/S1097-2765(00)00038-1. PubMed PMID: WOS:000089166100016.
116. Ullrich SJ, Hellmich UA, Ullrich S, Glaubitz C. Interfacial enzyme kinetics of a membrane bound kinase analyzed by real-time MAS-NMR. Nat Chem Biol. 2011;7(5):263-70. doi: 10.1038/nchembio.543. PubMed PMID: WOS:000289617800009.
117. Gesztelyi R, Zsuga J, Kemeny-Beke A, Varga B, Juhasz B, Tosaki A. The Hill equation and the origin of quantitative pharmacology. Arch Hist Exact Sci. 2012;66(4):427-38. doi: 10.1007/s00407-012-0098-5. PubMed PMID: WOS:000305840700003.

118. Arai Y, Shibata T, Matsuoka S, Sato MJ, Yanagida T, Ueda M. Self-organization of the phosphatidylinositol lipids signaling system for random cell migration. Proc Natl Acad Sci U S A. 2010;107(27):12399-404. doi: DOI 10.1073/pnas.0908278107. PubMed PMID: WOS:000279572100064.
119. Gamba A, de Candia A, Di Talia S, Coniglio A, Bussolino F, Serini G. Diffusion-limited phase separation in eukaryotic chemotaxis. Proceedings of the National Academy of Sciences of the United States of America. 2005;102(47):16927-32. doi: DOI 10.1073/pnas.0503974102. PubMed PMID: WOS:000233463200006.
120. Das S, Dixon JE, Cho WW. Membrane-binding and activation mechanism of PTEN. Proc Natl Acad Sci U S A. 2003;100(13):7491-6. doi: DOI 10.1073/pnas.0932835100. PubMed PMID: WOS:000183845800018.
121. McConnachie G, Pass I, Walker SM, Downes CP. Interfacial kinetic analysis of the tumour suppressor phosphatase, PTEN: evidence for activation by anionic phospholipids. Biochem J. 2003;371:947-55. doi: Doi 10.1042/Bj20021848. PubMed PMID: WOS:000182733400031.
122. Hon WC, Berndt A, Williams RL. Regulation of lipid binding underlies the activation mechanism of class IA PI3-kinases. Oncogene. 2012;31(32):3655-66. doi: 10.1038/onc.2011.532. PubMed PMID: WOS:000307653800001.
123. Barnett SF, Ledder LM, Stirdivant SM, Ahern J, Conroy RR, Heimbrook DC. INTERFACIAL CATALYSIS BY PHOSPHOINOSITIDE 3'-HYDROXYKINASE. Biochemistry. 1995;34(43):14254-62. doi: 10.1021/bi00043a033. PubMed PMID: WOS:A1995TD75600033.
124. Mitchell P. Microfluidics - downsizing large-scale biology. Nat Biotechnol. 2001;19(8):717-21. doi: 10.1038/90754. PubMed PMID: WOS:000170188600016.
125. Burns MA. Analytic chemistry: Everyone's a (future) chemist. Science. 2002;296(5574):1818-9. doi: 10.1126/science.1073562. PubMed PMID: WOS:000176054300032.
126. Wolf MP, Salieb-Beugelaar GB, Hunziker P. PDMS with designer functionalities-Properties, modifications strategies, and applications. Prog Polym Sci. 2018;83:97-134. doi: 10.1016/j.progpolymsci.2018.06.001. PubMed PMID: WOS:000440530300004.
127. Sia SK, Whitesides GM. Microfluidic devices fabricated in poly(dimethylsiloxane) for biological studies. Electrophoresis. 2003;24(21):3563-76. doi: 10.1002/elps.200305584. PubMed PMID: WOS:000186858700004.
128. Lionello A, Josserand J, Jensen H, Girault HH. Protein adsorption in static microsystems: effect of the surface to volume ratio. Lab Chip. 2005;5(3):254-60. doi: 10.1039/b411179f. PubMed PMID: WOS:000227186500003.
129. Lionello A, Josserand J, Jensen H, Girault HH. Dynamic protein adsorption in microchannels by "stop-flow" and continuous flow. Lab Chip. 2005;5(10):1096-103. doi: 10.1039/b506009e. PubMed PMID: WOS:000232003200014.
130. Vigil D, Cherfils J, Rossman KL, Der CJ. Ras superfamily GEFs and GAPs: validated and tractable targets for cancer therapy? Nature Reviews Cancer. 2010;10(12):842-57. doi: 10.1038/nrc2960. PubMed PMID: WOS:000284572200011.
131. Bos JL, Rehmann H, Wittinghofer A. GEFs and GAPs: Critical elements in the control of small G proteins. Cell. 2007;129(5):865-77. doi: 10.1016/j.cell.2007.05.018. PubMed PMID: WOS:000247084600008.
132. Shaw RJ, Cantley LC. Ras, PI(3)K and mTOR signalling controls tumour cell growth. Nature. 2006;441(7092):424-30. doi: 10.1038/nature04869. PubMed PMID: WOS:000237778900034.

133. Ahearn IM, Haigis K, Bar-Sagi D, Philips MR. Regulating the regulator: post-translational modification of RAS. Nat Rev Mol Cell Biol. 2012;13(1):39-51. doi: 10.1038/nrm3255. PubMed PMID: WOS:000298381700015.
134. Palsuledesai CC, Distefano MD. Protein Prenylation: Enzymes, Therapeutics, and Biotechnology Applications. ACS Chem Biol. 2015;10(1):51-62. doi: 10.1021/cb500791f. PubMed PMID: WOS:000348332100005.
135. Hobbs GA, Der CJ, Rossman KL. RAS isoforms and mutations in cancer at a glance. J Cell Sci. 2016;129(7):1287-92. doi: 10.1242/jcs.182873. PubMed PMID: WOS:000374949100001.
136. Normanno N, Tejpar S, Morgillo F, De Luca A, Van Cutsem E, Ciardiello F. Implications for KRAS status and EGFR-targeted therapies in metastatic CRC. Nat Rev Clin Oncol. 2009;6(9):519-27. doi: 10.1038/nrclinonc.2009.111. PubMed PMID: WOS:000269255300008.
137. De Roock W, De Vriendt V, Normanno N, Ciardiello F, Tejpar S. KRAS, BRAF, PIK3CA, and PTEN mutations: implications for targeted therapies in metastatic colorectal cancer. Lancet Oncol. 2011;12(6):594-603. doi: 10.1016/s1470-2045(10)70209-6. PubMed PMID: WOS:000291842400023.
138. Gureasko J, Galush WJ, Boykevisch S, Sondermann H, Bar-Sagi D, Groves JT, et al. Membrane-dependent signal integration by the Ras activator Son of sevenless. Nat Struct Mol Biol. 2008;15(5):452-61. doi: 10.1038/nsmb.1418. PubMed PMID: WOS:000255587800012.
139. RodriguezViciana P, Warne PH, Vanhaesebroeck B, Waterfield MD, Downward J. Activation of phosphoinositide 3-kinase by interaction with Ras and by point mutation. Embo J. 1996;15(10):2442-51. doi: 10.1002/j.1460-2075.1996.tb00602.x. PubMed PMID: WOS:A1996UM40600014.
140. Thron CD. A model for a bistable biochemical trigger of mitosis. Biophys Chem. 1996;57(2-3):239-51. doi: 10.1016/0301-4622(95)00075-5. PubMed PMID: WOS:A1996TJ90500011.
141. Pomerening JR, Sontag ED, Ferrell JE. Building a cell cycle oscillator: hysteresis and bistability in the activation of Cdc2. Nat Cell Biol. 2003;5(4):346-51. doi: 10.1038/ncb954. PubMed PMID: WOS:000182080700019.
142. Kholodenko BN. Cell-signalling dynamics in time and space. Nat Rev Mol Cell Biol. 2006;7(3):165-76. doi: 10.1038/nrm1838. PubMed PMID: WOS:000235590500012.
143. Shenoy S, Shekhar P, Heinrich F, Daou MC, Gericke A, Ross AH, et al. Membrane association of the PTEN tumor suppressor: molecular details of the protein-membrane complex from SPR binding studies and neutron reflection. PloS one. 2012;7(4):e32591. doi: 10.1371/journal.pone.0032591. PubMed PMID: 22505997; PubMed Central PMCID: PMC3323581.
144. Martins BM, Swain PS. Ultrasensitivity in phosphorylation-dephosphorylation cycles with little substrate. PLoS computational biology. 2013;9(8):e1003175. doi: 10.1371/journal.pcbi.1003175. PubMed PMID: 23950701; PubMed Central PMCID: PMC3738489.
145. Minton AP. Effects of excluded surface area and adsorbate clustering on surface adsorption of proteins I. Equilibrium models. Biophys Chem. 2000;86(2-3):239-47. PubMed PMID: 11026688.
146. Iversen L, Tu HL, Lin WC, Christensen SM, Abel SM, Iwig J, et al. Molecular kinetics. Ras activation by SOS: allosteric regulation by altered fluctuation dynamics. Science. 2014;345(6192):50-4. doi: 10.1126/science.1250373. PubMed PMID: 24994643; PubMed Central PMCID: PMC4255705.

147. Hsu C, Jaquet V, Maleki F, Becskei A. Contribution of Bistability and Noise to Cell Fate Transitions Determined by Feedback Opening. J Mol Biol. 2016;428(20):4115-28. doi: 10.1016/j.jmb.2016.07.024. PubMed PMID: WOS:000385324000018.
148. Shibata T, Fujimoto K. Noisy signal amplification in ultrasensitive signal transduction. Proceedings of the National Academy of Sciences of the United States of America. 2005;102(2):331-6. doi: 10.1073/pnas.0403350102. PubMed PMID: WOS:000226315700015.
149. Altschuler SJ, Angenent SB, Wang YQ, Wu LF. On the spontaneous emergence of cell polarity. Nature. 2008;454(7206):886-U41. doi: 10.1038/nature07119. PubMed PMID: WOS:000258398600036.
150. Strogatz SHa. Nonlinear dynamics and chaos : with applications to physics, biology, chemistry, and engineering: Second edition. Boulder, CO : Westview Press, a member of the Perseus Books Group, [2015]; 2015.
151. Su YJ, Richmond A. Chemokine Regulation of Neutrophil Infiltration of Skin Wounds. Adv Wound Care. 2015;4(11):631-40. doi: 10.1089/wound.2014.0559. PubMed PMID: WOS:000363925400002.
152. Thelen M. Dancing to the tune of chemokines. Nat Immunol. 2001;2(2):129-34. doi: 10.1038/84224. PubMed PMID: WOS:000166778700008.
153. Funamoto S, Meili R, Lee S, Parry L, Firtel RA. Spatial and temporal regulation of 3-phosphoinositides by PI 3-kinase and PTEN mediates chemotaxis. Cell. 2002;109(5):611-23. doi: 10.1016/s0092-8674(02)00755-9. PubMed PMID: WOS:000175957900010.
154. Iijima M, Devreotes P. Tumor suppressor PTEN mediates sensing of chemoattractant gradients. Cell. 2002;109(5):599-610. doi: 10.1016/s0092-8674(02)00745-6. PubMed PMID: WOS:000175957900009.
155. Taniguchi D, Ishihara S, Oonuki T, Honda-Kitahara M, Kaneko K, Sawai S. Phase geometries of two-dimensional excitable waves govern self-organized morphodynamics of amoeboid cells. Proc Natl Acad Sci U S A. 2013;110(13):5016-21. doi: 10.1073/pnas.1218025110. PubMed PMID: WOS:000318031900041.
156. Postma M, Van Haastert PJM. A diffusion-translocation model for gradient sensing by chemotactic cells. Biophys J. 2001;81(3):1314-23. PubMed PMID: WOS:000170600800010.
157. Matsuoka S, Ueda M. Mutual inhibition between PTEN and PIP3 generates bistability for polarity in motile cells. Nature Communications. 2018;9. doi: 10.1038/s41467-018-06856-0. PubMed PMID: WOS:000448414100031.
158. Nguyen HN, Afkari Y, Senoo H, Sesaki H, Devreotes PN, Iijima M. Mechanism of human PTEN localization revealed by heterologous expression in Dictyostelium. Oncogene. 2014;33(50):5688-96. doi: 10.1038/onc.2013.507. PubMed PMID: WOS:000346089300004.
159. Chagpar RB, Links PH, Pastor MC, Furber LA, Hawrysh AD, Chamberlain MD, et al. Direct positive regulation of PTEN by the p85 subunit of phosphatidylinositol 3-kinase. Proceedings of the National Academy of Sciences of the United States of America. 2010;107(12):5471-6. doi: 10.1073/pnas.0908899107. PubMed PMID: WOS:000275898300038.
160. Leung BO, Chou KC. Review of Super-Resolution Fluorescence Microscopy for Biology. Appl Spectrosc. 2011;65(9):967-80. doi: 10.1366/11-06398. PubMed PMID: WOS:000294831900002.
161. Patterson G, Davidson M, Manley S, Lippincott-Schwartz J. Superresolution Imaging using Single-Molecule Localization. In: Leone SR, Cremer PS, Groves JT, Johnson MA, Richmond G, editors. Annual Review of Physical Chemistry, Vol 61. Annual Review of Physical Chemistry. 61. Palo Alto: Annual Reviews; 2010. p. 345-67.